Deformation and Damage in Fiber Reinforced Polymer and Ceramic Matrix Composite Materials

by

Travis Skinner

A Dissertation Presented in Partial Fulfillment
of the Requirements for the Degree
Doctor of Philosophy

Approved May 2021 by the
Graduate Supervisory Committee:

Aditi Chattopadhyay, Chair
Masoud Yekani-Fard
Asha Hall
Yang Jiao
Yongming Liu

ARIZONA STATE UNIVERSITY

August 2021

ABSTRACT

Fiber reinforced composites are rapidly replacing conventional metallic or polymeric materials as materials of choice in a myriad of applications across a wide range of industries. The relatively low weight, high strength, high stiffness, and a variety of thermal and mechanical environmental and loading capabilities are in part what make composite materials so appealing to material experts and design engineers. Additionally, fiber reinforced composites are highly tailorable and customized composite materials and structures can be readily designed for specific applications including those requiring particular directional material properties, fatigue resistance, damage tolerance, high temperature capabilities, or resistance to environmental degradation due to humidity and oxidation. The desirable properties of fiber reinforced composites arise from the strategic combination of multiple constituents to form a new composite material. However, the significant material anisotropy that occurs as a result of combining multiple constituents, each with different directional thermal and mechanical properties, complicates material analysis and remains a major impediment to fully understanding composite deformation and damage behavior. As a result, composite materials, especially specialized composites such as ceramic matrix composites and various multifunctional composites, are not utilized to their fullest potential.

In the research presented in this dissertation, the deformation and damage behavior of several fiber reinforced composite systems were investigated. The damage accumulation and propagation behavior of carbon fiber reinforced polymer (CFRP) composites under complex in-phase biaxial fatigue loading conditions was investigated and the early stage

damage and microscale damage were correlated to the eventual fatigue failure behavior and macroscale damage mechanisms. The temperature-dependent deformation and damage response of woven ceramic matrix composites (CMCs) reinforced with carbon and silicon carbide fibers was also studied. A fracture mechanics-informed continuum damage model was developed to capture the brittle damage behavior of the ceramic matrix. A multiscale thermomechanical simulation framework, consisting of cooldown simulations to capture a realistic material initial state and subsequent mechanical loading simulations to capture the temperature-dependent nonlinear stress-strain behavior, was also developed. The methodologies and results presented in this research represent substantial progress toward increasing understanding of the deformation and damage behavior of some key fiber reinforced composite materials.

This dissertation is dedicated to my wife,

for her continued support and encouragement. She's earned this just as much as I have.

ACKNOWLEDGMENTS

I completed the research presented in this dissertation with the assistance and guidance of many people to whom I will always be grateful. First, I want to express my sincere gratitude to my advisor, Regents' Professor Aditi Chattopadhyay, for her valuable experience, encouragement, and advice. Her continued support throughout my doctoral studies was much appreciated and helped me achieve my academic and research goals. I am also thankful to the members of my Supervisory Committee, Professors Yongming Liu, Masoud Yekani-Fard, and Yang Jiao from ASU, and Dr. Asha Hall from the US Army Research Laboratory (ARL). I am also particularly grateful to Dr. Hall for sponsoring me for an ARL Journeyman Fellowship. The support and the opportunity to interact with ARL researchers was a great benefit and blessing to me and my doctoral work.

I am grateful for the opportunity to work with and learn from Dr. Chattopadhyay's research group, including the postdoctoral researchers and my fellow Ph.D. students. I am especially thankful to Dr. Bonsung Koo and Dr. Siddhant Datta for their mentorship and encouragement when I was an undergrad first considering research. The work I did with them got me excited about research and is ultimately what helped me decide to pursue my Ph.D.

The research presented in this dissertation was supported by the US Army Research Laboratory under Cooperative Agreement W911NF-17-2-0207 (Program Manager Dr. Asha Hall) and the US Air Force Office of Scientific Research under grant number FA9550-18-1-00129 (Program Manager Dr. Jaimie Tiley).

TABLE OF CONTENTS

Page

LIST OF TABLES viii

LIST OF FIGURES x

CHAPTER

1 INTRODUCTION 1

1.1 Background and Motivation 1

1.2 Objectives 14

1.3 Outline 16

2 BIAXIAL FATIGUE DAMAGE BEHAVIOR OF CARBON FIBER REINFORCED COMPOSITES 18

2.1 Introduction 18

2.2 Materials and Methods 21

2.3 Specimen Design 24

2.3.1 Cross Ply Layup 26

2.3.2 Quasi Isotropic Layup 29

2.4 Results and Discussion 32

2.4.1 Cross Ply at Baseline Load 32

CHAPTER Page

2.4.2 Cross Ply at Low Load 37

2.4.3 Cross Ply at High Load 40

2.4.4 Quasi Isotropic Low Load 42

2.4.5 Quasi Isotropic Intermediate Load 44

2.4.6 Quasi Isotropic High Load 46

2.5 Fabrication of CNT-enhanced CFRP Composites 48

2.6 Conclusions 50

3 FRACTURE MECHANICS-INFORMED DAMAGE MODEL FOR CERAMIC MATRIX COMPOSITES 51

3.1 Introduction 51

3.2 Description of Damage Model 52

3.2.1 Thermodynamic Framework 52

3.2.2 Porosity 54

3.2.3 Matrix Cracking 56

3.2.4 Crack-induced Local Anisotropy 58

3.3 Multiscale Modeling Framework 60

CHAPTER Page

3.4 Results and Discussion 68

3.4.1 Monolithic SiC Response 68

3.4.2 Unidirectional Composite Response 74

3.4.3 Woven Composite Response 78

3.4.4 Comparison with Literature 83

3.5 Temperature-dependent Reformulation 85

3.5.1 Reformulated Damage Model 85

3.5.2 Temperature-dependent Damage Model Parameters 88

3.5.3 Results and Discussion 89

3.6 Conclusions 97

4 TEMPERATURE-DEPENDENT CERAMIC MATRIX COMPOSITE DAMAGE MODEL WITH THERMAL RESIDUAL STRESSES AND MANUFACTURING-INDUCED DAMAGE 100

4.1 Introduction 100

4.2 Model Description 101

4.2.1 Multiscale Modeling Framework 101

CHAPTER Page

4.2.2 Cooldown Simulations 103

4.2.3 Damage Model 107

4.2.4 Fiber Damage Model 110

4.2.5 Model Calibration 112

4.3 Results and Discussion 117

4.3.1 Monolithic SiC 117

4.3.2 C/SiC 119

4.3.3 Predictive Capability 124

4.4 SiC/SiC 126

4.5 Experimental Testing for Model Validation 129

4.6 Conclusions 137

5 CONTRIBUTIONS AND FUTURE WORK 140

5.1 Contributions 140

5.2 Future Work 141

REFERENCES 144

LIST OF TABLES

Table Page

Table 2.1. Biaxial Fatigue Load Parameters 24

Table 2.2. Optimized Cross Ply Specimen Parameters 27

Table 2.3. Optimized Quasi Isotropic Specimen Parameters 32

Table 3.1. Material Properties and Model Parameters Used to Simulate Monolithic SiC With Isotropic Damage ISV and Anisotropic Damage ISV 68

Table 3.2. Material Properties and Model Parameters Used to Simulate Monolithic SiC With Matrix Cracking and Porosity Effects 72

Table 3.3. Material Properties for T300 Fibers (Daniel & Ishai, 2006) 75

Table 3.4. Calibrated RT Model Parameters 91

Table 3.5. Predicted and Calibrated Parameters for 1000°C 96

Table 4.1. Temperature-dependent Material Properties for PyC and BN Interphase Materials and Sylramic Fibers 106

Table 4.2. SiC/SiC Matrix Damage Model Parameters for RT and 1200°C 128

Table 4.3. Dimensions (in mm) for S200H C/SiNC Specimen Geometry in Figure 4.16. 131

LIST OF FIGURES

Figure Page

Figure 2.1. Specimen Geometries to Investigate Multiaxial Stress States in Composite Materials; (a) Off-axis Uniaxial Coupon; (b) Tension-torsion Tubular Specimen; (c) Planar Cruciform Specimen 20

Figure 2.2. Optimized Composite Cruciform Specimen in Biaxial Test Frame 23

Figure 2.3. Cross Ply Cruciform Equivalent Strain Profiles. (a) DIC Image from Static Biaxial Load Test; (b) ANSYS FEM Simulation 28

Figure 2.4. Optimized Cross Ply Specimen Geometry 29

Figure 2.5. Quasi Isotropic Specimen Equivalent Strain Profiles. (a) ANSYS FEM Simulation; (b) DIC Image from Static Biaxial Load Test 31

Figure 2.6. Optimized Quasi Isotropic Specimen Geometry 31

Figure 2.7. Baseline Stiffness Plot for Cross Ply Specimen With R=0.1 33

Figure 2.8. Baseline Cross Ply Fatigue Specimen at 10% Fatigue Life. (a) Matrix Cracks Initiate Between Fiber Tows and Cause Transverse Tow Separation; (b) SEM Micrograph of Serrated Separation in Stage 1 of Fatigue 34

Figure 2.9. Baseline Cross Ply Fatigue Specimen at 50% Fatigue Life. (a) Additional Matrix Cracks and Increased Fiber/matrix Separation; (b) SEM Micrograph of Smooth Fiber/matrix Separation in Stage 2 of Fatigue 34

Figure Page

Figure 2.10. Fatigue Failure in Subsurface Plies. (a) Failed Specimen; (b) SEM Micrograph Showing Longitudinal Subsurface Fiber Fracture 36

Figure 2.11. Baseline Cross Ply Fatigue Specimen With R=0.3 at 50% Fatigue Life. (a) Mesoscale Matrix Cracks Between Tows (b) SEM Micrograph Showing Matrix Voids and Microcracks in Resin-rich Intertow Areas 37

Figure 2.12. Low Load Stiffness Plot for Cross Ply Specimen with R=0.1 38

Figure 2.13. Low Load Specimen at 10% Fatigue Life. (a) Surface Ply Transverse Matrix Cracks; (b) SEM Micrograph of Matrix Microcracks in Resin-rich Intertow Area..... 38

Figure 2.14. Low Load Specimen at 50% Fatigue Life. (a) Surface Ply Transverse Matrix Cracks; (b) SEM Micrograph of Matrix Cracks Between Fiber Tows..... 39

Figure 2.15. Low Load Cross Ply Load Case with R=0.3. (a) Minor Mesoscale Gage Region Damage; (b) SEM Micrograph Showing Minor Matrix Microcracking 39

Figure 2.16. Stiffness Plot for Cross Ply Specimen High Load Case..... 41

Figure 2.17. High Load Specimen at 50% Fatigue Life. (a) Transverse Separation in Surface Tows; (b) SEM Micrograph of Fiber Breakage Inside Tow Separation 41

Figure 2.18. High Load Specimen at 50% Fatigue Life. (a) Transverse Separation in Surface Tows; (b) SEM Micrograph of Fiber Breakage Inside Tow Separation 42

Figure Page

Figure 2.19. Low Load Stiffness Plot for Quasi Isotropic Laminates 43

Figure 2.20. SEM Micrographs of Low Load ($Pmax = 30kN$) Quasi Isotropic Specimen Cross Section. (a) Transverse Cracks and Interfacial Debonding at 30% Fatigue Life; (b) Transverse Cracks, Debonding, and Delamination at 60% Fatigue Life 44

Figure 2.21. Intermediate Load Stiffness Plot for Quasi Isotropic Specimen 45

Figure 2.22. SEM Micrographs of Intermediate Load ($Pmax = 35kN$) Quasi Isotropic Specimen Cross Section. (a) Transverse Cracks and Delamination at 30% Fatigue Life; (b) Transverse Cracks and Severe Delamination at 60% Fatigue Life 46

Figure 2.23. High Load Stiffness Plot for Quasi Isotropic Specimen 47

Figure 2.24. SEM Micrographs of High Load ($Pmax = 40kN$) Quasi Isotropic Specimen Cross Section. (a) Severe Delamination at 30% Fatigue Life; (b) Ply Fracture in +/-45° Plies and Severe Delamination at 60% Fatigue Life 48

Figure 2.25. Placement of Buckypaper Membrane in Optimized Cruciform Gage Region 49

Figure 2.26. Cross Sectional View of Buckypaper Membrane Placement in Optimized Cruciform Gage Region 49

Figure Page

Figure 3.1. Common CMC 2D Woven Architectures; (a) Plain Weave; (b) 5HS Weave; (c) 8HS Weave 61

Figure 3.2. MSGMC Representation of 2D Plain Weave Architecture; (a) Section of Plain Weave Architecture with Four Weave-level RUCs; (b) Weave-level RUC Discretized into Subcells—Adapted from (Aboudi, Arnold, & Bednarcyk, 2012).... 62

Figure 3.3. Multiscale Representation of 2D Plain Weave Architecture using MSGMC; (a) Exploded View of Weave-level RUC Discretized into Subcells—Adapted from (Aboudi, Arnold, & Bednarcyk, 2012); (b) Mesoscale Subcell Stacks; (c) Microscale RUC Consisting of Monolithic Fiber, Matrix, and Interphase Material Subcells 63

Figure 3.4. Schematic of MSGMC Multiscale Modeling Methodology for 5HS Weave 67

Figure 3.5. Micrograph of CVI CMC Showing Weave and Tow Level Manufacturing Induced Cavities; Adapted from Bonacuse et al. (Bonacuse, Mital, & Goldberg, 2011) 67

Figure 3.6. Simulated Stress-strain Response of Monolithic SiC with Isotropic and Anisotropic Matrix Cracking ISVs 70

Figure 3.7. Monolithic SiC Damage and Effective Modulus Evolution. (a) Isotropic and Anisotropic Damage Parameters vs. Strain; (b) Effective SiC Modulus vs. Strain 71

Figure Page

Figure 3.8. Simulated Stress–strain Response of Monolithic SiC with Microcracking and Porosity 73

Figure 3.9. Evolution of Damage Model Parameters and Effective Modulus in Monolithic SiC. (a) Normalized Microcrack Length vs. Strain; (b) Damage from Microcracking vs. Strain; (c) Damage from Nucleation and Growth of Pores vs. Strain; (d) Effective SiC Modulus vs. Strain 74

Figure 3.10. Simulated Stress–strain Response of UD C/SiC with Isotropic and Anisotropic Matrix Cracking ISVs 76

Figure 3.11. Simulated Effective Modulus Response of UD C/SiC with Isotropic and Anisotropic Matrix Cracking ISVs 76

Figure 3.12. Simulated Response of UD C/SiC with Microcracking and Porosity 77

Figure 3.13. Effective Modulus of UD C/SiC with Microcracking and Porosity Effects 78

Figure 3.14. Simulated Response of 2D Woven C/SiC CMC with Isotropic and Anisotropic Damage 79

Figure 3.15. Simulated Effective Modulus Response of 2D Woven C/SiC CMC with Isotropic and Anisotropic Damage 80

Figure Page

Figure 3.16. Simulated Response of 2D Woven C/SiC CMC with Matrix Cracking and Porosity 81

Figure 3.17. Damage in the 5HS RUC. (a) Simulated Weave Architecture; (b) Microcracking Damage (Dc) in Weave RUC at 0.25% Strain 82

Figure 3.18. Effective Modulus of 2D Woven C/SiC CMC with Matrix Cracking and Porosity 83

Figure 3.19. Comparison of Model (with Both Porosity and Matrix Microcracking) with Experimental Results from Literature..... 84

Figure 3.20. Comparing Original Formulation with Updated Formulation. (a) Monolithic SiC; (b) UD C/SiC (e.g. Minicomposite)..... 90

Figure 3.21. Comparison of RT Experiments to Simulation Results from Original and Updated Frameworks for Plain Weave C/SiC CMC 91

Figure 3.22. Temperature-dependent Model Results Compared with Experimental Data 93

Figure 3.23. Damage Model Parameter Temperature Trends. (a) Porosity Scaling Parameter; (b) Effective Pore Size Proportionality Constant; (c) Crack Density/Growth Rate Parameter; (d) Maximum Porosity Nucleation Stress; (e) Post-cracking Secant-tangent Damage Parameter; (f) Initial Damage Parameter 94

Figure Page

Figure 3.24. Predicted Response Compared to Experiment for 1000°C 96

Figure 4.1. CTE vs. Temperature; (a) Longitudinal and Transverse CTE for T300 Carbon Fiber (Pradere & Sauder, 2008); (b) CTE for CVI (Rohm and Haas, 2008) and MI (Murthy, Mital, & DiCarlo, 1999) SiC Matrix 105

Figure 4.2. Young's Modulus vs. Temperature for CVI (Rohm and Haas, 2008) and MI (Murthy, Mital, & DiCarlo, 1999) SiC Matrix 106

Figure 4.3. Experimental Longitudinal Stress-strain Response. (a) 2D Plain Weave C/SiC CMC (Yang, Zhang, Wang, Huang, & Jiao, 2017); (b) 2D 5HS Weave SiC/SiC CMC (Gowayed, et al., 2010)..... 115

Figure 4.4. Micrographs Adapted from (Khafagy, Datta, & Chattopadhyay, 2021) Showing As-produced Damage with Preferential Orientation in C/SiC CMC. (a) Partial Specimen Cross Section; (b) Close-up View..... 115

Figure 4.5. Micrographs Adapted from (Gowayed, et al., 2010) Showing As-produced damage in CVI/MI SiC/SiC CMC. (a) Specimen Cross Section; (b) Micrograph Showing Matrix Cracks and Voids Filled After MI Step 116

Figure 4.6. Simulated Stress-strain Response for RT Monolithic SiC 118

Figure 4.7. Simulation Results for RT Monolithic SiC. (a) Total Damage ISV vs. Strain; (b) Effective SiC Modulus vs. Strain..... 119

Figure 4.8. Simulated Thermal Residual Stresses for RT Plain Weave C/SiC CMC. (a) Residual Transverse Stress (Weft Direction); (b) Residual Longitudinal Stress (Warp Direction); (c) Residual Through-thickness Stress; (d) Residual Effective Stress ... 120

Figure 4.9. Damage Model Parameter Temperature Trends. (a) Porosity Scaling Parameter—Cooldown; (b) Porosity Scaling Parameter—Loading; (c) Effective Pore Size Proportionality Constant; (d) Crack Density/Growth Rate Parameter; (e) Post-cracking Secant-tangent Damage Parameter 123

Figure 4.10. Temperature-dependent Model Results Compared with Experimental Data from Ref. (Yang, Zhang, Wang, Huang, & Jiao, 2017)..... 124

Figure 4.11. Predicted C/SiC Longitudinal Response Compared to Experiment (Yang, Zhang, Wang, Huang, & Jiao, 2017) for 1000°C 126

Figure 4.12. Simulated Thermal Residual Stresses for RT 5-HS weave SiC/SiC CMC. (a) Residual Transverse Stress (Weft Direction); (b) Residual Longitudinal Stress (warp Direction); (c) Residual Through-thickness Stress; (d) Residual Effective Stress 128

Figure 4.13. Temperature-dependent SiC/SiC Model Results Compared to Experiments from Ref. (Gowayed, et al., 2010) 128

Figure 4.14. Experimental Setup with MTS Load Frame and AMTECO Furnace .. 130

Figure 4.15. AMTECO Furnace in Operation 130

Figure Page

Figure 4.16. Specimen Geometry for S200 H C/SiNC CMC Specimens..... 131

Figure 4.17. Room Temperature Experimental Results for S200H C/SiNC CMC Specimens Compared to Experiments from Literature (Artz, Yuan, Kumar, & Fish, 2020); (a) 0°/90° S200H C/SiNC CMC; (b) ±45° S200H C/SiNC CMC..... 132

Figure 4.18. DIC ARAMIS Setup with MTS Bionix Load Frame; (a) 0° S200H Specimen; (b) +/-45° S200H Specimen..... 135

Figure 4.19. Select Major Strain DIC Results for RT Quasi Static Load Test for 0°/90° S200H CMC; (a) 0% Strain; (b) 0.048% Strain—Localized Strain Near Defect and in Undulating Tows and Intertow Regions ; (c) 0.4% strain; (d) 0.45% Strain; (e) 0.5% Strain (Immediately Preceding Failure); (f) Post Failure 135

Figure 4.20. Select Major Strain DIC Results for RT Quasi Static Load Test for +/-45° S200H CMC; (a) 0% Strain; (b) 0.05% Strain—Localized Strain in Undulating Tows and Intertow Regions ; (c) 0.45% strain; (d) 0.48% Strain; (e) 0.5% Strain (Immediately Preceding Failure); (f) Post Failure..... 136

Figure 4.21. Failed S200H Specimens; (a) 0° Specimen; (b) +/- 45° Specimen..... 137

1 INTRODUCTION

1.1 Background and Motivation

Composite materials offer numerous benefits and are rapidly emerging as materials of choice in a wide range of applications. However, the scientific barriers pertaining to reliability and durability of these complex and heterogeneous material systems are major impediments limiting their widespread usage. During their service life in aerospace as well as ground vehicles, composite structures experience a wide variety of fatigue loading conditions. Understanding composite damage initiation and propagation behavior under such complex dynamic loading is an essential part of optimizing their performance and predicting useful life. Researchers have recognized the need to understand composite fatigue damage behavior, and a significant number of studies have been reported on this topic (Hashin, 1985; Daniel, Wooh, & Lee, 1987; Peng, Liu, Saxena, & Goebel, 2015; Degrieck & Van Paepegem, 2001; Bathias, An engineering point of view about fatigue of polymer matrix composite materials, 2006; Sun, Daniel, & Luo, 2003; Lua, Pham, Rahman, & Phan, 2018). Despite recent advancements in composite fatigue, the complexity of fatigue analysis in these heterogeneous, anisotropic materials and the very limited availability of multiaxial test frames has largely limited the literature to studies on composite fatigue behavior under uniaxial loading, leaving composite damage behavior under multiaxial fatigue loading largely unexplored.

Curtis (Curtis, 1991) studied tensile fatigue in polymer matrix composites and showed that the dominant damage growth mechanisms for unidirectional laminates was splitting along the fiber direction (transverse cracking). Fracture mechanics based expressions were

developed to describe the straightforward damage mechanism of transverse cracking, however these results cannot be applied to laminates containing off axis plies. Wright et al. (Wright, Fu, Sinclair, & Spearing, 2008) studied quasistatic tensile composite damage mechanisms using computed tomography to capture damage in $[90/45/-45/\bar{0}]_S$ (quasi-isotropic) uniaxial coupons. In each of the off axis plies, transverse cracks grew along the fiber direction and showed complex interaction with cracks in adjacent plies. Significant delamination occurred between the +45° and -45° plies because of the large difference in angle between them, and the interactions between the cracks in other plies caused crack arrest as ply cracks encountered the interlaminar boundary. Additionally, fiber breaks in the 0° ply were aligned with the ply cracks in the adjacent -45° plies, suggesting that much of the damage in the 0° ply resulted from interactions with damage in neighboring plies. This work further describes additional interactions between matrix cracking, delamination, fiber fracture, and fiber pull out in each ply. These results give insight into the complex interactions between composite damage mechanisms, but this study only considered quasistatic tensile loading and therefore does not describe the additional complexities introduced by fatigue loads. Talreja (Talreja R. , 1981) and Bathias (Bathias, Fracture and fatigue of high performance composite materials: mechanisms and prediction, 1991) studied the growth of damage mechanisms (especially delamination) in uniaxially loaded composite coupon specimens and developed rough fatigue life estimates for various stacking sequences. These researchers show that composite damage mechanisms strongly govern the fatigue behavior and useful life of composites. The initiation and growth of composite damage mechanisms are driven by local strain fields that depend on both stacking sequence and loading (Kawai, A phenomenoligical model for off-axis fatigue

behavior of unidirectional polymer matrix composites under different stress ratios, 2004). Introducing multiaxial loads adds further complexity due to intricate interactions between external loading and composite fatigue damage mechanisms. Investigations into the effects of multiaxial fatigue in composites is limited.

Due to their anisotropic nature, composites often experience complex internal multiaxial stress states even under uniaxial loading conditions. Montesano et al. (Montesano, McCleave, & Singh, 2018) studied the growth of damage within multidirectional laminates due to local multiaxial stress states and interactions between localized damage mechanisms in adjacent plies. According to their work, localized ply cracks grow along the fiber direction of their respective plies. As crack density in each ply increases, local stress fields around ply cracks in adjacent plies interact, either resulting in crack arrest (crack shielding) or causing additional stress concentrations that result in further crack growth and a global reduction in material properties. Additionally, this work discussed the formation of critical damage modes (damage mechanisms that govern failure behavior) such as delamination from sub-critical damage mechanisms such as transverse ply cracks. Kawai et al. (Kawai, Yajima, Hachinohe, & Takano, 2001) studied the effects of local multiaxial stress states on the fatigue behavior of unidirectional off axis composite laminates. They found that transverse cracks formed and grew until they penetrated through-thickness and then extended along the fiber direction into the tab region of the uniaxially loaded coupons. Longitudinal fatigue failure, with fiber pullout and fiber fracture, occurred shortly after. Their work showed that failure mechanisms in off axis plies are governed by the fatigue strengths of the matrix as well as the strength of the fiber/matrix

interface. The studies mentioned have increased the understanding of the effects of local multiaxial stress states on composites under external uniaxial loading, but they fail to account for interactions between local (internal) multiaxiality and global (external) multiaxiality that occur when external multiaxial loads are applied. Results obtained from uniaxial tests cannot be used to predict failure under external multiaxial loading conditions, which composite structures often experience during their lifetimes. Interactions between multiaxial loads and the initiation and propagation of key damage mechanisms can be highly intricate, making life prediction a challenging task. To better understand damage initiation and propagation behavior in composite materials, the material response to external multiaxial fatigue loading conditions must be explored.

Thin walled cylindrical tension-torsion specimens are perhaps the most common geometry used to study external multiaxial fatigue in composites, primarily because of the simplicity of specimen design and test setup (Quaresimin & Carraro, 2013; Smits, Van Hemelrijck, Philippidis, & Cardon, 2006). Lee et al. (Lee, Hwang, Park, & Han, 1999) used SEM microscopy to investigate the damage and failure mechanisms of carbon/epoxy composite tension-torsion tubes subjected to different biaxiality ratios. Failure at low biaxiality ratios was distributed along the entire length of the tube and matrix damage mechanisms dominated, leading to severe fiber pull out at fatigue failure. High biaxiality ratios caused localized failure with fiber damage mechanisms dominating and fatigue failure occurred due to fiber fracture. The variation in thickness and fiber volume fraction were directly correlated with the biaxial fatigue behavior of the thin-walled tubes. Quaresimin et al. (Quaresimin, Susmel, & Talreja, 2010) performed an extensive review

of literature on the fatigue behavior and life prediction of composites under multiaxial loading and showed discrepancies between the multiaxial fatigue behavior of tension-torsion tubes and tension-tension cruciforms. The curvature of the tension-torsion tubular specimens can cause significant variations in thickness and fiber volume fraction which can lead them to exhibit different multiaxial fatigue behavior than flat or slightly curved specimens. This can potentially make them unsuitable to characterize multiaxial fatigue in many composite components used in aerospace and ground vehicles (Smits, Van Hemelrijck, Philippidis, & Cardon, 2006; Quaresimin, Susmel, & Talreja, 2010).

Although planar cruciform specimens are more difficult to design and test, they are better suited to study multiaxial stress states in these types of structures. Some researchers have used planar cruciform specimens to study the effects of static multiaxial loading in composites (Smits, Van Hemelrijck, Philippidis, & Cardon, 2006; Mayes, Welsh, & Key, 2002; French, Rapking, Mollenhauer, & Czabaj, 2016), but only a few have considered multiaxial fatigue in cruciform specimens (Baptista, Claudio, Reis, Madeira, & Freitas, 2016; Sun, et al., 2012; Li, Datta, Chattopadhyay, Iyyer, & Phan, 2019). To the best of the authors' knowledge, investigations into the damage mechanisms in carbon fiber reinforced polymer (CFRP) composites under planar biaxial fatigue loading has not been reported in literature. Capturing this complex damage behavior is crucial to understanding composite response to multiaxial fatigue and predicting the service life of composites in real platforms.

Those few researchers who have used planar cruciform specimens to study biaxial fatigue in composites used tapered thickness specimens, either by machining out the gage

region (French, Rapking, Mollenhauer, & Czabaj, 2016) or by using ply drops (Makris, et al., 2010), to ensure failure in the gage region. Baptista et al. (Baptista, Claudio, Reis, Madeira, & Freitas, 2016) reported a numerical study of biaxial fatigue crack growth in optimized cruciform geometries. They showed that tapered thickness specimens are suitable for studying biaxial fatigue damage initiation but lead to uneven damage propagation due to nonuniform gage region thickness and assert that constant thickness specimens are better suited to investigate composite biaxial fatigue damage propagation behavior.

Ceramic matrix composites (CMCs) have a wide range of applicability and are often selected by designers for components operating in extreme service conditions such as those seen in the propulsion and energy production fields (Binner, et al., 2020; Schmidt, et al., 2004; Ohnabe, Masaki, Onozuka, Miyahara, & Sasa, 1999). The relatively low density, wide range of operating temperatures, and desirable properties of CMCs, including strength, stiffness, toughness, and damage resistance (Arai, Inoue, Goto, & Kogo, 2019; Rubio, et al., 2020; Krenkel, 2008), have positioned CMCs as ideal replacements for conventional high temperature materials such as nickel-based superalloys. However, CMCs exhibit complex temperature-dependent thermomechanical deformation and damage behavior that occurs across multiple length scales, and material performance under critical mechanical and environmental loading conditions is not completely understood. As a result, the inherent capabilities of CMCs are not fully exploited. Accurately modeling the complex thermomechanical behavior of CMC material systems, which occurs across multiple length scales, is a challenging task that largely limits the understanding of CMC

material performance. Any predictive analysis framework must consider scale-specific features and behaviors and incorporate them in a synergistic manner. This motivates the need for a multiscale modeling framework that integrates physics-based thermomechanical constitutive models with scale-specific damage behavior for damage assessment of CMC components in service environments. A multiscale modeling framework that can capture the scale-specific and temperature-dependent damage behavior is required to accurately predict CMC damage behavior in service environments.

During their service life, CMCs are exposed to a wide range of operating temperatures, which has a significant effect on the CMC response (Gowayed, et al., 2010; Yang, Zhang, Wang, Huang, & Jiao, 2017). Accounting for these thermal effects is critical to understanding CMC damage behavior and material performance under a wide array of operating conditions. The manufacturing process also plays an important role in CMC response and damage. Most SiC matrix CMCs are manufactured using chemical vapor infiltration (CVI), polymer infiltration and pyrolysis (PIP), or melt infiltration (MI), all of which occur at extremely high temperatures (up to ~1200°C for CVI, up to ~1600°C for PIP, and up to ~1400°C for MI) (Heidenreich, 2015; DiCarlo, 2015). As a result of spatially and architecturally varying thermal properties, CMCs experience significant thermal residual stresses when they are cooled from processing to operating temperatures. Appreciable as-produced damage can occur as a result of the high thermal residual stresses and must be accounted for to accurately capture the initial material state. Typical C/SiC CMCs are manufactured using an initial CVI step to deposit a thin interfacial pyrolytic carbon (PyC) layer on the fiber surfaces, followed by deposition of the SiC matrix using

CVI (Heidenreich, 2015; DiCarlo, 2015). Similarly, an initial CVI step is also used to deposit a thin interfacial boron nitride (BN) layer on the fiber surfaces of most SiC/SiC CMCs. The subsequent matrix densification process for SiC/SiC CMCs typically consists of an initial CVI matrix deposition step followed by MI to fill voids and achieve higher matrix density (DiCarlo, 2015). This results in two distinct SiC phases as well as pockets of excess Si in the SiC matrix of CVI/MI SiC/SiC material systems. Each phase has distinct thermomechanical properties which must be accounted for to accurately model the overall weave thermomechanical damage response. In general, C/SiC CMCs are more susceptible to manufacturing-induced damage than SiC/SiC CMCs because of the higher mismatch between constituent thermal properties. Additionally, the relatively high-density matrix resulting from the two-step matrix densification process used to manufacture SiC/SiC CMCs is more resistant to matrix cracking and manufacturing-induced damage because the MI step fills voids and cracks left by the CVI step.

Most CMC models assume a pristine initial state, or at most assume initial degraded material properties to match the stiffness of the as-produced CMC. Manufacturing-induced damage can result in reduced material performance that must be accounted for to accurately model CMC thermomechanical deformation and damage behavior. Yang et al. (Yang, Yuan, & Markert, 2019) studied the thermomechanical degradation and microstructural evolution of oxide/oxide CMCs due to cyclic thermal shocks. They showed that differences in constituent thermal properties resulted in significant microporosity formation and material property degradation when rapidly cooled. In addition to the microporosity, they observed delamination due to high temperature gradients, and matrix cracking due to in-

plane thermal tensile stresses. The high cooling rate exacerbated these cooldown-induced damage mechanisms, but thermal property mismatch can result in significant damage and property degradation even when cooled gradually, and should be included in CMC models. Gowayed et al. (Gowayed, et al., 2010) investigated the effects of temperature on the elastic properties of a SiC/SiC CMC and correlated the global weave elastic properties to the in situ temperature-dependent properties of the constituent phases. This is a valuable work that increases understanding of the temperature-dependent response of SiC/SiC CMCs, but it fails to account for thermal residual stresses and manufacturing induced damage. Yang et al. (Yang, Zhang, Wang, Huang, & Jiao, 2017) accounted for thermal residual stresses due to cooldown in a 2D plain weave C/SiC CMC and were able to model the as-produced matrix cracks with a reasonably accurate initial modulus.

Damage in CMCs is temperature dependent and occurs across multiple length scales. Damage behavior in brittle matrix CMCs is typically dominated by matrix damage mechanisms, particularly in monotonic tensile tests of brittle matrix CMCs with higher matrix modulus than fiber modulus (Yang, Zhang, Wang, Huang, & Jiao, 2017). In these CMCs, the matrix stress increases more rapidly than the fiber stress and damage initiates in the matrix in the form of tow level matrix cracks followed by intratow weave level matrix cracking. These damage mechanisms eventually progress and lead to fiber/matrix debonding followed by fiber fracture and pullout at high strains. Longbiao (Longbiao, 2018) studied the damage and fracture behavior of a SiC fiber, magnesium aluminosilicate (MAS) matrix CMC under thermomechanical fatigue loading at different temperatures. They showed that significant material degradation occurs at high temperatures due to an

increase in matrix microcracking as well as oxidation and weakening of the fiber/matrix interphase. Ladeveze et al. (Ladeveze, Gasser, & Allix, 1994) studied room temperature damage in SiC/SiC CMCs and developed thermodynamic constitutive damage models to capture the CMC stress-strain response. Arhatari et al. (Arhatari, Zonneveldt, Thornton, & Abbey, 2017) studied damage mechanisms in C/C-SiC CMCs under four-point bending using X-ray radiography. They observed scale-dependent damage mechanisms including intertow and intratow matrix microcracks, fiber-matrix interfacial debonding, progressive fiber filament failure, fiber pullout, and delamination.

The scale-dependent and temperature-dependent CMC damage behavior necessitates the use of multiscale thermomechanical modeling methods to accurately capture temperature and damage effects at each length scale. Multiscale studies have shown numerous advantages over single scale methods to understand material behavior in heterogeneous composite material systems (Sadowski & Marsavina, Multiscale modelling of two-phase ceramic matrix composites, 2011; Kanoute, Boso, Chaboche, & Schrefler, 2009; Sadowski, Multiscale modelling of damage and fracture processes in composite materials, 2007). Ceramic matrix composites exhibit strong length scale dependent behavior which makes the inclusion of such phenomenon imperative to accurately model global material behavior and predict material properties. The generalized method of cells (GMC) developed by Aboudi et al. (Aboudi, Arnold, & Bednarcyk, 2012) is well suited to model composite materials and can capture limited length scale dependent behavior (Liu, Chattopadhyay, Bednarcyk, & Arnold, 2011; Borkowski & Chattopadhyay, 2015). This method assumes that a macroscale composite material can be fully defined by an infinitely

repeating periodic microstructure. The repeating microstructure is taken as the composite representative unit cell (RUC) and discretized into an arbitrary number of subcells which are assigned different material properties to represent a composite microstructure with multiple constituents. Continuity of tractions and displacements between neighboring subcells is enforced in an average sense, and subcells are assumed to be in static equilibrium. By enforcing these conditions, the homogenized RUC response can be obtained as the volume averaged response of its subcells, which depend on the geometry, material properties, and constitutive behavior of each subcell. Localization/homogenization algorithms provide the relationship between the stress/strain in each subcell and the averaged RUC stress strain, thus allowing for an accurate semi-analytical solution linking the overall composite behavior to that of each constituent. The GMC framework was extended by Liu et al. (Liu, Chattopadhyay, Bednarcyk, & Arnold, 2011) into a multiscale GMC (MSGMC) framework that is well suited to capture scale-dependent material behavior by recursively applying GMC to each length scale. The recursive nature of MSGMC provides a means to concurrently solve multiple relevant length scale models. In this case, the CMC weave is divided into three main length scales—the microscale (fiber/matrix level), mesoscale (fiber tows and intertow matrix) and macroscale (full composite weave). The global thermomechanical behavior of the CMC weaves can be obtained by simulating each relevant length scale and applying appropriate material constitutive models. This method is well suited to capture the multiscale response of CMC weaves to external loading and can be used in conjunction with additional material theories to capture CMC thermomechanical behavior. Borkowski et al. (Borkowski & Chattopadhyay, 2015) used MSGMC to investigate the effects of cooldown and simulate

the as-produced damage state of RT plain weave and UD C/SiC CMCs. By accounting for thermal residual stresses, they were able to capture a realistic initial state with local concentrations of damage in the RT UD CMC.

A key objective in a multiscale methodology is to capture the dominant scale-dependent damage mechanisms and model their propagation behavior across length scales to accurately predict structural scale damage and failure. In CMCs, damage appears in the form of intertow and intratow matrix microcracks, fiber-matrix interfacial debonding, progressive fiber filament failure, etc (Ladeveze, Gasser, & Allix, 1994). Furthermore, the presence of defects in the as-received parts or specimens introduces additional complexities. Chemical vapor infiltration (CVI), melt infiltration (MI), and polymer infiltration and pyrolysis (PIP) are the most common CMC manufacturing methods (Heidenreich, 2015; DiCarlo, 2015) and result in significant manufacturing induced cavities that detrimentally affect the thermomechanical behavior of the finished parts. As a result, accurately modeling the distribution of manufacturing induced cavities is critical to capturing CMC behavior. Liu et al. (Liu, Chattopadhyay, & Arnold, Impact of material and architecture model parameters on the failure of woven CMCs via the multiscale generalized method of cells, 2011) showed that assuming uniformly distributed manufacturing induced cavities caused overpredictions of CMC mechanical properties because of incorrect local failure modes and stress distributions. They concluded that localized cavity concentrations were necessary to accurately capture CMC deformation behavior.

Other researchers have used internal state variable (ISV) theory and continuum damage mechanics (CDM) to describe damage in CMCs and to derive constitutive laws based on the thermodynamics of deformation and damage. Camus (Camus, 2000) applied the CDM methodology to a 2D SiC/SiC CMC and used a phenomenological internal damage variable to modify the composite compliance tensor. This methodology is applied to the composite at the macroscale and is highly dependent on loading conditions and weave architecture. Hild et al. (Hild, Burr, & Leckie, 1996) developed a similar CMC damage model using the CDM framework and included elements of micromechanics to inform the damage model. They defined two damage variables to describe matrix cracking and interface debonding and derived evolution equations by combining experimental results with basic micromechanical analysis. Though the micromechanical analysis includes actual physics of deformation and damage at the microscale, the model remains largely phenomenological at the macroscale and is highly dependent on composite architecture. Maire et al. (Maire & Lesne, 1997) used ISV theory to create a CMC damage model with damage ISVs that degraded stiffness in the composite principal axes. Again, because this model is applied at the macroscale it fails to capture micro- and mesoscale damage behavior and is only valid for a specific composite architecture. The definitions of the damage variables and other ISVs in these models satisfy thermodynamics, but they may not capture the actual physics of damage in CMCs because the evolution laws are selected for mathematical tractability and to satisfy thermodynamics. Additionally, each of these models is weave dependent because they are applied at the macroscale. A benefit of the MSGMC framework is that it can be used to capture the behavior of multiple CMC weaves simply by rearranging the RUC to resemble the composite architecture. The damage relationships are applied to the

constituents at each relevant length scale, therefore the scale dependent behavior of each constituent must be understood.

Researchers have made significant strides in understanding the mechanical behavior of brittle ceramic materials. Paliwal et al. (Paliwal & Ramesh, An interacting micro-crack damage model for failure of brittle materials under compression, 2008) created a damage model to describe the degradation of brittle materials due to the growth of microcracks. They use fracture mechanics and crack growth kinetics to determine how microcracks activate and propagate and the resulting effects on ceramic mechanical integrity. Rubin et al. (Rubin, Vorobiev, & Glenn, 2000) used a thermodynamic approach to describe the nucleation and growth of porosity in brittle materials. Evans et al. (Evans, Rice, & Hirth, 1980) investigated the mechanisms of pore nucleation and showed that porosity is a major deformation mechanism in ceramics and that pores form as a result of material diffusion around grain boundaries. Finally, Deshpande et al. (Deshpande & Evans, 2008) describe mechanisms of inelasticity in ceramics. They showed that high confining stresses lead to crack growth arrest and the onset of grain boundary sliding and developed a constitutive model for the inelastic deformation and fracture of ceramics. These works have increased understanding of the damage behavior of ceramics and have been instrumental in developing the CMC matrix damage model discussed in this work.

1.2 Objectives

Following are the principal objectives of this work:

- Optimize specimen geometry to facilitate study of CFRP response to biaxial fatigue loading. Develop methodology for in-phase planar biaxial fatigue damage characterization in carbon fiber composites.
- Quantify and characterize biaxial fatigue damage mechanisms in CFRP composites. Investigate effects of external loading and stacking sequence and correlate with nucleation and propagation of damage mechanisms.
- Fabricate nano-enhanced CFRP laminates that can be used to characterize benefits of incorporating nano-engineered particles such as CNTs to increase fatigue life, delay damage mechanism nucleation and growth, and to explore potential self-sensing capabilities.
- Develop multiscale CMC matrix damage model to simulate nucleation and growth of matrix damage across length scales.
- Extend and reformulate CMC damage model to account for effects of temperature and investigate temperature-dependent damage parameter trends.
- Account for residual stresses and manufacturing induced damage in CMCs due to cooldown from manufacturing to operating temperatures. Incorporate temperature-dependent CMC material properties and thermal damage model to obtain realistic as-produced initial damage state of the material.
- Predict nonlinear temperature-dependent stress-strain response of 2D woven CMC using thermomechanical damage model.
- Conduct thermomechanical loading tests to investigate CMC matrix damage nucleation and propagation behavior and to validate CMC damage models.

1.3 Outline

The document is structured as follows:

Chapter 2 introduces the optimized cruciform geometries for investigating biaxial fatigue behavior of cross ply and quasi-isotropic CFRP composite material systems. The characterization and testing results are presented and SEM microscopy and fractography is conducted to investigate the nucleation and evolution of CFRP damage mechanisms due to the external loading and stacking sequence.

Chapter 3 presents the formulation of a fracture mechanics-informed multiscale CMC matrix damage model. The damaged constitutive laws and the multiscale modeling framework are introduced. An extended temperature-dependent reformulation is also presented that allows the model to capture effects of temperature on the 2D woven CMC stress-strain response.

In Chapter 4, a temperature dependent thermomechanical multiscale damage model framework is developed for woven CMCs that builds on the fracture mechanics-informed matrix damage model introduced in Chapter 3. The framework consists of cooldown simulations, which capture a realistic material initial state, and subsequent mechanical loading simulations to capture temperature-dependent nonlinear stress-strain behavior. The cooldown simulations result in a realistic material initial state with thermal residual stresses and damage hotspots that occur due to constituent property mismatch and post-manufacturing cooldown. A temperature-dependent reformulation of the fracture mechanics-informed brittle matrix damage model is applied to capture the manufacturing-

induced damage that occurs because of the high thermal residual stresses and to simulate the mechanical response of 2D plain weave C/SiC CMCs at temperatures ranging from RT to 1200°C.

Chapter 5 discusses the contributions to composites research made through the work conducted to produce this dissertation. Current work and future directions of the current research are also discussed. Additionally, ideas for extending this work to additional applications are explored.

2 BIAXIAL FATIGUE DAMAGE BEHAVIOR OF CARBON FIBER REINFORCED COMPOSITES

2.1 Introduction

Various test configurations and specimen designs can be utilized to study how fiber reinforced composite materials respond to multiaxial stress. The high anisotropy of fiber reinforced composite materials often results in complicated local (internal) multiaxial stress profiles even when subjected to simple uniaxial loading conditions. As a result, uniaxial loading tests are often conducted on off-axis flat coupon specimens (Figure 2.1(a)) to investigate the nucleation and growth of various damage mechanisms under local multiaxialities. Off-axis uniaxial specimens are easy to manufacture and easy to test. However, the local multiaxial stress fields are sensitive to flaws such as voids or fiber misalignment. Additionally, since the multiaxiality is local, damage that initiates in multiaxially stressed regions often propagates away into regions under different stress states. To properly study damage propagation, damage should propagate through relatively constant multiaxial stress fields (Smits, Van Hemelrijck, Philippidis, & Cardon, 2006). Thus, uniaxially loaded specimens can be used to study damage initiation under multiaxial stress, but are not ideal for damage propagation studies.

Tension-torsion tubular specimens (Figure 2.1(b)) are also commonly used to study multiaxiality in composites. As simultaneous tension and torsion are applied, the corresponding normal and shear stresses are superimposed, resulting in a global (external) multiaxial stress state. Various combinations of local multiaxiality and interactions between local and global multiaxiality can also be investigated by varying the laminate

stacking sequence to obtain the desired stress states. Tension-torsion specimen geometries are relatively easy to test, given the proper equipment, but are difficult to manufacture and often have defects that affect the validity of results. Additionally, the curvature of the tension-torsion tubular specimens can cause significant variations in thickness and fiber volume fraction and can cause radial stress gradients. As with the uniaxial off-axis specimens, tension-torsion specimens are suitable for studying damage initiation behavior in multiaxial loading conditions but are not well suited for damage propagation studies due to the radially varying multiaxial stress fields.

Planar cruciform specimens (Figure 2.1(c)) are the final specimen geometry frequently used to study multiaxial stress in composite materials. These specimens are difficult to design and fabricate and require specialized equipment to test. However, they are well suited to study in-plane multiaxial stress states in composite materials. Local multiaxialities can be readily induced by altering the laminate stacking sequences, and global multiaxiality is simple to apply by varying the loading applied to the specimen arms. The specimen gage region can be optimized to obtain a uniform multiaxial stress state to facilitate damage initiation as well as damage propagation studies since damage can propagate through regions of uniform multiaxiality. In this work, planar cruciform geometries were selected to study the multiaxial fatigue damage behavior of CFRP composite laminates.

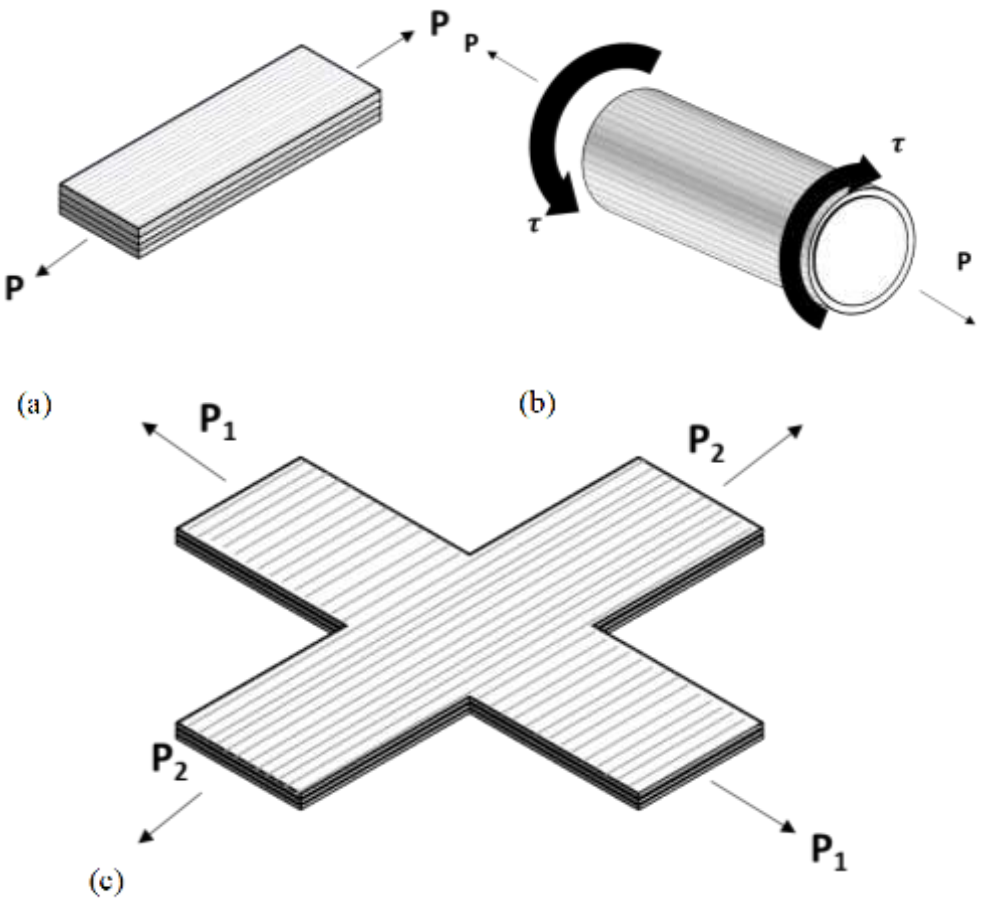

Figure 2.1. Specimen Geometries to Investigate Multiaxial Stress States in Composite Materials; (a) Off-axis Uniaxial Coupon; (b) Tension-torsion Tubular Specimen; (c) Planar Cruciform Specimen

Significant characterization and experimental testing is required to better understand composite multiaxial fatigue behavior due to the high variability and interactions between complex damage mechanisms. This chapter focuses on fatigue damage mechanisms in CFRP composites under constant amplitude planar biaxial fatigue. Extensive biaxial testing has been conducted with the goal of identifying micromechanisms that govern

damage nucleation and propagation and correlating them with the macroscale fatigue-fracture behavior. A major difficulty in simulating or performing multiaxial fatigue tests using cruciform specimens is to design a specimen geometry that results in a uniform plane stress state when subjected to biaxial loads. Constant thickness specimens were designed for this study to avoid machining damage, to prevent strain concentrations near ply drops, and to facilitate the study of biaxial fatigue damage mechanisms and damage propagation behavior in biaxially fatigued composites. FEM analysis was conducted using the commercial software ANSYS, and a multi-objective genetic algorithm (MOGA) optimization technique, available in ANSYS DesignXplorer, was used to obtain the geometry which optimally satisfied the key requirements.

The chapter is organized as follows: Section 2.2 describes the biaxial fatigue experimental setup and the SEM microscopy used to investigate microscale damage mechanisms. Section 2.3 details the design and validation of the specimen geometries. Section 2.4 presents results from biaxial fatigue tests and discusses the correlation between loading parameters, damage mechanisms, and fatigue failure modes for cross ply and quasi isotropic CFRP laminates. Finally, the last section concludes the chapter and provides a summary of findings.

2.2 Materials and Methods

In this work, planar cruciform specimens were fabricated from laminated composite plates. The plates were manufactured using the wet layup method with unidirectional T700-SC-12K-50C carbon fiber and thermoset FS-A23 epoxy resin and were cured in a hot press to achieve greater matrix material properties. The specimen geometry was cut out of the

laminates using a high-pressure CNC waterjet cutter to avoid machining damage to the specimens.

Equibiaxial (biaxiality ratio of 1) in-phase planar biaxial fatigue experiments were conducted using the MTS biaxial with torsion load frame shown in Figure 2.2. This unique load frame is equipped with six independent actuators which allows for testing over a wide range of multiaxial load conditions including in-phase, out-of-phase, proportional, and non-proportional biaxial fatigue loading. The test frame has dynamic in-plane load capacity of up to 100kN in the horizontal and vertical directions and the horizontal actuators have a torsional load capacity of up to 1100 N-m. Biaxial fatigue testing over a range of loadings were performed for cross ply specially orthotropic laminates and quasi isotropic laminates to determine the effects of loading parameters on composite fatigue damage behavior. The fatigue test details are provided in Table 2.1. A high-resolution camera was positioned to capture meso scale damage initiation and propagation in the specimen gage region. In addition, specimen stiffness was recorded to capture material property degradation in the horizontal and vertical directions and was correlated with the fatigue cycles and the extent of fatigue damage in the specimen.

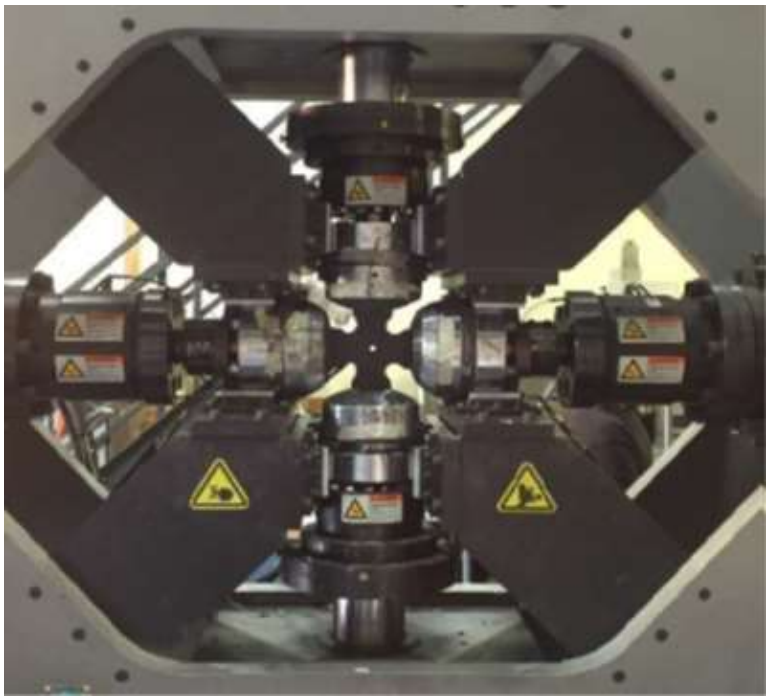

Figure 2.2. Optimized Composite Cruciform Specimen in Biaxial Test Frame

Additional fatigue tests were performed and interrupted at various levels of fatigue and the microscale damage mechanisms were investigated using SEM to determine the effects of loading parameters and stacking sequence on biaxial fatigue damage behavior. Sections of the gage regions were cut out from the fatigued specimens using a low speed cubic boron nitride (CBN) cutting wheel. Surface damage mechanisms were investigated by polishing the specimen gage region prior to fatigue testing and using SEM to analyze the surface of the fatigued specimens. Internal damage mechanisms were studied by analyzing the cross sections of the gage region.

Table 2.1. Biaxial Fatigue Load Parameters

Cross Ply		Quasi Isotropic		
Pmax (kN)	R ratio	Pmax (kN)	Frequency (Hz)	Biaxiality Ratio (P_y/P_x)
35	0.1	30	5	1
30	0.1	35	5	1
30	0.3	37	5	1
27	0.1	40	5	1
27	0.3	42	5	1
25	0.1	-	5	1
25	0.3	-	5	1

2.3 Specimen Design

The essential design requirements for studying biaxial loading are presented as follows: 1) Maximize region of uniform biaxial strain; 2) Ensure failure initiates in gage region; 3) Minimize stress concentrations outside gage region; 4) Minimize load sharing between adjacent arms (Smits, Van Hemelrijck, Philippidis, & Cardon, 2006; Mayes, Welsh, & Key, 2002). Load sharing occurs when the stress from one set of arms flows away from the gage region into the adjacent perpendicular arms, thus increasing stress in the uniaxially loaded arms. This can lead to failure outside of the gage region. Additionally, Poisson's effects can lead to biaxial strengthening, which can increase the strength of the biaxially

loaded gage region relative to the uniaxially loaded arms and can cause failure to occur away from the gage region. A central hole was introduced to facilitate fatigue failure in the gage region, and the Tsai-Wu failure criteria was used to determine the location of failure initiation. Tsai-Wu criteria was selected as it includes the interaction effects between stresses in the material principal directions, making this failure theory well suited for analyzing biaxially loaded composite specimens.

The following objective function was defined to optimally satisfy the design requirements when minimized:

$$\boldsymbol{F}(\bar{x}) = w_1\boldsymbol{f_1}(\bar{x}) + w_2\boldsymbol{f_2}(\bar{x}) + w_3\boldsymbol{f_3}(\bar{x}), \tag{2.1}$$

where $\bar{x}$ are the specimen geometrical parameters, and $w_1 = w_2 = w_3$ are the assigned weights to objectives $\boldsymbol{f_1}$, $\boldsymbol{f_2}$, and $\boldsymbol{f_3}$ which are defined as follows:

$$\boldsymbol{f_1}(\bar{x}) = \frac{TW_{out}}{TW_{gage}} - 1. \tag{2.2}$$

In this equation, TW_{out} and TW_{gage} are the maximum Tsai-Wu factor outside the gage region and inside the gage region, respectively. Minimizing this ratio ensures failure in the gage region and decreases stress and strain concentrations outside the gage region. Similarly, the following minimizes the ratio of the standard deviation of gage region strain (ε_{gage}) to the average gage region strain, thus increasing the uniformity of the strain field in the gage region:

$$\boldsymbol{f_2}(\bar{x}) = \frac{StDev(\varepsilon_{gage})}{Ave(\varepsilon_{gage})} - 1. \tag{2.3}$$

Finally, $\boldsymbol{f_3}$ is defined using the ratio of σ_{near} and σ_{far}, which are the perpendicular stresses in each arm near the gage region and far from the gage region, respectively. Minimizing this ratio decreases load sharing between adjacent arms and causes stress to flow through the gage region rather than deviating into the cruciform arms:

$$\boldsymbol{f_3}(\bar{x}) = \frac{\sigma_{\text{near}}}{\sigma_{\text{far}}} - 1. \tag{2.4}$$

Finite element analysis was conducted using the commercial software ANSYS, and a multi-objective genetic algorithm (MOGA) optimization technique available in ANSYS DesignXplorer was used to perform the optimization and obtain the specimen geometry which optimally satisfied the key design requirements. The stress state in composites is highly dependent on the stacking sequence, so adjustments to the design are required for different layups to ensure design requirements are optimally satisfied. Specially orthotropic cross ply specimens and quasi isotropic specimens were designed to investigate the biaxial fatigue damage behavior in laminates with multiple stacking sequences.

2.3.1 Cross Ply Layup

Initial analysis was performed using a cross ply $[0/90]_S$ specimen. Cross ply laminates have low poisson's effects, hence this layup exhibited minimal biaxial strengthening. A circular central hole was cut in the gage region to increase stress and ensure failure in the gage region. The optimized design parameters for the cross ply specimen geometry are

presented in Table 2.2. Design validation was performed using an ARAMIS digital image correlation (DIC) system to measure the strain fields. As shown in Figure 2.3, the biaxial strain field in the cross ply geometry satisfies the design requirements. The optimized cross ply geometry is presented in Figure 2.4.

Table 2.2. Optimized Cross Ply Specimen Parameters

Parameter Name	Explanation	Optimized Parameters (cm)
l	Specimen length	25.4
w	Arm width	7.62
d_{cutout}	Diameter of cutout between adjacent arms	3.05
h_{offset}	Offset distance from cutout center to arm edge	0.508
$r_{smallfillet}$	Fillet radius between cutout and arms	1.27
D	Center hole diameter	0.94

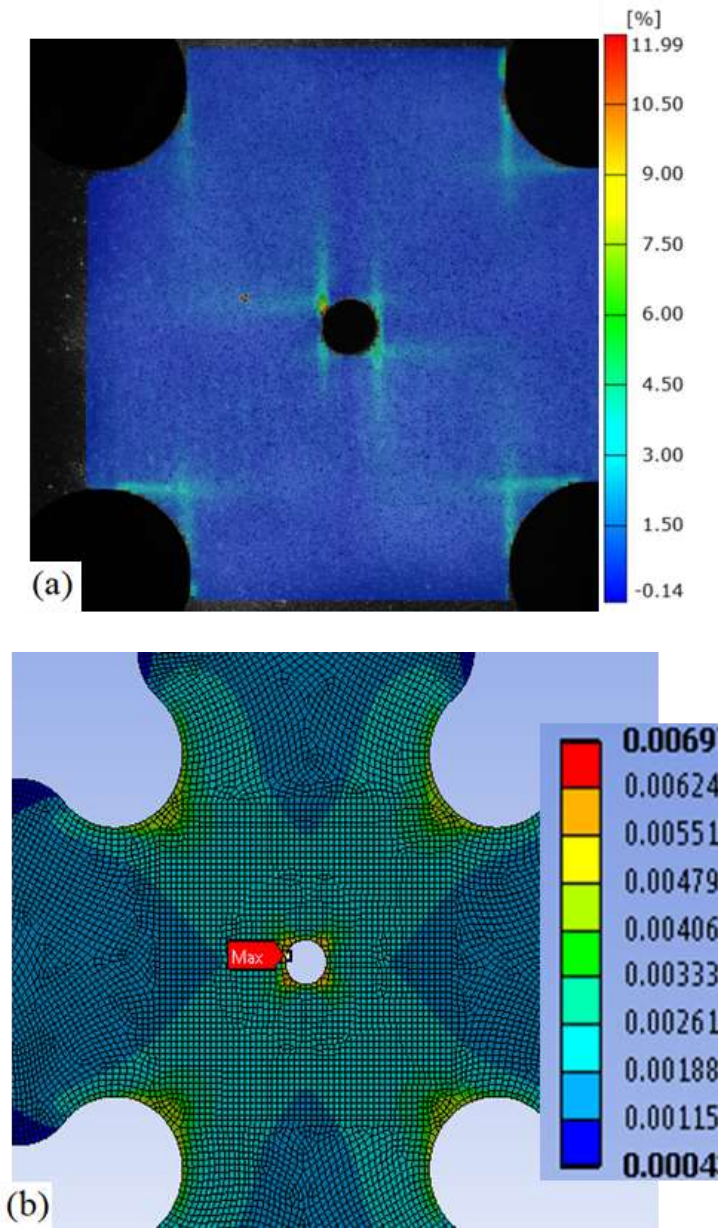

Figure 2.3. Cross Ply Cruciform Equivalent Strain Profiles. (a) DIC Image from Static Biaxial Load Test; (b) ANSYS FEM Simulation

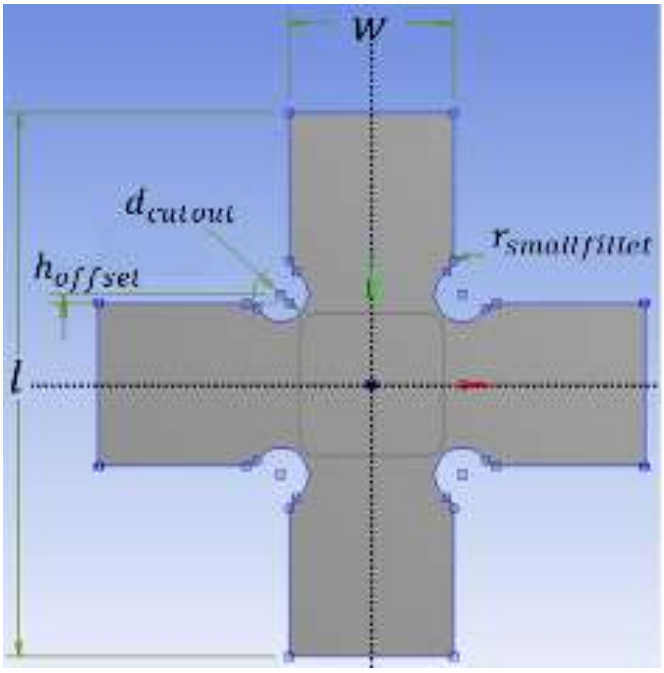

Figure 2.4. Optimized Cross Ply Specimen Geometry

2.3.2 Quasi Isotropic Layup

The design process was repeated for a quasi isotropic $[0/45/-45/90]_S$ layup using the design requirements and optimization methodology explained previously. Specimen length and width were kept the same as the cross ply specimens to keep specimen size consistent and to reduce the number of design parameters. Due to high poisson effects, quasi isotropic laminates are susceptible to biaxial strengthening, and the optimized cruciform reflects geometrical changes that mitigate the effects of biaxial strengthening. For example, the width of the quasi isotropic cruciform arms gradually decreases near the gage region. This increases the cross sectional area of the arms relative to that of the gage region to increase stress in the biaxially loaded gage region. Additionally, a circular central hole was insufficient to ensure failure in the gage region, so an ellipse was introduced. The length and orientation of major and minor axes of the ellipse were used as design parameters in

the optimization, and sensitivity analysis was performed to ensure that minor changes in the orientation and size of the ellipse did not result in significant changes to the strain field. As shown in Figure 2.5, the ellipse decreases the uniformity of the gage region strain field, but the strain along the damage path (red dashed line) remains relatively constant, so damage still propagates through a region of uniform biaxial strain. DIC strain analysis shows good agreement with the FE analysis, and both maximum strain and Tsai-Wu failure theories predict failure initiation in the gage region. The optimized quasi isotropic specimen geometry is shown in Figure 2.6 and the optimized parameters are presented in Table 2.3.

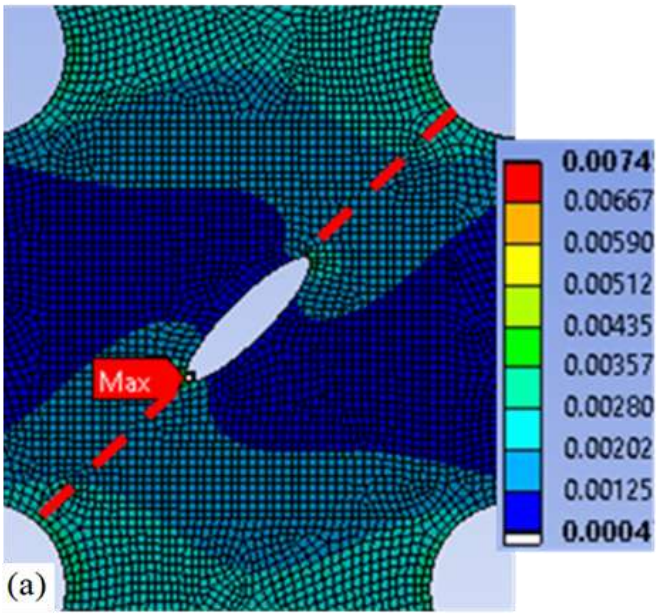

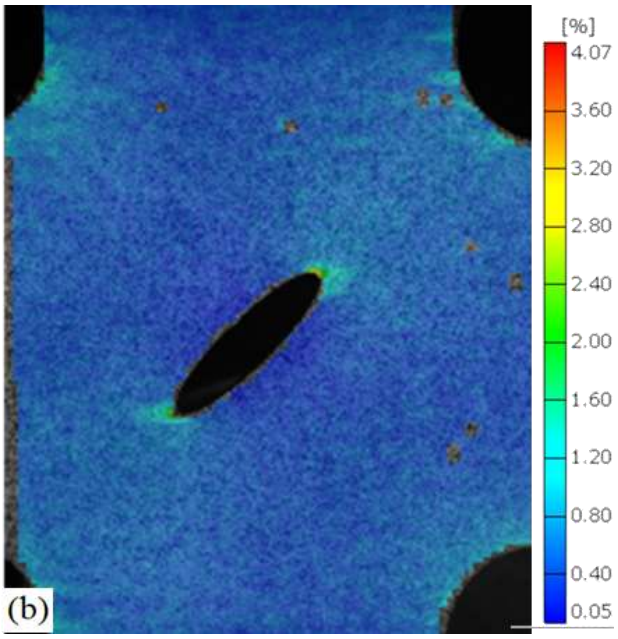

Figure 2.5. Quasi Isotropic Specimen Equivalent Strain Profiles. (a) ANSYS FEM Simulation; (b) DIC Image from Static Biaxial Load Test

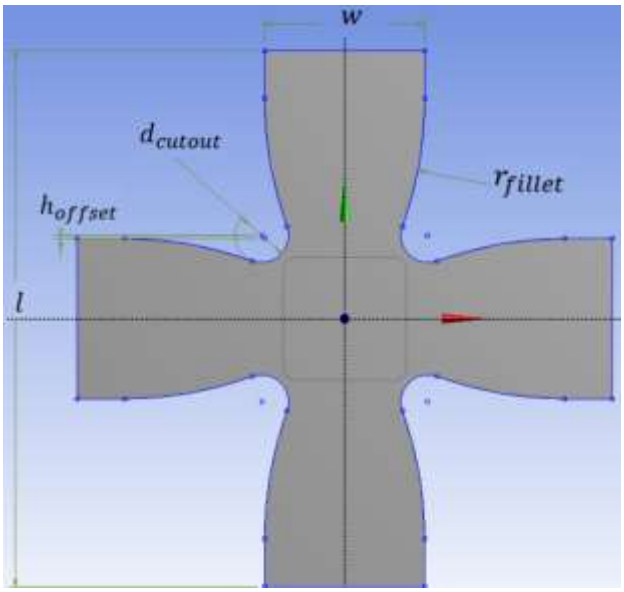

Figure 2.6. Optimized Quasi Isotropic Specimen Geometry

Table 2.3. Optimized Quasi Isotropic Specimen Parameters

Parameter Name	Explanation	Optimized Parameters (in)
l	Specimen length	25.4
w	Arm width	7.62
d_{cutout}	Diameter of cutout between adjacent arms	2.54
h_{offset}	Offset distance from cutout center to arm edge	0.127
r_{fillet}	Fillet radius between cutout and arms	17.78
a	Ellipse major axis	1.27
b	Ellipse minor axis	0.305
θ	Ellipse angle	45°

2.4 Results and Discussion

2.4.1 Cross Ply at Baseline Load

Fatigue tests were conducted across a range of loadings and the intermediate loading case ($P_{max} = 27kN, R = 0.1$) was established as a baseline for investigating biaxial fatigue damage mechanisms in the cross ply specimens. Specimen stiffness in both horizontal and vertical directions was monitored to correlate stiffness degradation to damage in surface and subsurface fiber directions. At these loads, specimen stiffness degrades sigmoidally in both ply orientations. Stiffness degrades rapidly during stage 1 of the fatigue test (see Figure 2.7) primarily due to material relaxation and matrix crazing

(Peng, Liu, Saxena, & Goebel, 2015). The primary damage mechanisms at this level of fatigue are matrix microcracks which initiate in the resin-rich intertow regions of the surface plies. The transition from stage 1 to stage 2 of fatigue occurs at about 10% fatigue life and damage begins to propagate from the initial matrix cracks.

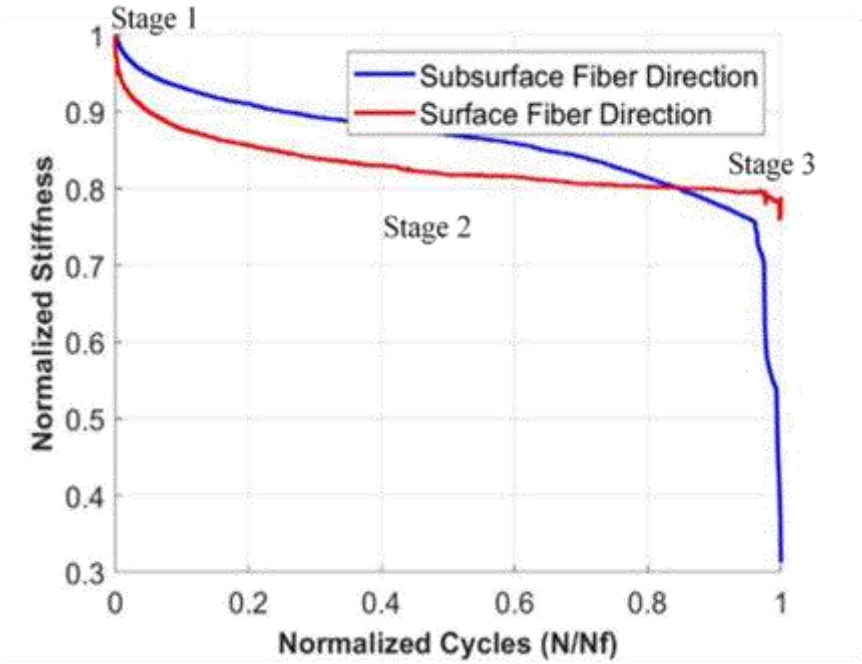

Figure 2.7. Baseline Stiffness Plot for Cross Ply Specimen With R=0.1

The optimized $[0/90]_S$ cruciform at 10% fatigue life is shown in Figure 2.8. At this level of fatigue, the initial matrix microcracks begin to coalesce and cause transverse tow separation. The SEM micrograph in Figure 2.8 (b) shows matrix serrations protruding into an initiating tow separation. These matrix serrations are only seen in the transition between stage 1 and stage 2 of fatigue and are the result of crazing and void formation in the matrix before fiber/matrix separation (Greenhalgh, 2009). After the fiber and matrix separate, the crack grows along the fiber/matrix interface, resulting in a smooth crack profile as shown

in Figure 2.9 (b). As the fatigue test progresses, the cracks are pulled open and the surface ply transverse tow separation begins.

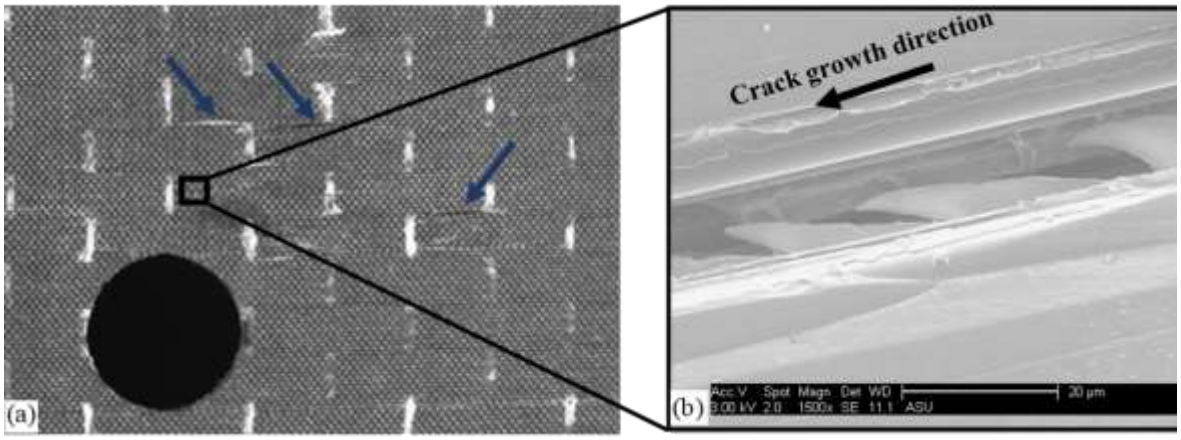

Figure 2.8. Baseline Cross Ply Fatigue Specimen at 10% Fatigue Life. (a) Matrix Cracks Initiate Between Fiber Tows and Cause Transverse Tow Separation; (b) SEM Micrograph of Serrated Separation in Stage 1 of Fatigue

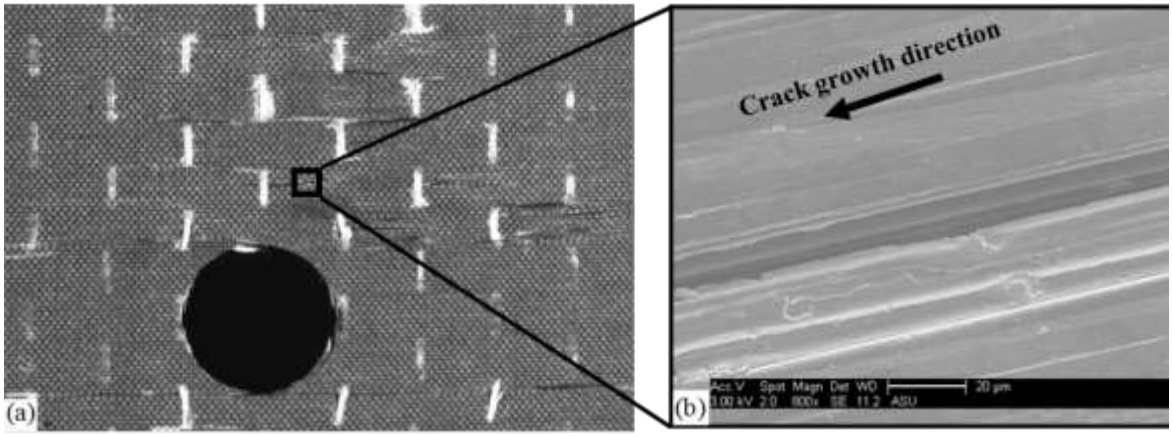

Figure 2.9. Baseline Cross Ply Fatigue Specimen at 50% Fatigue Life. (a) Additional Matrix Cracks and Increased Fiber/matrix Separation; (b) SEM Micrograph of Smooth Fiber/matrix Separation in Stage 2 of Fatigue

As the specimen enters the second stage of fatigue, the rate of stiffness degradation decreases and matrix cracking dominates. The transverse tow separations that initiated in stage 1 of fatigue extend further and propagate parallel to the fibers. At about 50% fatigue life, the stiffness in the subsurface ply direction begins to degrade at a higher rate relative to the surface ply direction. This is because at the low biaxial strains induced by these loadings (0.7% strain at peak loading), the subsurface plies in specially orthotropic cross ply layups have higher crack density than the surface plies (Montesano & Singh, 2015), leading to degraded stiffness in the subsurface fiber direction. Additionally, the growth of surface ply transverse separation contributes to more rapid property degradation in the subsurface fiber direction. By about 80% fatigue life the rate of subsurface ply direction stiffness degradation increases further as the locally failed regions combine. Fatigue failure occurs shortly thereafter.

The final stage of fatigue is characterized by an abrupt drop in stiffness as subsurface fiber breakage and pullout occurs. At these loads, failure occurs first in the subsurface plies because of the transverse separation in surface fiber tows and because of the higher crack density in subsurface plies at low equibiaxial strains (Montesano & Singh, 2015). The surface ply transverse separation decreases the load capacity of the surface plies and causes load redistribution. This increases subsurface ply degradation and leads to longitudinal failure in the subsurface plies. Figure 2.10 (a) shows that subsurface fiber failure occurred directly beneath the surface ply transverse separation and the SEM micrograph in Figure 2.10 (b) shows longitudinal fiber fracture.

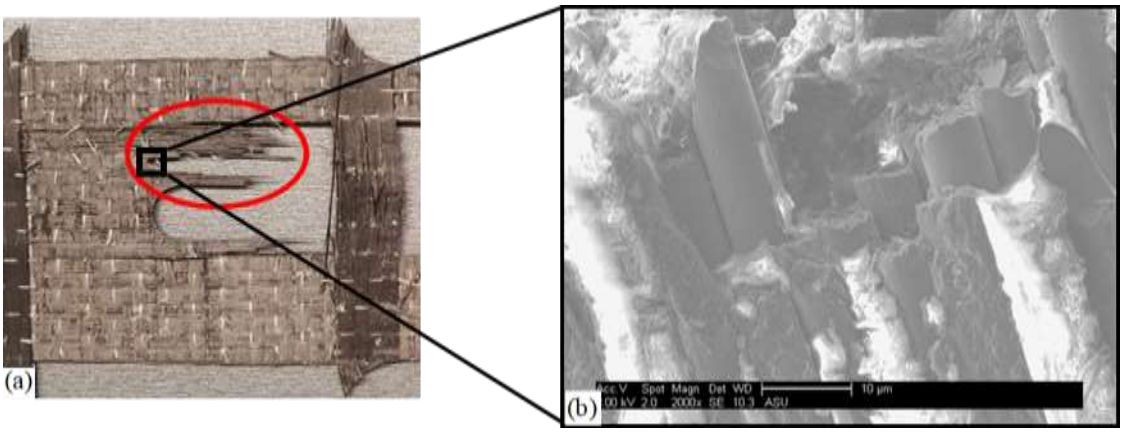

Figure 2.10. Fatigue Failure in Subsurface Plies. (a) Failed Specimen; (b) SEM Micrograph Showing Longitudinal Subsurface Fiber Fracture

When the R ratio is increased to 0.3, fatigue life is increased and damage mechanisms such as fiber/matrix separation and transverse tow separation are delayed. As shown in Figure 2.11, matrix cracks in surface plies propagate parallel to fibers with no transverse tow separation, which is delayed until approximately 75% fatigue life. Despite an increase in mean stress with higher R ratio, stress amplitude is lower and damage is less severe. The cross ply intermediate loading case with R ratio 0.3 showed damage behavior and delayed damage mechanisms similar to the low load case with R=0.1. At these loadings, failure initiates in subsurface plies.

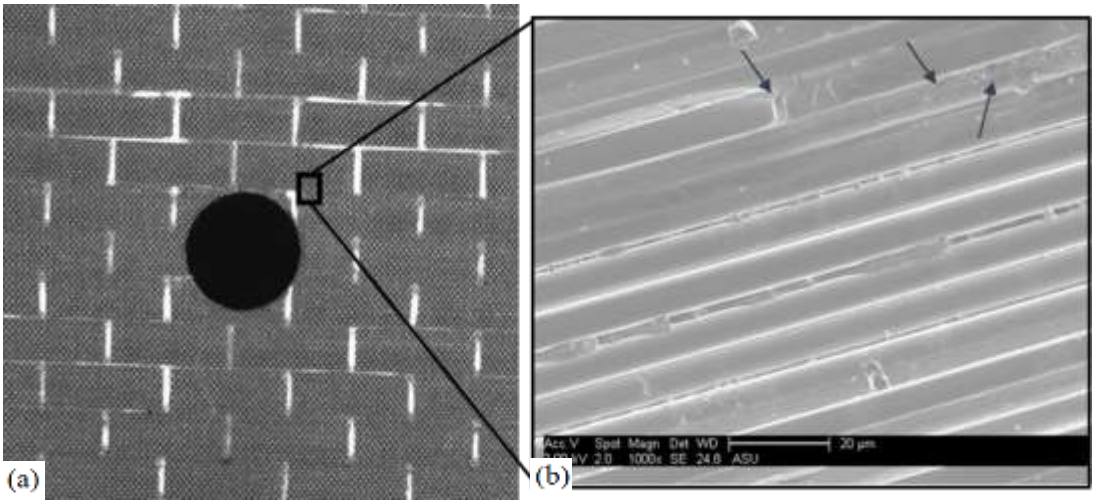

Figure 2.11. Baseline Cross Ply Fatigue Specimen With R=0.3 at 50% Fatigue Life. (a) Mesoscale Matrix Cracks Between Tows (b) SEM Micrograph Showing Matrix Voids and Microcracks in Resin-rich Intertow Areas

2.4.2 Cross Ply at Low Load

At low loads ($P_{max} \leq 25kN, R = 0.1$), stiffness in both surface and subsurface ply directions degrades sigmoidally (see Figure 2.12), and matrix damage mechanisms dominate. Intertow matrix microcracks at 10% fatigue life are shown in Figure 2.13 and matrix cracking between fiber tows at 50% fatigue life are shown in Figure 2.14, but fiber/matrix separation is delayed until almost 70% fatigue life at these loads. Stiffness in both surface and subsurface ply directions degrade at essentially the same rate until approximately 75% fatigue life, when stiffness in the subsurface fiber direction begins to degrade at a higher rate relative to that of the subsurface fiber direction. When fatigue reaches approximately 90% fatigue life, subsurface ply direction stiffness crosses below that of the surface ply and failure occurs soon after. At low loads, failure occurs first in the subsurface plies due to higher subsurface ply crack density as in the baseline case.

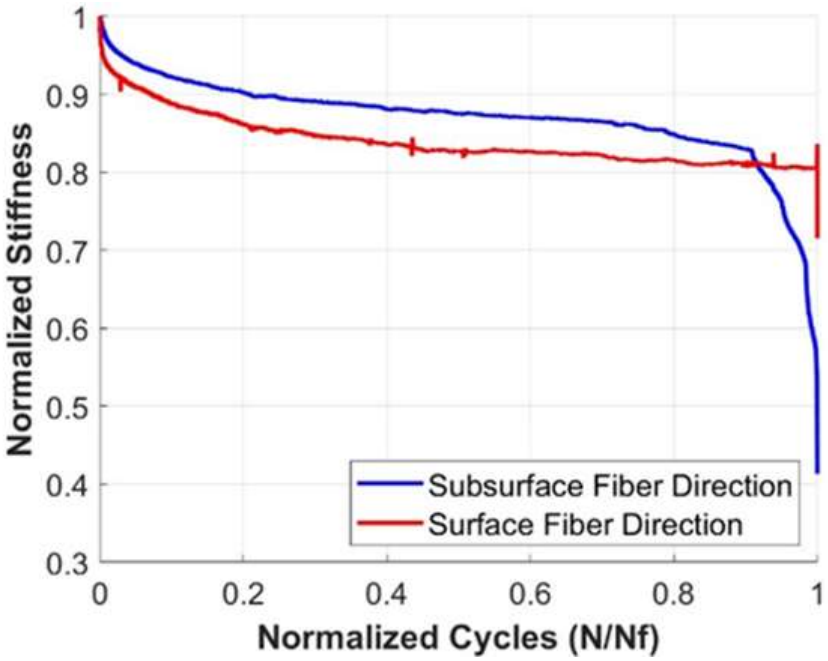

Figure 2.12. Low Load Stiffness Plot for Cross Ply Specimen with R=0.1

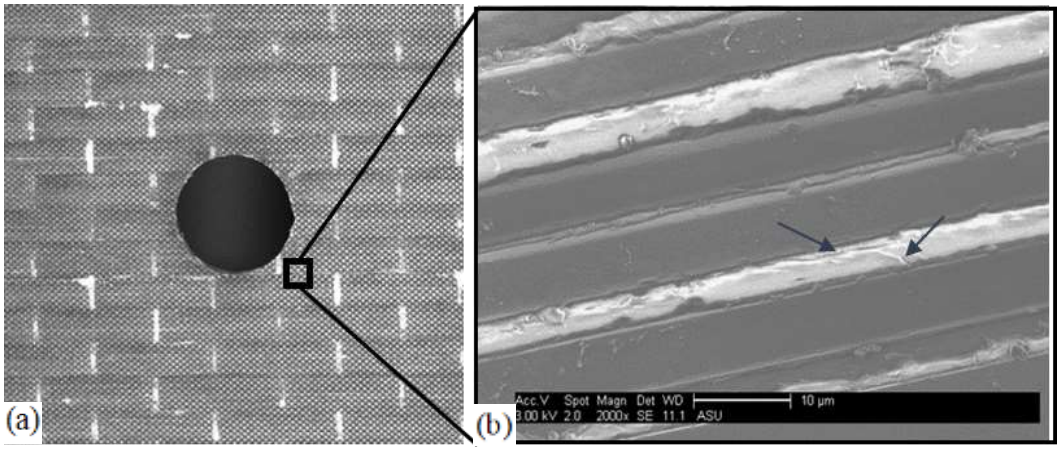

Figure 2.13. Low Load Specimen at 10% Fatigue Life. (a) Surface Ply Transverse Matrix Cracks; (b) SEM Micrograph of Matrix Microcracks in Resin-rich Intertow Area

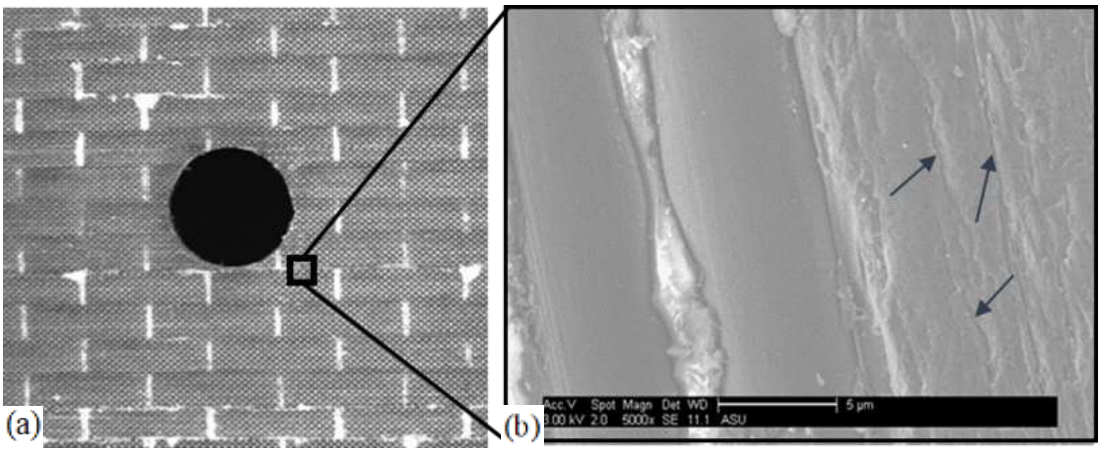

Figure 2.14. Low Load Specimen at 50% Fatigue Life. (a) Surface Ply Transverse Matrix Cracks; (b) SEM Micrograph of Matrix Cracks Between Fiber Tows

When the R ratio is increased to 0.3, fatigue life is significantly extended. Minor matrix cracking occurs between fibers, but no significant fiber/matrix separation occurs. The low load case fatigue tests with R=0.1 takes about 1×10^6 cycles to reach failure, but with R=0.3 the tests reach past 2.5×10^6 cycles without failure. Even at 500,000 cycles, very minor matrix cracking and crazing occurs (see Figure 2.15).

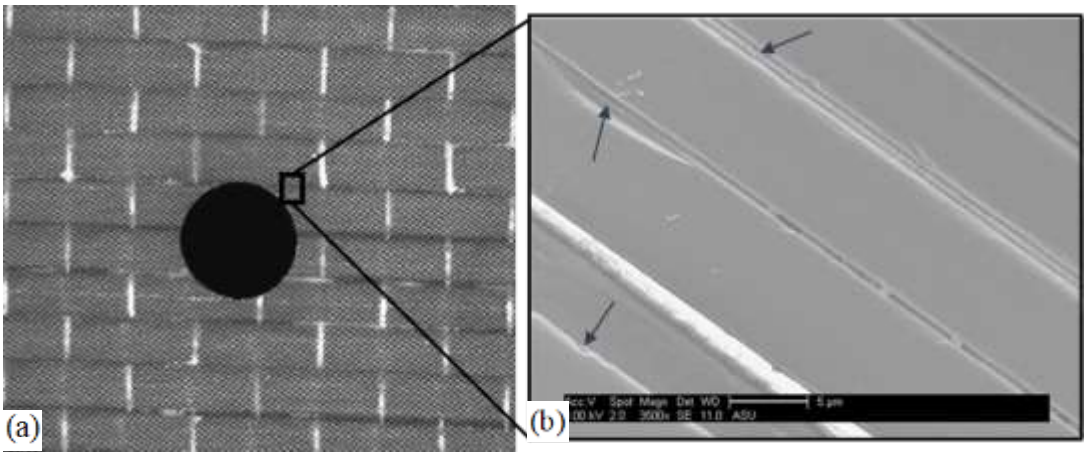

Figure 2.15. Low Load Cross Ply Load Case with R=0.3. (a) Minor Mesoscale Gage Region Damage; (b) SEM Micrograph Showing Minor Matrix Microcracking

2.4.3 Cross Ply at High Load

When the load is increased ($P_{max} \geq 30kN, R = 0.3$), property degradation in both surface and subsurface ply directions shows an approximately linear behavior as shown in Figure 2.16. Fiber damage mechanisms such as fiber pull out, fiber fracture, and fiber/matrix separation near the center hole dominate. Fiber pull out and fiber breakage between separated tows are shown in Figure 2.17, but even at 85% fatigue life there is little observable matrix damage away from the center hole and damage in the gage region is highly localized around the severe transverse separation near the center hole. Transverse matrix cracks initiate near the center hole and almost immediately cause transverse separation of surface fibers in this region. These loading conditions cause approximately 1.2% biaxial strain at peak load. Due to high biaxial strain, the surface ply direction stiffness degrades at a higher rate than that of the subsurface ply direction and fatigue failure occurs first in the surface plies. This experimental observation is supported by the literature, which shows that above approximately 0.8% biaxial strain, the 0º surface plies of a cross ply laminate have higher crack density than the 90º subsurface plies (Montesano & Singh, 2015).

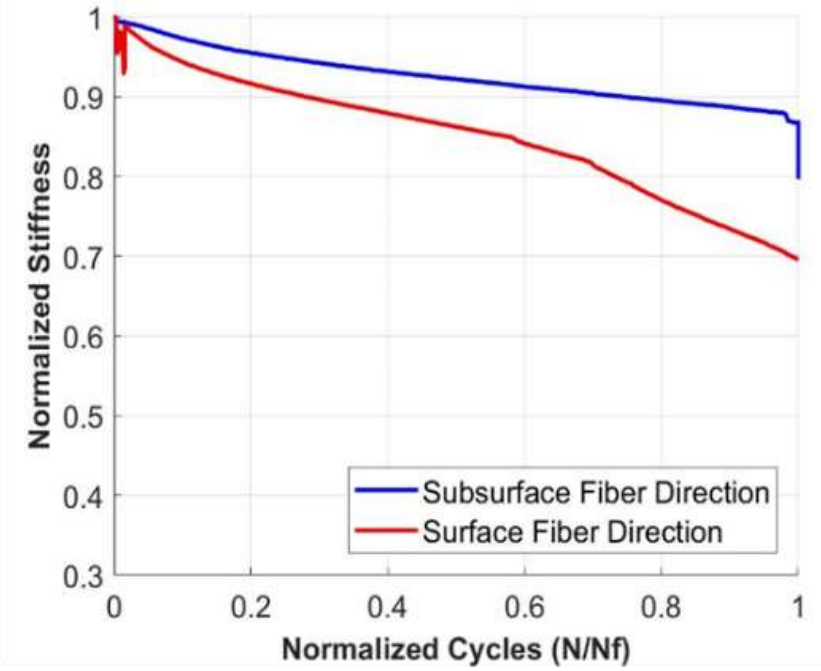

Figure 2.16. Stiffness Plot for Cross Ply Specimen High Load Case

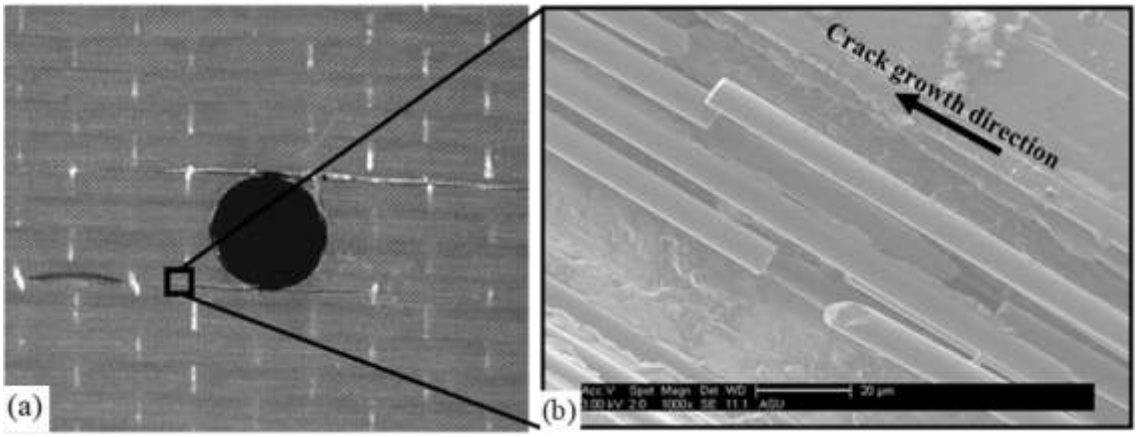

Figure 2.17. High Load Specimen at 50% Fatigue Life. (a) Transverse Separation in Surface Tows; (b) SEM Micrograph of Fiber Breakage Inside Tow Separation

Increasing the R ratio from 0.1 to 0.3 for the high load case extends the fatigue life and results in more evenly distributed damage throughout the gage region. For the high loading case with R=0.3 at 50% fatigue, Figure 2.18(a) shows that surface ply transverse separation

is severe, but matrix cracking and tow separation are visible away from the center hole. Additionally, Figure 2.18(b) shows that no fiber pull out or fiber fracture occurs.

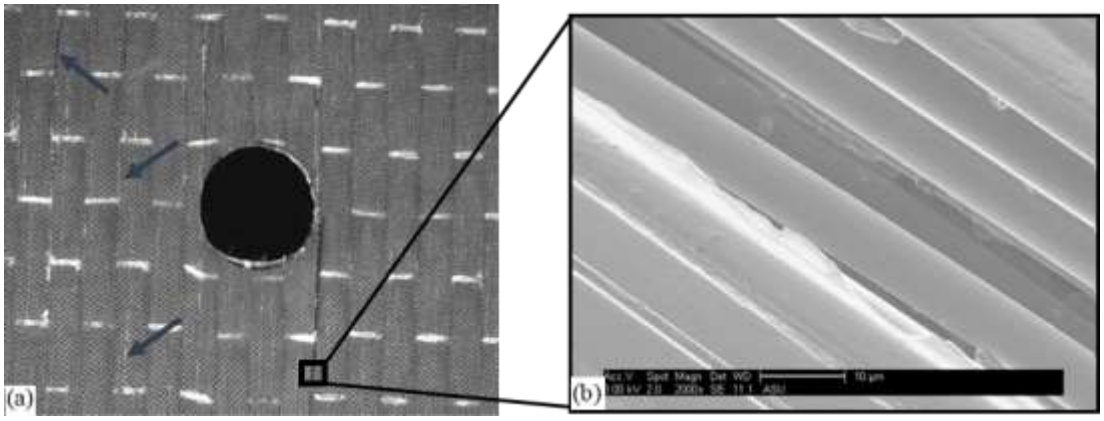

Figure 2.18. High Load Specimen at 50% Fatigue Life. (a) Transverse Separation in Surface Tows; (b) SEM Micrograph of Fiber Breakage Inside Tow Separation

2.4.4 Quasi Isotropic Low Load

Similar biaxial fatigue tests were performed for the quasi isotropic laminates and specimen stiffness in the horizontal and vertical directions was recorded to determine the effect of stacking sequence on composite biaxial fatigue damage behavior. The specimens were oriented with the 0° plies aligned in the vertical direction. In the low load case for quasi isotropic laminates ($P_{max} < 35kN$), specimen stiffness degrades rapidly during the first 10% of fatigue life (stage 1) as matrix microcracking and material relaxation occurs (see Figure 2.19). At the beginning of stage 2, between approximately 10% and 20% fatigue life, the rate of stiffness degradation decreases as matrix microcracks reach saturation and more stable matrix cracks form, leading to transverse ply cracks. At these loads, transverse cracks form in the -45° plies between approximately 20% and 40%

fatigue life, causing interfacial debonding near the tips of the transverse cracks as shown in Figure 2.20(a). In these images, the blue arrows indicate transverse ply cracks, blue ovals indicate interfacial debonding at the tips of transverse cracks, and the gold arrows indicate delamination. By approximately 60% fatigue life, delamination occurs between the -45° and 90° plies as a result of this interfacial debonding, and transverse cracks that formed in additional plies cause additional interfacial debonding as shown in Figure 2.20(b). After 60% fatigue life, the delaminated regions between plies grow and the locally failed regions find a path that leads to increased material degradation (Talreja R. , 1986). The 45° and -45° plies fail shortly after, at approximately 75% fatigue life. This results in a precipitous drop in stiffness followed by rapid sigmoidal stiffness degradation as load is redistributed to the remaining plies.

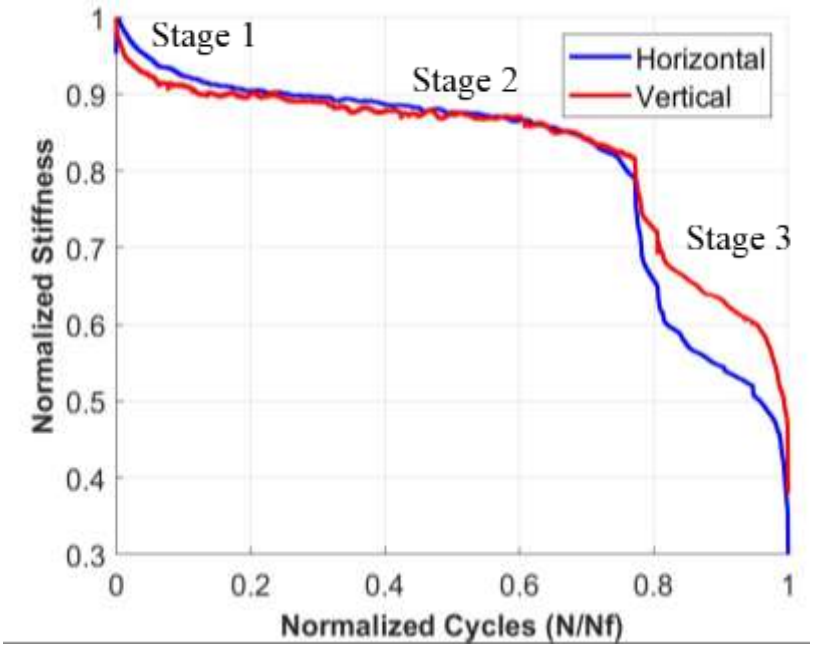

Figure 2.19. Low Load Stiffness Plot for Quasi Isotropic Laminates

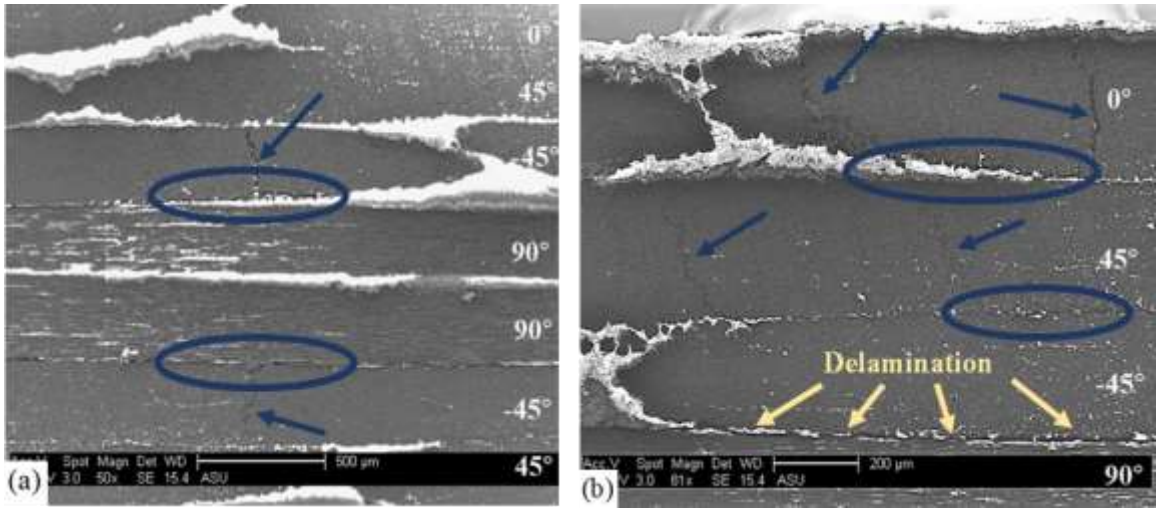

Figure 2.20. SEM Micrographs of Low Load ($P_{max} = 30kN$) Quasi Isotropic Specimen Cross Section. (a) Transverse Cracks and Interfacial Debonding at 30% Fatigue Life; (b) Transverse Cracks, Debonding, and Delamination at 60% Fatigue Life

2.4.5 Quasi Isotropic Intermediate Load

Quasi isotropic laminates subjected to intermediate biaxial fatigue loadings ($35kN \leq P_{max} \leq 40kN$) showed increased stiffness degradation and accelerated formation and propagation of biaxial fatigue damage mechanisms. Figure 2.21 shows that stiffness degrades rapidly during the first 10% of fatigue due to material relaxation and matrix microcracking. At these loadings, the normalized stiffness in both horizontal and vertical directions fell below 0.9 by 20% fatigue life compared to the low load case which required approximately 40% of fatigue life for normalized stiffness to fall below 0.9. In addition to increased stiffness degradation, the onset of delamination was accelerated compared to the low load case. By 30% fatigue, interactions between transverse cracks in the outer plies lead to delamination as shown in Figure 2.22(a). In these images, the blue arrows indicate transverse ply cracks and the gold arrows indicate delamination. As fatigue cycles increase,

these damage mechanisms progress as additional transverse cracks form and cause further delamination to occur. By 60% fatigue life, delamination becomes the dominating damage mechanism as shown in Figure 2.22(b). Specimen stiffness further degrades as the delaminated regions grow, and the 45° and -45° plies fail at approximately 75% fatigue life as a result. A sharp drop in specimen stiffness occurs as the load is redistributed to the remaining plies, which degrade rapidly before final biaxial fatigue failure.

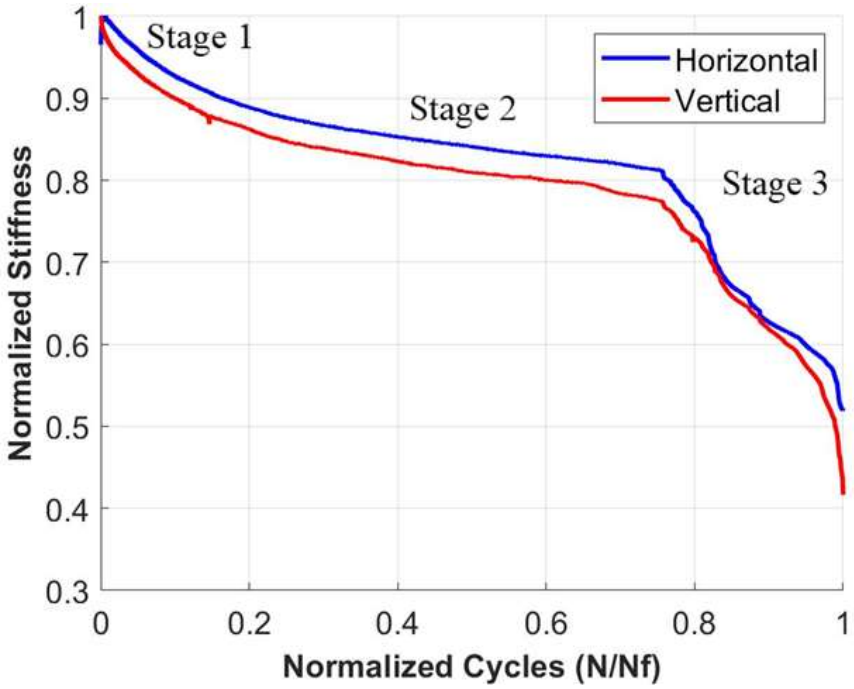

Figure 2.21. Intermediate Load Stiffness Plot for Quasi Isotropic Specimen

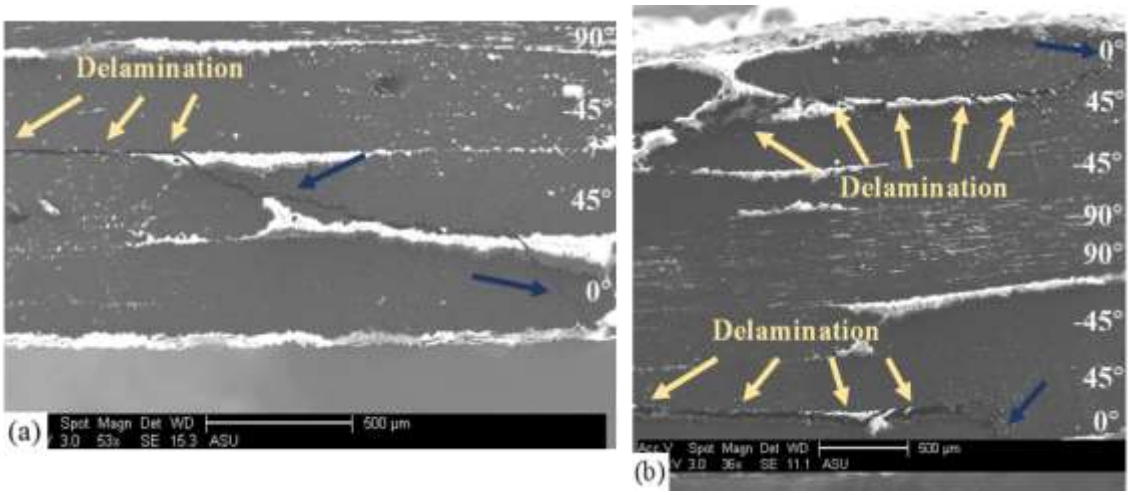

Figure 2.22. SEM Micrographs of Intermediate Load ($P_{max} = 35kN$) Quasi Isotropic Specimen Cross Section. (a) Transverse Cracks and Delamination at 30% Fatigue Life; (b) Transverse Cracks and Severe Delamination at 60% Fatigue Life

2.4.6 Quasi Isotropic High Load

When subjected to the high load case ($P_{max} > 40kN$), the stiffness degradation in quasi isotropic laminates behaves almost linearly (see Figure 2.23) before failure initiates in the 45° and -45° plies at around 70% fatigue life. At these loadings, initiation and propagation of biaxial fatigue damage mechanisms are accelerated and the damage mechanisms, especially delamination, are more severe. By 30% fatigue life, significant delamination occurs at the tips of transverse cracks in the surface plies as shown in Figure 2.24(a). Additional transverse cracks form in the inner plies and interact with the growing delaminated areas, resulting in the cross section shown in Figure 2.24(b). Severe transverse cracks in the 45° and -45° plies (indicated with red arrows) allow delamination to jump between the ply interfaces causing almost complete layer separation. This interaction between transverse cracks and delamination leads to failure in the 45° and -45° plies at

approximately 70% fatigue life, followed by rapid degradation in the remaining plies. At lower loads, specimen stiffness degrades sigmoidally after the 45° and -45° plies fail and load is redistributed to the remaining plies. In the high load case, however, the extent of damage in the 0° and 90° plies and the severity of the delamination between each layer precludes smooth stiffness degradation as the remaining plies reach ultimate fatigue failure.

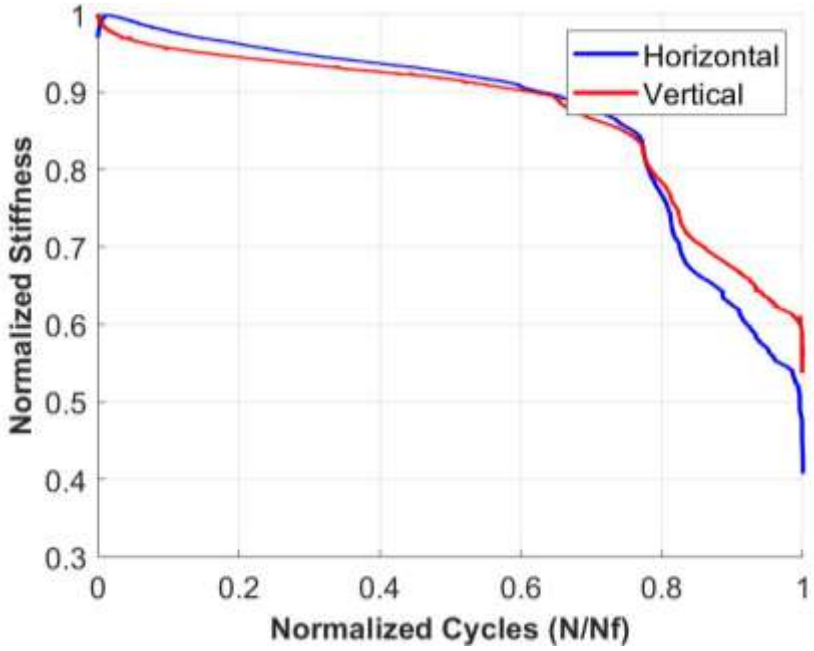

Figure 2.23. High Load Stiffness Plot for Quasi Isotropic Specimen

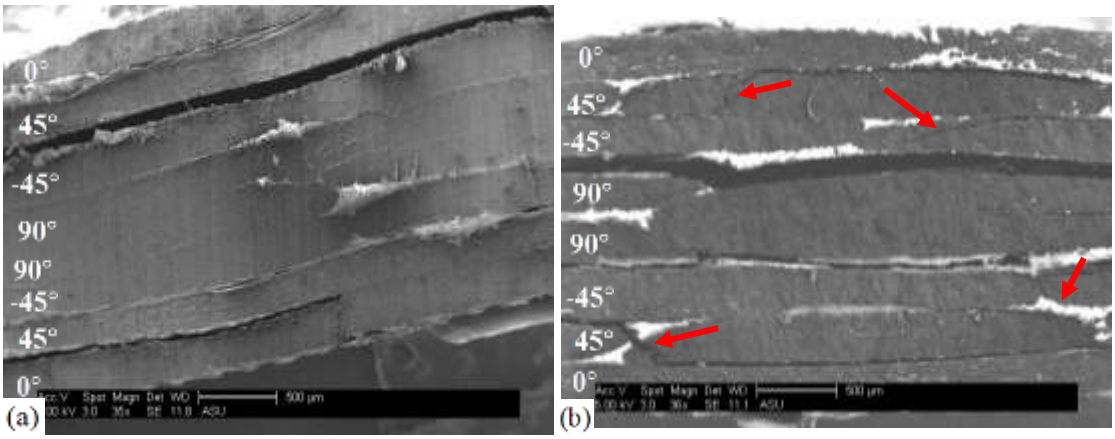

Figure 2.24. SEM Micrographs of High Load ($P_{max} = 40kN$) Quasi Isotropic Specimen Cross Section. (a) Severe Delamination at 30% Fatigue Life; (b) Ply Fracture in +/-45° Plies and Severe Delamination at 60% Fatigue Life

2.5 Fabrication of CNT-enhanced CFRP Composites

Carbon nanoparticles have the potential to impart multifunctional properties, such as enhanced fatigue life, damage resistance, and self-sensing capabilities to otherwise mundane materials. Datta et al. (Datta, Neerukatti, & Chattopadhyay, 2018) investigated the effects of embedding a CNT membrane called buckypaper between layers of a glass fiber reinforced polymer (GFRP) composite subjected to uniaxial fatigue loading. They found that the electrical resistance of the specimens changed with increasing fatigue cycles and successfully correlated the resistance changes to crack length in the buckypaper-enhanced GFRP specimens. In addition to the self-sensing capabilities, they reported that the buckypaper decreased the fatigue crack growth rate by an order of magnitude and doubled the fatigue life as a result of crack tip blunting during fatigue. In the continuation of the work described in this chapter, buckypaper membranes have been manufactured and embedded within the gage region of the optimized CFRP cruciform specimens. Figure 2.25 and Figure 2.26 show the placement of the buckypaper membranes. Biaxial fatigue tests will be conducted, and the damage behavior of the nano-enhanced specimens will be investigated. The nucleation and propagation of damage mechanisms will be investigated using SEM fractography techniques and correlated to external loading, stacking sequence, and the placement of the buckypaper membrane within the specimen gage region.

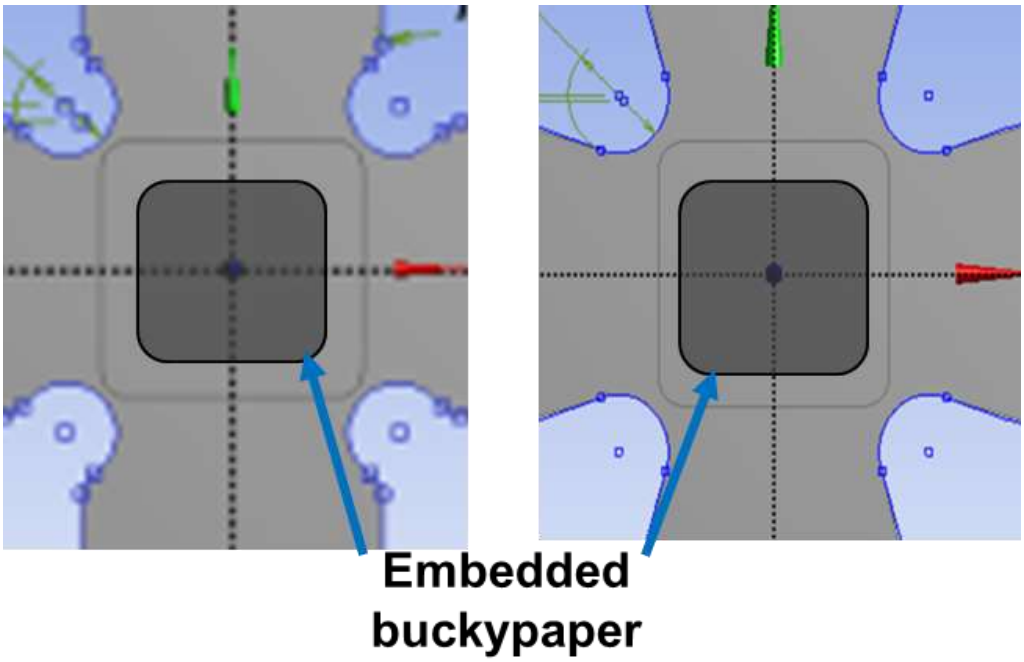

Figure 2.25. Placement of Buckypaper Membrane in Optimized Cruciform Gage Region

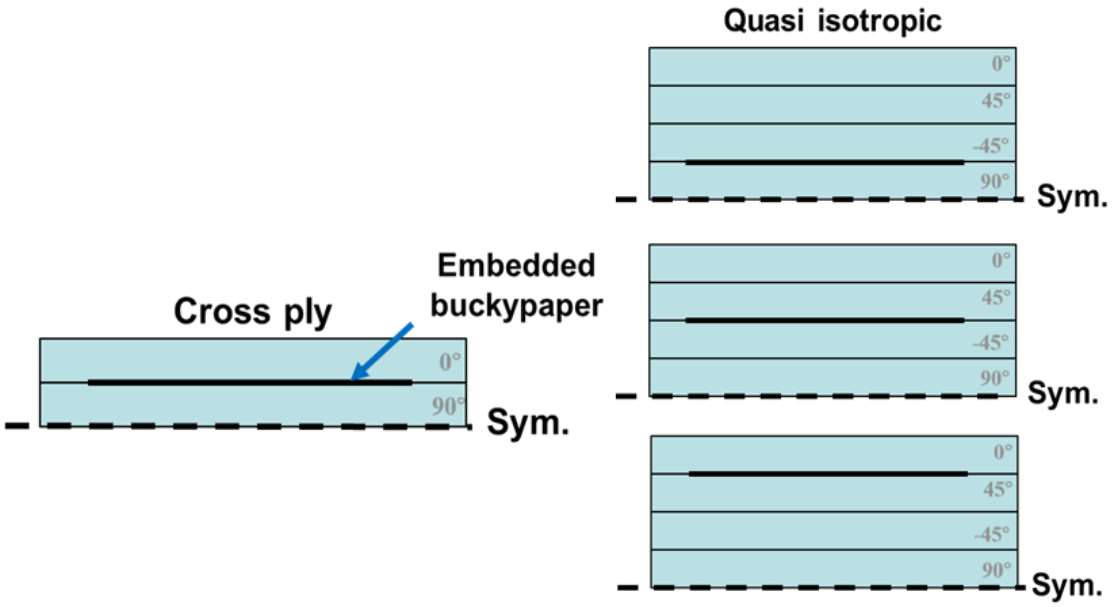

Figure 2.26. Cross Sectional View of Buckypaper Membrane Placement in Optimized Cruciform Gage Region

2.6 Conclusions

Optimized composite cruciform specimens were designed and in plane constant amplitude biaxial fatigue tests were performed to investigate the initiation and progression of biaxial fatigue damage mechanisms in $[0/90]_S$ and $[0/45/-45/90]_S$ CFRP laminates. Microscale damage mechanisms were studied using SEM fractography and were correlated to material property degradation and biaxial fatigue loading parameters. Additionally, nano-enhanced CFRP laminates have been fabricated to investigate the effects of buckypaper membranes on the biaxial fatigue damage behavior of CFRP composites. The following are some key observations from this study: Cross ply laminate stiffness degrades sigmoidally for low and intermediate load cases and is approximately linear for high load cases. Transverse matrix cracks and transverse tow separation in surface plies lead to subsurface longitudinal ply failure for the low and intermediate load cases, while high biaxial loading causes severe transverse tow separation, highly localized damage, and failure in the subsurface plies. Increasing the R ratio extends fatigue life, delays damage mechanisms, and causes a more uniform distribution of damage in the gage region. In the Quasi isotropic laminates, failure occurs in the 45° and -45° plies followed by rapid sigmoidal property degradation as load redistributes to the remaining plies. Delamination occurs at the tips of transverse ply cracks and is the dominant damage mechanisms in quasi isotropic laminates, especially in the high load case. The observations obtained in this study provide important insight into the damage mechanisms that govern the overall damage behavior of CFRP composites under external biaxial fatigue loading.

3 FRACTURE MECHANICS-INFORMED DAMAGE MODEL FOR CERAMIC MATRIX COMPOSITES

3.1 Introduction

In this chapter, a fracture mechanics-informed damage model is developed and implemented within the MSGMC framework to account for the multiscale nature of matrix damage initiation and propagation in CMCs. The material stress-strain constitutive relationship is derived using ISV theory and a damage ISV is defined to capture the effects of both micro- and macroscale matrix cracks that initiate from manufacturing induced cavities. The damage variable is a function of the crack density in the matrix and is determined using fracture mechanics and the self-consistent scheme (Budiansky & O'Connell, 1976). Matrix cracking is activated when stress intensity factors exceed the fracture toughness of the material and crack growth kinetics govern the growth of cracks and the progression of damage in the matrix. An additional ISV is defined as a function of volumetric strain to describe porosity nucleation and growth within the ceramic matrix material. Accounting for porosity effects in addition to matrix cracking enhances the nonlinear predictive capability of the model and captures key physics of deformation and damage in CMCs that are often overlooked when only considering matrix cracking. The model is applied to monolithic SiC, UD C/SiC CMC, and a 5 harness satin (HS) woven C/SiC CMC using SiC and carbon fiber material properties obtained from literature.

This chapter is organized as follows: Section 3.2 describes the fracture mechanics-informed matrix damage model. Section 3.3 discusses the multiscale modeling framework used to simulate the woven CMC. Section 3.4 presents modeling results for monolithic

SiC, UD C/SiC, and woven C/SiC and compares the woven CMC simulation results to experiments from literature. Section 3.5 presents a temperature-dependent reformulation of the fracture mechanics-informed matrix damage model. The final section concludes the chapter and highlights the key findings of the chapter.

3.2 Description of Damage Model

3.2.1 Thermodynamic Framework

The governing equations of the ISV approach are obtained by combining the first and second laws of thermodynamics to obtain a dissipation inequality (Clausius-Duhem inequality):

$$\dot{\psi} + s\dot{\theta} - \frac{1}{\rho}\boldsymbol{\sigma}\colon \boldsymbol{D} + \frac{1}{\rho\theta}\boldsymbol{q}\cdot\boldsymbol{\nabla}(\theta) \leq 0, \tag{3.1}$$

where ψ is the Helmholtz free energy, s is entropy, θ is temperature, ρ is density, $\boldsymbol{\sigma}$ is the Cauchy stress tensor, $\boldsymbol{D}$ is the symmetric part of the velocity gradient ($\boldsymbol{D} = \dot{\boldsymbol{\varepsilon}}$ for small strains), and $\boldsymbol{q}$ is the heat flux. The Helmholtz free energy is taken as the scalar state potential of the material, meaning that it governs the evolution of state variables, and is a function of the external state variables (elastic strain and temperature) and internal state variables (α_i):

$$\psi = \hat{\psi}(\boldsymbol{\varepsilon}^e, \theta, \alpha_i). \tag{3.2}$$

The ISVs can be chosen to represent specific damage mechanisms. In this case, two isotropic ISVs, D_c, and D_p, are chosen to represent the damaged state of the material, and

an additional state variable, ξ, which captures the effects of irreversible grain boundary sliding and contributes to the inelastic material behavior. D_c depends on the activation and propagation of matrix cracks near manufacturing-induced cavities, and D_p depends on the nucleation and growth of pores due to microstructural deformation with increasing volumetric strain. The Helmholtz free energy is divided into elastic and inelastic parts so that:

$$\psi = \psi^e + \psi^I. \tag{3.3}$$

Assuming that the elastic part of the free energy is completely described by the strain potential for linear thermo-elasticity, the elastic Helmholtz free energy is:

$$\psi^e = \frac{1}{\rho}\left(\frac{1}{2}\varepsilon_{ij}\sigma_{ij} + \alpha(\theta - \theta_0)\delta_{ij}\right). \tag{3.4}$$

Applying the principle of strain equivalence for a damaged medium and simplifying, Equation (3.4) becomes:

$$\psi = \frac{1}{\rho}\left(\frac{1}{2}\varepsilon_{ij}^e C_{ijkl}\varepsilon_{kl}^e(1 - D_c)(1 - D_p) + \alpha(\theta - \theta_0)\delta_{ij}\right), \tag{3.5}$$

where C_{ijkl} is the forth-order stiffness tensor, α is the coefficient of thermal expansion, and δ_{ij} is the Kronecker-delta function. The thermoelastic law derived from this potential is:

$$\sigma_{ij} = \rho\frac{\partial\psi}{\partial\varepsilon_{ij}} = C_{ijkl}\varepsilon_{kl}^e(1 - D_c)\big(1 - D_p\big). \tag{3.6}$$

To fully describe the thermoelastic behavior of ceramic matrix material the temporal evolution laws for D_c and D_p need to be defined. At this point, classical ISV methods would propose an additional scalar potential function (the potential of dissipation) to develop these evolution laws (Lemaitre J. A., 2012; Lemaitre & Desmorat, 2005). This methodology satisfies thermodynamics but is phenomenological and may not be grounded in the physics of damage evolution within the real material. To ensure that the material model is grounded in the physical damage behavior of the ceramic matrix material, a fracture mechanics methodology is used to determine the damage state variables and their temporal evolution.

3.2.2 Porosity

Accurately capturing the effects of nucleation and growth of microstructural pores is key to describing the deformation and fracture behavior of ceramics. Porosity occurs as a result of material diffusion around grain boundaries and can lead to nonlinear stress-strain constitutive behavior even at relatively low strains, (Evans, Rice, & Hirth, 1980; Bar-on, Rubin, & Yankelevsky, 2003). As shown by Rubin et al. (Rubin, Vorobiev, & Glenn, 2000), the evolution of porosity in a ceramic material is related to the material entropy dissipation rate, and a modified form of their evolution equation is used to determine the temporal evolution of D_p:

$$\dot{D_p} = a\left(1 - D_p\right)\gamma\varepsilon^V, \tag{3.7}$$

where a is a constant scaling parameter related to porosity density, γ is the entropy dissipation rate, and ε^V is the volumetric strain. $\dot{D_p}$ is a linear function of ε^V, and the slope

of $\dot{D}_p$ depends on the porosity density and the dissipation rate, γ. From Rubin et al. (Rubin, Vorobiev, & Glenn, 2000):

$$\gamma = \frac{1}{2}\left(1 - D_p\right)\Gamma_p \, |\boldsymbol{F}_{dil}| \, G \left(trace(\boldsymbol{F}_{dist}) - \frac{9}{trace(\boldsymbol{F}_{dist}^{-1})}\right), \tag{3.8}$$

where G is the shear modulus, and Γ_p is calculated as from (Rubin, Vorobiev, & Glenn, 2000) as follows:

$$\Gamma_p = \frac{3G}{\sigma_{eq}}\left(\frac{\langle \sigma_{p_{max}} - \sigma_{eq} \rangle}{\sigma_y}\right). \tag{3.9}$$

In Equation (3.9), σ_{eq} is the von Mises equivalent stress ($\sigma_{eq} = \sqrt{\frac{3}{2}\sigma_{ij}^D \sigma_{ij}^D}$ where $\sigma_{ij}^D = \sigma_{ij} - \frac{1}{3}\sigma_{kk}\delta_{ij}$ is the deviatoric stress), $\sigma_{p_{max}}$ is related to the yield stress and represents the maximum stress at which porosity nucleation is possible, and $\langle x \rangle$ are the Macaulay brackets, where $\langle x \rangle = \frac{1}{2}(x + |x|)$. Based on Flory (Flory, 1961), the deformation gradient, $\boldsymbol{F}$, can be decomposed into the product of dilatational, $\boldsymbol{F}_{dil}$, and distortional, $\boldsymbol{F}_{dist}$, parts (Flory, 1961):

$$\begin{aligned} \boldsymbol{F} &= \boldsymbol{F}_{dil} \cdot \boldsymbol{F}_{dist} \\ \boldsymbol{F}_{dil} &= \sqrt[1/3]{|\boldsymbol{F}|}\, \boldsymbol{I} \\ \boldsymbol{F}_{dist} &= \sqrt[1/3]{|\boldsymbol{F}|}\, \boldsymbol{F}, \end{aligned} \tag{3.10}$$

where a bold symbol denotes a matrix or tensor and $|\boldsymbol{A}|$ signifies the determinant of matrix $\boldsymbol{A}$.

3.2.3 Matrix Cracking

This methodology uses the self-consistent scheme as described in (Budiansky & O'Connell, 1976) to determine the change in mechanical properties due to the growth of matrix cracks from manufacturing-induced cavities. The potential energy density, ϕ, of an uncracked elastic body is:

$$\phi = \frac{1}{2}\sigma\varepsilon = \frac{1}{2}\frac{\sigma^2}{E}, \tag{3.11}$$

and the potential energy of a cracked body can be written in terms of an effective modulus, $\tilde{E}$:

$$\frac{1}{2}\frac{\sigma^2}{\tilde{E}} = \frac{1}{2}\frac{\sigma^2}{E} - N\Delta\phi. \tag{3.12}$$

The total change in potential energy density, $N\Delta\phi$, is due to the energy released by N cracks, which can be determined by integrating the J integral, which computes the strain energy released per unit fracture surface area (Cherapanov, 1967; Rice, 1968), over all crack surfaces:

$$N\Delta\phi = \frac{N(1-\nu^2)}{VE}\oint r\left[K_I^2 + K_{II}^2 + \frac{K_{III}^2}{1-\nu}\right]dS, \tag{3.13}$$

where $K_I, K_{II},$ and K_{III} depend on the crack shape and are the mode I, II, and III stress intensity factors respectively, ν is the poisson ratio, V is volume, and r is the perpendicular distance from the origin to the point of interest on the crack surface, S. If the crack shape

is known, this integral can be computed and substituted into Equation (3.12) to solve for $\tilde{E}$. Using wing cracks, which can be approximated as long elliptical cracks (Paliwal & Ramesh, An interacting micro-crack damage model for failure of brittle materials under compression, 2008), and solving for $\tilde{E}$ yields:

$$\tilde{E} = \left(1 - \frac{\pi^2}{30}(1+\nu)(5-4\nu)\Omega\right)E, \tag{3.14}$$

where Ω is the scalar volumetric crack density ($\Omega = \frac{N}{V}l^3$). The change in stiffness from Equation (3.14) can be related to the stiffness change caused by the matrix cracking damage variable in the ISV formulation so that:

$$\mathrm{D_c} = \frac{\pi^2}{30}(1+\nu)(5-4\nu)\Omega. \tag{3.15}$$

The temporal evolution of the damage variable can be determined by differentiating Equation (3.15) with respect to time:

$$\dot{D}_c = \frac{\pi^2}{10}(1+\nu)(5-4\nu)\frac{N}{V}l^2\dot{l}, \tag{3.16}$$

where l is the characteristic crack length. An expression for $\dot{l}$ can be obtained using crack growth kinetics. Following Paliwal et al. (Paliwal & Ramesh, An interacting micro-crack damage model for failure of brittle materials under compression, 2008),

$$\dot{l} = C_R \frac{K_I - K_{IC}}{K_I - K_{IC}/2}, \tag{3.17}$$

where C_R is the Rayleigh wave speed of the material and K_{IC} is the critical stress intensity factor (fracture toughness) of the material.

This model is employed at multiple length scales within the MSGMC modeling framework. The local stresses at each length scale are determined and the stress intensity factor, K_I, around the cavity is evaluated using the maximum principal stress and compared to the critical stress intensity factor, K_{IC}. When $K_I = K_{IC}$ the cavity is activated and a crack begins to grow. Due to the brittle nature of the ceramic matrix material, the mode II and III stress intensity factors play a negligible role in the rate of crack growth (Wachtman, Cannon, & Matthewson, 2009) and are not included in the model. It is also important to emphasize that the cracking damage variable captures the effects of matrix crack growth from existing defects (manufacturing induced cavities) and does not account for nucleation of additional defects, which is why N/V in Equation (3.16) does not vary with time. The nucleation of new micro-defects is accounted for by the porosity internal state variable described in the previous section.

3.2.4 Crack-induced Local Anisotropy

The equations outlined above assume that D_c, the matrix cracking ISV, behaves isotropically; in reality, matrix cracking causes local anisotropy. To better approximate the physical fracture behavior of the brittle CMC matrix material, the cracked matrix is assumed to be transversely isotropic in the plane of the crack, and matrix anisotropy occurs

when the damaged stiffness tensor is rotated from the crack plane to global axes. The relationships outlined in Equations (3.13) - (3.16) are applied to obtain the effective modulus perpendicular to the crack face, $\widetilde{E_n}$, which is equivalent to the effective (damaged) modulus obtained from the isotropic matrix damage relationships. The matrix cracking ISV in Equation (3.15) and its temporal evolution relationship in Equation (3.16) are applied to obtain a transversely isotropic damaged compliance tensor ($\tilde{\boldsymbol{S}}$) in the plane of the crack. In matrix form:

$$\tilde{\mathbf{S}} = \begin{bmatrix} 1/E_t & -\nu/E_t & -\nu/E_n & 0 & 0 & 0 \\ -\nu/E_t & 1/E_t & -\nu/E_n & 0 & 0 & 0 \\ -\nu/E_n & -\nu/E_n & 1/E_n & 0 & 0 & 0 \\ 0 & 0 & 0 & 1/G_{tn} & 0 & 0 \\ 0 & 0 & 0 & 0 & 1/G_{tn} & 0 \\ 0 & 0 & 0 & 0 & 0 & 2(1+\nu)/E_t \end{bmatrix}, \tag{3.18}$$

where E_t is the transverse modulus ($E_t = E$), and G_{tn} is the cracked shear modulus, which is assumed to follow the form $G_{tn} = \frac{E_n}{2(1+\nu)}$. The Poisson's ratio in a cracked body is expected to slightly increase (Wang & Ramesh, 2003), but some researchers have observed no significant change (Paliwal, Ramesh, & MaCauley, Direct observation of the dynamic compressive failure of a trnasparent polycrystalline ceramic, 2006) or even a decrease in poisson ratio (Budiansky & O'Connell, 1976) after onset of cracking in a brittle material. Due to a lack of experimental data for this material system and the conflicting results in the literature, the Poisson's ratio is kept constant in this model. The compliance in global axes are obtained by rotating the damaged compliance tensor from principal axes to global axes as follows (in Einstein notation):

$$S'_{ijkl} = R_{ip}R_{jq}\tilde{S}_{pqrs}R_{kr}R_{ls}, \tag{3.19}$$

where $\boldsymbol{R}$ is the rotation matrix whose rows are the unit vectors associated with the principal stresses and are the basis vectors for the principal frame, and the indices $i, j \ldots r, s$ range from 1 to 3. As a result of the rotation from principal axes, the resulting compliance tensor, $\tilde{\boldsymbol{S}}'$, and the corresponding stiffness tensor, $\tilde{\boldsymbol{C}}'$, are fully anisotropic in the global frame where loads are applied.

3.3 Multiscale Modeling Framework

The complex multiscale behavior of CMCs is in large part due to the material architecture and necessitates the use of multiscale modeling methods to accurately model the relevant damage physics at each length scale. Multiscale modeling methods can link material constitutive behavior and capture damage initiation and evolution behavior at each relevant length scale. Therefore, the fracture mechanics-informed damage model is implemented in the MSGMC framework (Liu, Chattopadhyay, Bednarcyk, & Arnold, 2011) to predict the behavior of various C/SiC CMC architectures. The MSGMC method is a recursive application of the GMC (Aboudi, Arnold, & Bednarcyk, 2012), and allows concurrent analysis of an arbitrary number of length scales.

Idealized representations of common 2D weaves used in CMCs, including plain weave, 5HS, and 8HS, are shown in Figure 3.1. In each case, the idealized weave can be divided into a series of repeating units, which are defined as representative unit cells (RUCs). Since the RUC is representative of the weave, the overall weave behavior can be obtained by simulating the behavior of the RUC. Figure 3.2 illustrates how the plain weave architecture

can represented using the MSGMC. Figure 3.2(a) shows a section of the plain weave architecture, which can be divided into four identical repeating units, which are the weave-level RUCs for this architecture. The weave level RUC is triply periodic and can be discretized into $N_\alpha x N_\beta x N_\gamma$ subcells, where α, β, and γ correspond to the 1, 2, and 3 directions, respectively. In this case, $\alpha = \beta = \gamma = 4$, as shown in Figure 3.2(b). The material properties and orientations of each subcell are selected to best represent the overall material architecture including intertow matrix subcells and aligned and undulating tows. The bold dotted line in Figure 3.2(b) indicates the weft tow undulation.

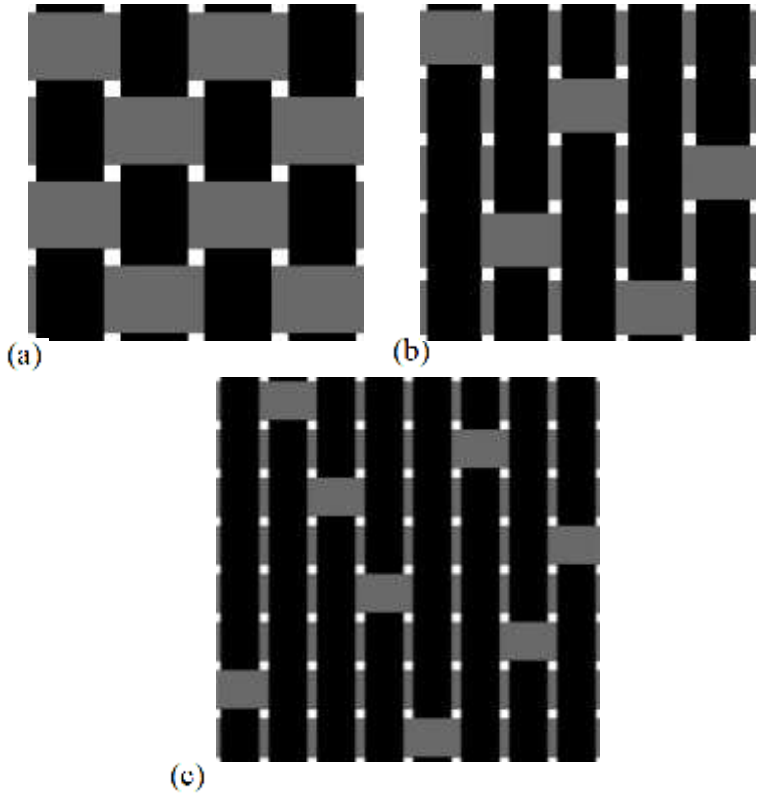

Figure 3.1. Common CMC 2D Woven Architectures; (a) Plain Weave; (b) 5HS Weave; (c) 8HS Weave

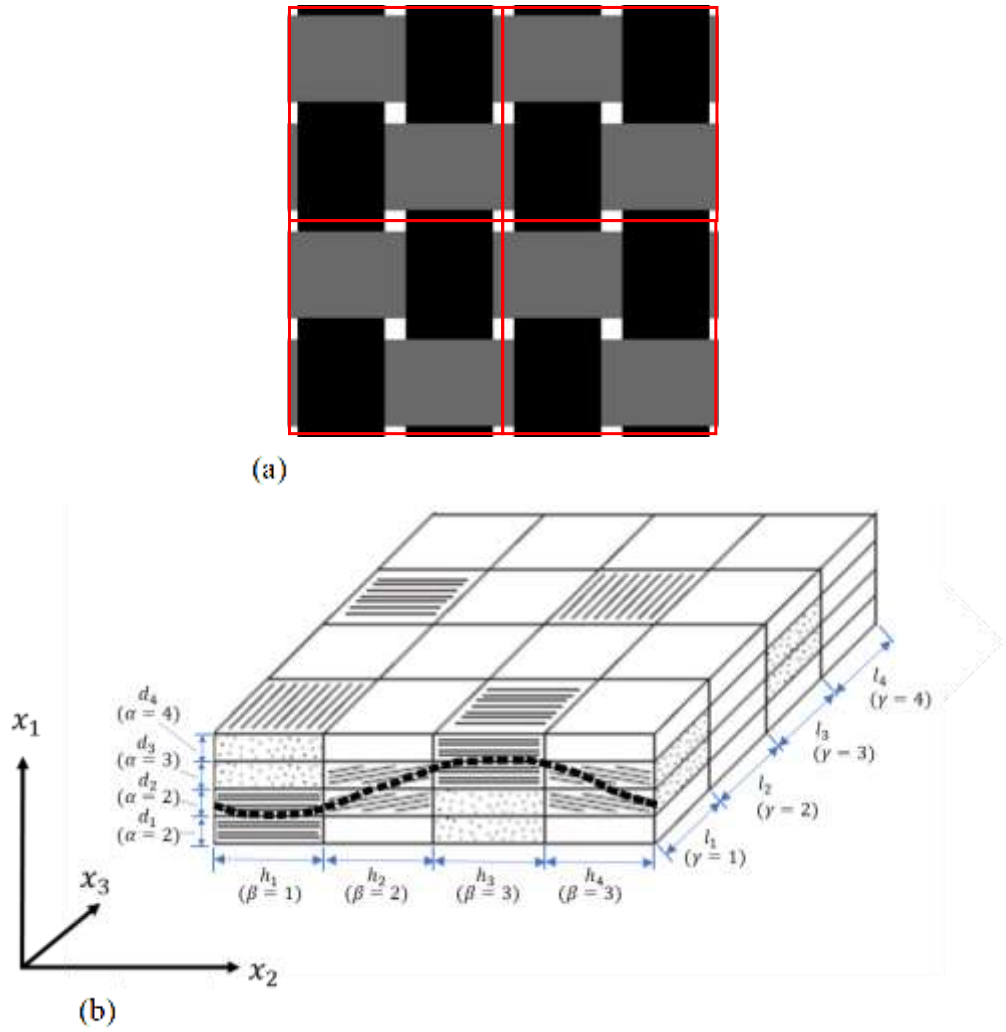

Figure 3.2. MSGMC Representation of 2D Plain Weave Architecture; (a) Section of Plain Weave Architecture with Four Weave-level RUCs; (b) Weave-level RUC Discretized into Subcells—Adapted from (Aboudi, Arnold, & Bednarcyk, 2012)

In order to capture the effects of microstructure and microscale damage, the weave-level RUC can be further discretized as shown in Figure 3.3. Figure 3.3(a) shows the exploded view of the weave-level RUC and the undulating warp tows are indicated with bold dashed lines. The weave-level RUC consists of six unique subcell stacks that comprise the material mesoscale. Each subcell stack consists of subcells assigned properties and

orientations corresponding to intertow matrix, undulating warp and weft tows, and aligned warp and weft tows (see Figure 3.3(b)). Each subcell of the weave-level RUC makes up a tow-level RUC which consists of microscale subcells made up of monolithic intertow matrix, fiber, fiber coating/interphase, or intratow matrix material.

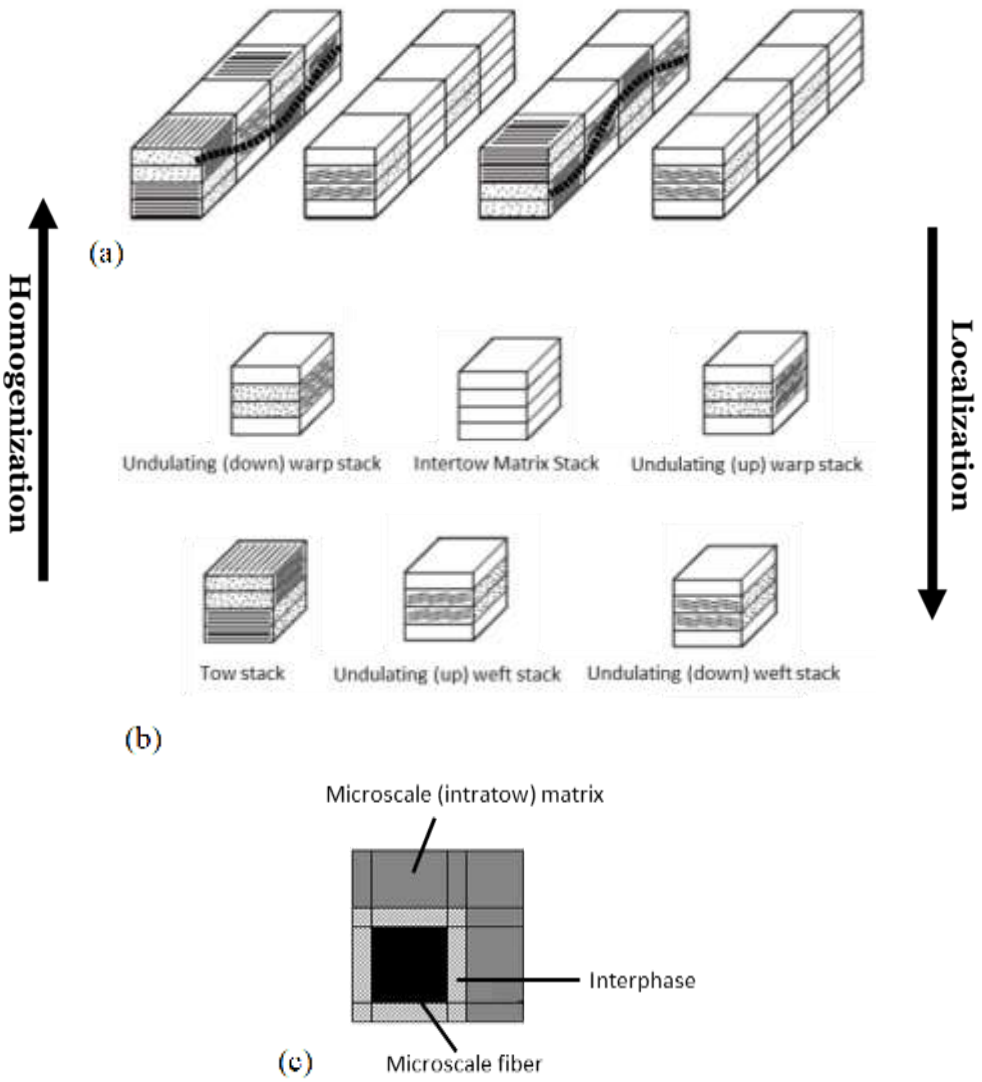

Figure 3.3. Multiscale Representation of 2D Plain Weave Architecture using MSGMC; (a) Exploded View of Weave-level RUC Discretized into Subcells—Adapted from

(Aboudi, Arnold, & Bednarcyk, 2012); (b) Mesoscale Subcell Stacks; (c) Microscale RUC Consisting of Monolithic Fiber, Matrix, and Interphase Material Subcells

By linking the length scales and moving down length scales (localization) and up length scales (homogenization), the damage behavior of the CMC can be concurrently analyzed at each relevant length scale. The simulated global strain, $\bar{\boldsymbol{\varepsilon}}$, is applied at the macroscale level to the weave RUC (see Figure 3.2), and the subcell strains are obtained using the following localization algorithm:

$$\boldsymbol{\varepsilon}^{\{\alpha\beta\gamma\}} = \boldsymbol{A}^{\{\alpha\beta\gamma\}}\bar{\boldsymbol{\varepsilon}} + \boldsymbol{D}^{\{\alpha\beta\gamma\}}\left(\boldsymbol{\varepsilon}^{\{\alpha\beta\gamma\}\boldsymbol{I}} + \boldsymbol{\varepsilon}^{\{\alpha\beta\gamma\}\boldsymbol{T}}\right), \tag{3.20}$$

where $\{\alpha\beta\gamma\}$ denotes the subcell location within the weave-level RUC, $\boldsymbol{A}^{\{\alpha\beta\gamma\}}$and $\boldsymbol{D}^{\{\alpha\beta\gamma\}}$ are $6N_\alpha xN_\beta xN_\gamma$ square concentration matrices which are functions of subcell geometry and stiffness, and $\boldsymbol{\varepsilon}^{\{\alpha\beta\gamma\}\boldsymbol{I}}$ and $\boldsymbol{\varepsilon}^{\{\alpha\beta\gamma\}\boldsymbol{T}}$ are the subcell inelastic and thermal strains, respectively (Aboudi, Arnold, & Bednarcyk, 2012; Liu, Chattopadhyay, Bednarcyk, & Arnold, 2011). Each subcell of the macroscale RUC is then modeled using a doubly periodic mesoscale RUC which is in turn discretized into $N_{\{\alpha\beta\gamma\}\beta}xN_{\{\alpha\beta\gamma\}\gamma}$ subcells (see Figure 3.3(b)). Additional localization is performed to obtain the mesoscale RUC subcell strains:

$$\boldsymbol{\varepsilon}^{\{\alpha\beta\gamma\}\{\beta\gamma\}} = \boldsymbol{A}^{\{\alpha\beta\gamma\}\{\beta\gamma\}}\boldsymbol{\varepsilon}^{\{\alpha\beta\gamma\}} + \boldsymbol{D}^{\{\alpha\beta\gamma\}\{\beta\gamma\}}\left(\boldsymbol{\varepsilon}^{\{\alpha\beta\gamma\}\{\beta\gamma\}\boldsymbol{I}} + \boldsymbol{\varepsilon}^{\{\alpha\beta\gamma\}\{\beta\gamma\}\boldsymbol{T}}\right). \tag{3.21}$$

The subcells of the mesoscale RUC are modeled using a microscale RUC consisting of mesoscale matrix or fiber (monofilament), fiber coating (interphase), and microscale matrix subcells (see Figure 3.3(c)). A final localization is performed to determine the strain

of each constituent subcell and constitutive relationships are applied to obtain the stress-strain response of each constituent subcell. The fiber and damage models are applied at this step to determine the damaged response of the corresponding subcells. The subcell stresses are then volume averaged (homogenized) to obtain the stress of the RUC at that length scale.

The stresses at each length scale are determined using homogenization techniques. The homogenized microscale RUC stress (mesoscale RUC subcell stress) is obtained using the microscale RUC effective stiffness, $\boldsymbol{C}^{\{\alpha\beta\gamma\}\{\beta\gamma\}\star}$, which depends on the microscale geometry and constituent material properties:

$$\boldsymbol{\sigma}^{\{\alpha\beta\gamma\}\{\beta\gamma\}} = \boldsymbol{C}^{\{\alpha\beta\gamma\}\{\beta\gamma\}\star}\left(\boldsymbol{\varepsilon}^{\{\alpha\beta\gamma\}\{\beta\gamma\}} - \boldsymbol{\varepsilon}^{\{\alpha\beta\gamma\}\{\beta\gamma\}\boldsymbol{I}} - \boldsymbol{\varepsilon}^{\{\alpha\beta\gamma\}\{\beta\gamma\}\boldsymbol{T}}\right). \tag{3.22}$$

Similarly, the homogenized mesoscale RUC stress (macroscale RUC subcell stress) is determined using:

$$\boldsymbol{\sigma}^{\{\alpha\beta\gamma\}} = \boldsymbol{C}^{\{\alpha\beta\gamma\}\star}\left(\boldsymbol{\varepsilon}^{\{\alpha\beta\gamma\}} - \boldsymbol{\varepsilon}^{\{\alpha\beta\gamma\}\boldsymbol{I}} - \boldsymbol{\varepsilon}^{\{\alpha\beta\gamma\}\boldsymbol{T}}\right). \tag{3.23}$$

Finally, the global macroscale RUC stress, $\overline{\boldsymbol{\sigma}}$, is obtained using the homogenized composite stiffness matrix, $\boldsymbol{C}^{\star}$:

$$\overline{\boldsymbol{\sigma}} = \boldsymbol{C}^{\star}(\overline{\boldsymbol{\varepsilon}} - \overline{\boldsymbol{\varepsilon}}^{\boldsymbol{I}} - \overline{\boldsymbol{\varepsilon}}^{\boldsymbol{T}}). \tag{3.24}$$

These localization/homogenization algorithms allow for an accurate semi-analytical solution that can include the effects of damage at each length scale.

The CMCs simulated in this chapter are UD and 2D 5HS woven architecture. The MSGMC methodology for the 5HS weave used in this chapter is shown in Figure 3.4. The mesoscale repeating unit cell (RUC) of the UD composite consists of microscale fiber and matrix subcells arrayed as shown in the tow level RUC in Figure 3.4. A tow fiber volume fraction of 0.56 was used for the simulations. The 5HS weave RUC consists of macroscale matrix and macroscale fiber tow subcell stacks to accurately represent weave architecture. The tow subcells in the stacks are modeled as unidirectional tows using the UD mesoscale RUC which consists of microscale matrix and microscale monofilament fiber subcells. The weave fiber volume fraction used in the simulation was 0.43. The damage model is applied to each macroscale, mesoscale, and microscale matrix subcell independently, allowing the model to capture multiscale matrix damage behavior.

The fibers are modeled as a linearly elastic transversely isotropic material. The focus of this chapter is the initiation and propagation of damage in the CMC matrix material, hence the use of a simple fiber model. A CVI boron nitride (BN) fiber coating/interphase material is included in the MSGMC model. Damage and failure in the coating is not considered since the BN is already less than 5% as stiff as the matrix material, so modeling degradation in the BN stiffness would have negligible effect on the overall composite performance. Accurately modeling the distribution of manufacturing induced cavities is key to capturing the mechanical behavior of CVI CMCs. As shown in Figure 3.5, CVI CMCs have localized regions of high void content. The distribution of manufacturing induced cavities will have significant effects on CMC mechanical response and must be modeled. A realistic cavity distribution with localized concentrations of cavities was

accounted for in the MSGMC framework as discussed in (Liu, Chattopadhyay, & Arnold, Impact of material and architecture model parameters on the failure of woven CMCs via the multiscale generalized method of cells, 2011).

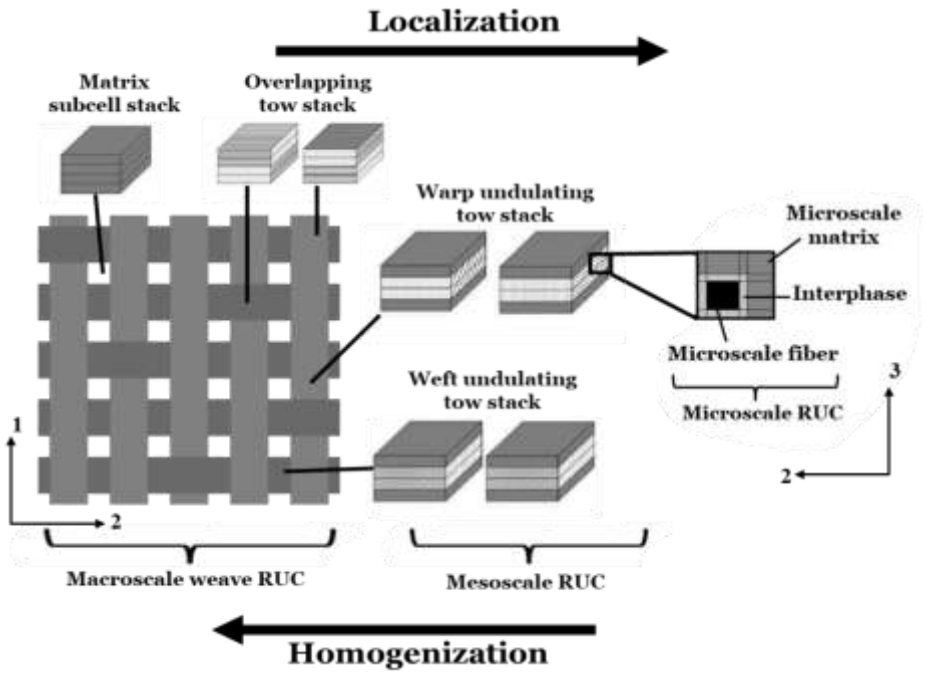

Figure 3.4. Schematic of MSGMC Multiscale Modeling Methodology for 5HS Weave

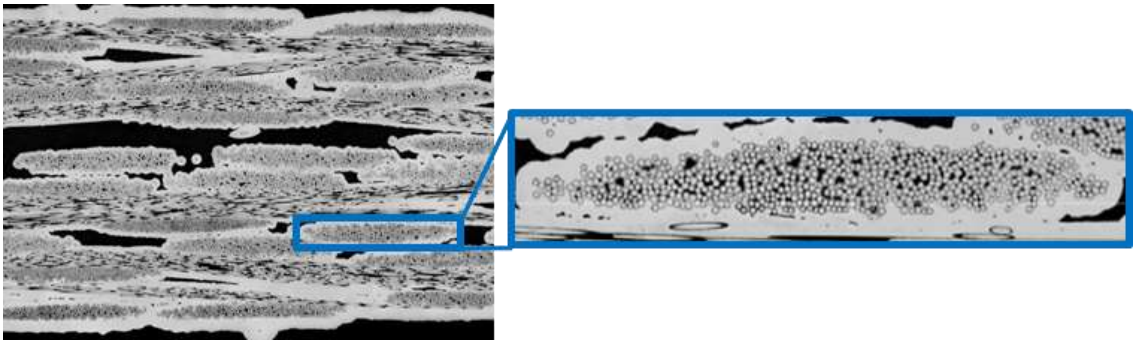

Figure 3.5. Micrograph of CVI CMC Showing Weave and Tow Level Manufacturing Induced Cavities; Adapted from Bonacuse et al. (Bonacuse, Mital, & Goldberg, 2011)

3.4 Results and Discussion

3.4.1 Monolithic SiC Response

To demonstrate the capabilities of the damage model, the stress-strain response of bulk SiC matrix material is simulated and compared to the linear elastic case. The effects of crack anisotropy on the simulation results are considered and the results are compared to those obtained using an isotropic matrix cracking damage variable. Additionally, the results obtained by considering only the matrix cracking (anisotropic) are compared to the results obtained simulating both anisotropic matrix cracking and porosity. The relevant material properties and initial values for crack density and characteristic crack length used to compare the anisotropic matrix cracking damage variable to the isotropic case are included in Table 3.1.

Table 3.1. Material Properties and Model Parameters Used to Simulate Monolithic SiC With Isotropic Damage ISV and Anisotropic Damage ISV

K_{IC} $(MPa\sqrt{m})$	E (GPa)	ν	Ω_0	l_0
4.9	415	.17	0.001	0.005

The model captures the quasi brittle behavior of the bulk SiC matrix as shown in the simulated stress-strain curves in Figure 3.6. In both the isotropic and anisotropic damage cases, stress increases linearly with strain until the stress intensity factor exceeds the fracture toughness and cracking is activated. The crack grows rapidly, causing material

property degradation until a critical crack length is reached and failure occurs. The maximum stress increases when the cracked matrix is modeled as an anisotropic material and occurs at a slightly higher value of strain compared to the isotropic damage case. Additionally, as shown in Figure 3.7 (b), the effective stiffness of the bulk matrix material is higher when anisotropy due to damage is considered. This is as expected, since cracking initiates and propagates in the principal plane, which is aligned at an angle relative to the global (loading) axes. When crack direction and transverse isotropy are accounted for, the maximum stiffness degradation occurs normal to the crack surface, and no degradation occurs transverse to the crack. It is interesting to note that the stiffness of the anisotropic damaged matrix is higher than that of the isotropic case even though damage initiates earlier and evolves more rapidly in the anisotropic case than the isotropic case. This is because as the damaged stiffness tensor in the plane of the crack is rotated from principal axes to global axes, the reduction in stiffness for each direction will be less than that observed normal to the crack face, and a significantly longer crack is required to release energy and have a similar effect on global stiffness. The damage variable computed in the principal plane in the isotropic case releases additional energy and degrades the entire stiffness tensor equally without considering the effects of crack orientation or transverse isotropy.

The damage parameter and effective damaged stiffness of the bulk SiC material for both isotropic and anisotropic damage cases are shown in Figure 3.7. After crack activation, the crack length increases rapidly, causing a rapid increase in the damage ISV

until material failure occurs when $D \approx 0.9$ for the isotropic damage case, and when $D \approx 1$ for the anisotropic case.

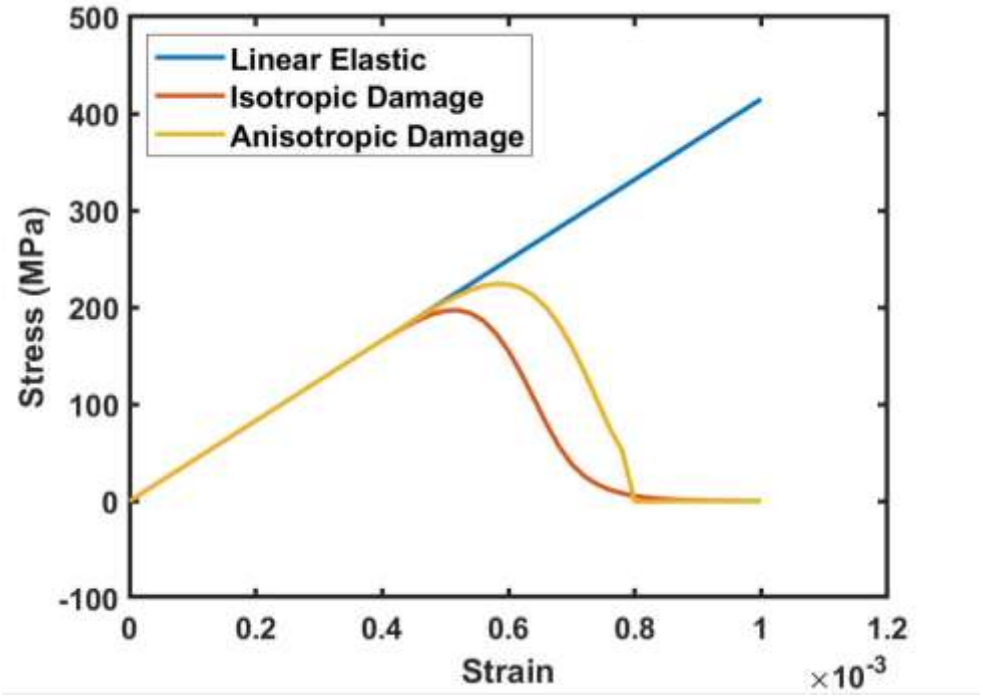

Figure 3.6. Simulated Stress-strain Response of Monolithic SiC with Isotropic and Anisotropic Matrix Cracking ISVs

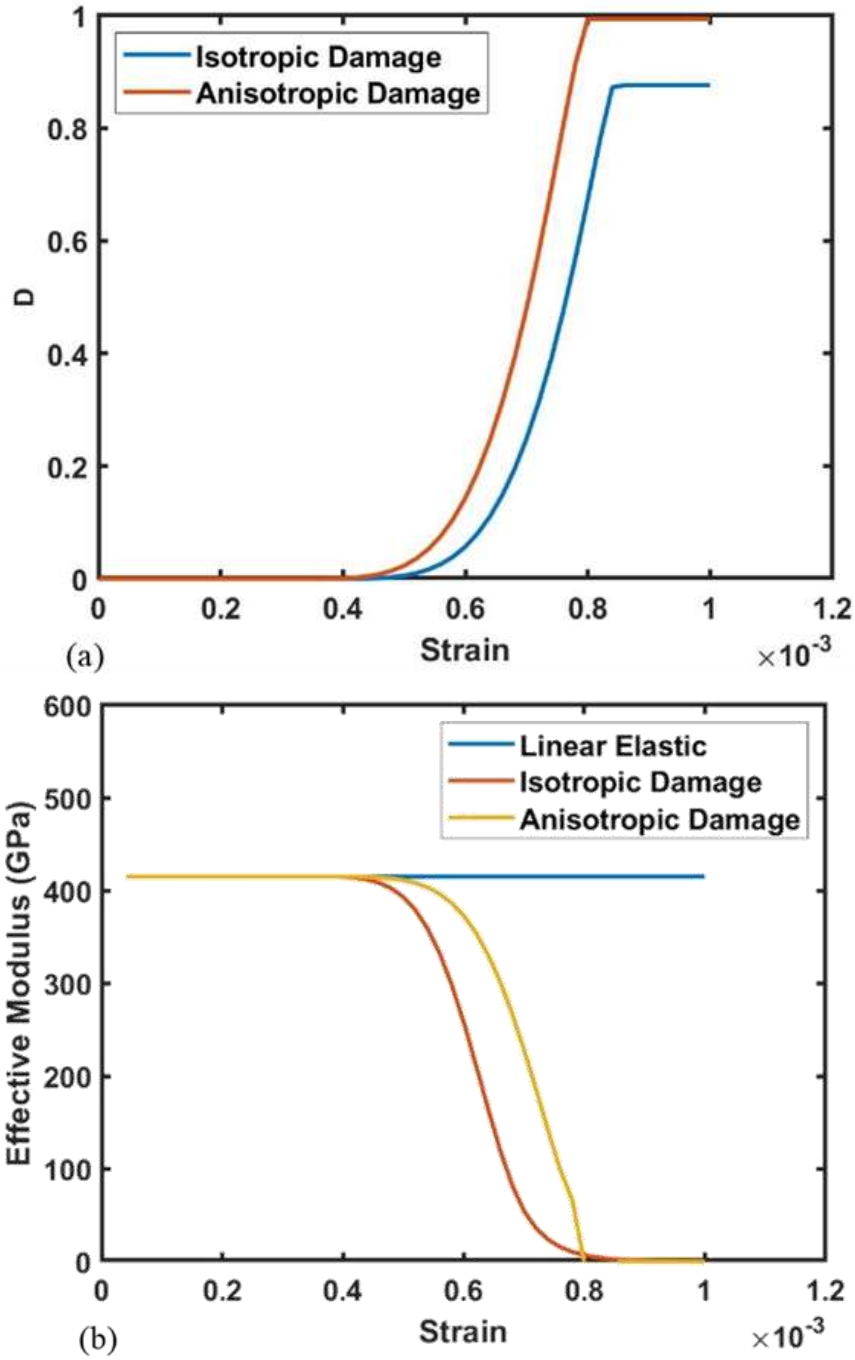

Figure 3.7. Monolithic SiC Damage and Effective Modulus Evolution. (a) Isotropic and Anisotropic Damage Parameters vs. Strain; (b) Effective SiC Modulus vs. Strain

As discussed in a previous section, the nucleation and propagation of micropores is an important low strain damage mechanism in many brittle ceramic materials. The effects of porosity have also been considered and the results are included below. The relevant material properties and model parameters, including initial values for pore density, crack density, and characteristic crack length are presented in Table 3.2.

Table 3.2. Material Properties and Model Parameters Used to Simulate Monolithic SiC With Matrix Cracking and Porosity Effects

K_{IC} ($MPa\sqrt{m}$)	E (GPa)	ν	D_{p0}	A	N/V (m^{-1})	l_0	σ_y (MPA)
4.9	415	0.17	0.01	5000	2300	0.005	160

The results of simulating the quasi brittle behavior of the SiC matrix material using porosity effects are shown in Figure 3.8. When only matrix microcracking is considered, stress increases linearly with strain until the stress intensity factor near manufacturing induced cavities exceeds the fracture toughness and cracking is activated. The crack grows rapidly and causes material property degradation until a critical crack length is reached and failure occurs. When porosity effects are included in addition to matrix microcracking, material nonlinearity occurs even before crack activation as a result of pore nucleation and growth caused by material diffusion around SiC grain boundaries. The peak stress decreases slightly when porosity effects are considered and occurs at higher strain as a result of additional deformation caused by pore growth.

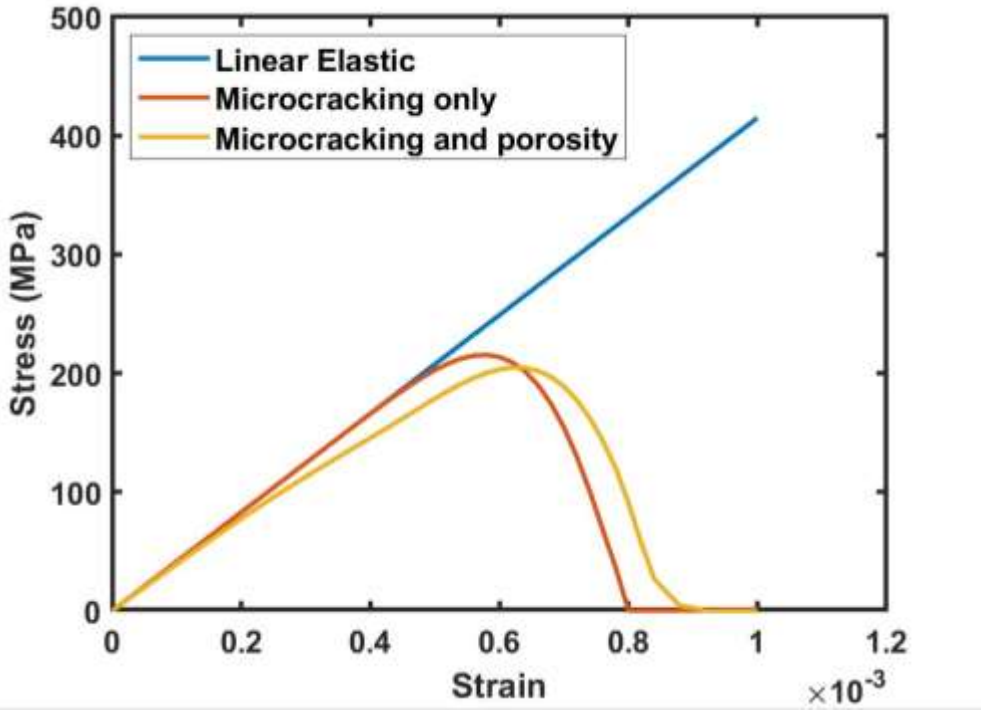

Figure 3.8. Simulated Stress–strain Response of Monolithic SiC with Microcracking and Porosity

Data relating to characteristic crack length, damage due to matrix microcracking, and damage due to pore nucleation and growth obtained from the damage model are shown in Figure 3.9. The initial material nonlinearity before matrix microcrack activation (see Figure 3.9d) is due to the evolution of the porosity ISV (D_p), which increases sigmoidally before reaching saturation when $D_p \approx 0.13$. After crack activation, the characteristic crack length increases rapidly before reaching a critical value. The microcracking damage ISV (D_c) follows a similar trend and total material failure occurs when $D_c \approx 0.9$. To satisfy the dissipation inequality given in Equation (3.1), the temporal evolution of the damage ISVs must monotonically increase. Figure 3.9 (b-c) show that the fracture mechanics definition

of D_c and the dissipation-based definition of D_p and their growth rates are thermodynamically valid and agree with ISV theory.

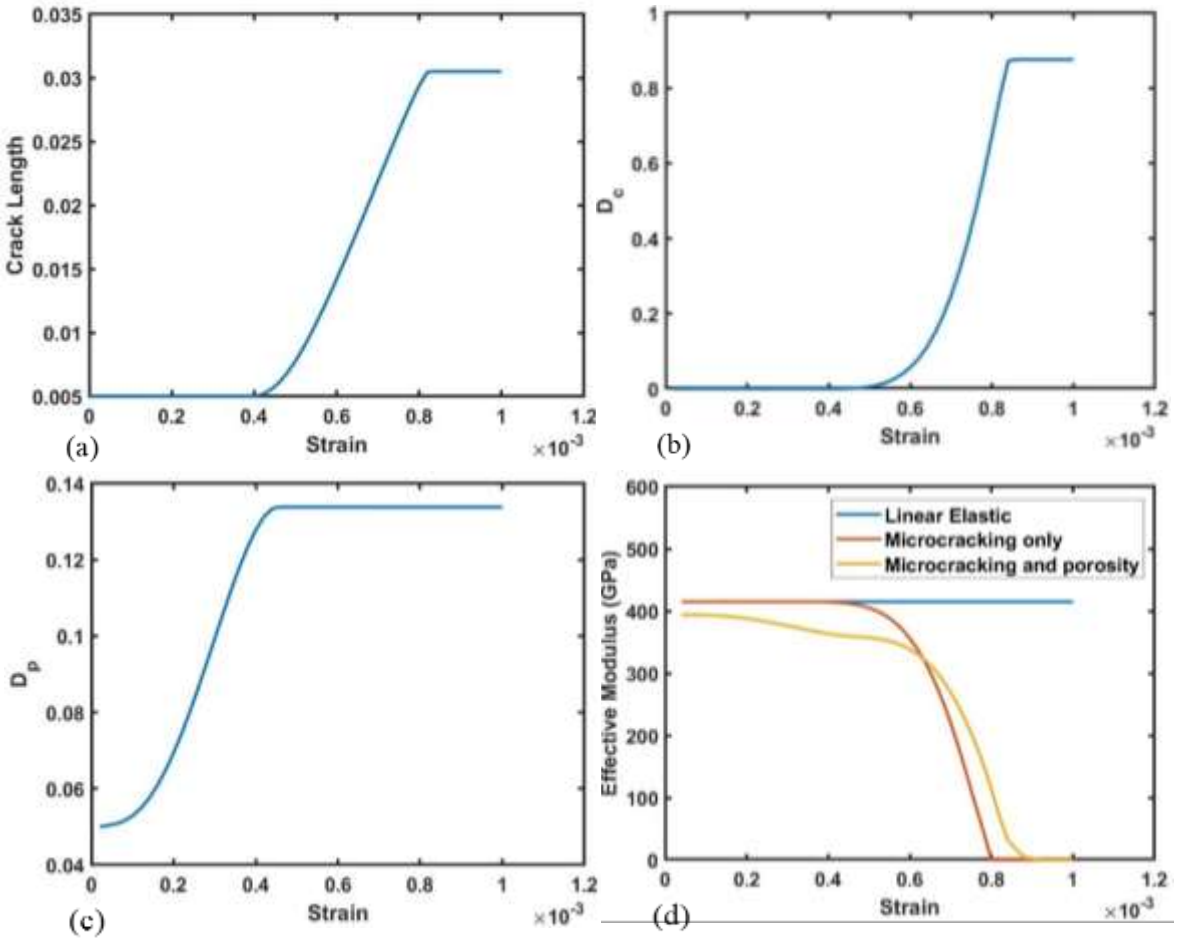

Figure 3.9. Evolution of Damage Model Parameters and Effective Modulus in Monolithic SiC. (a) Normalized Microcrack Length vs. Strain; (b) Damage from Microcracking vs. Strain; (c) Damage from Nucleation and Growth of Pores vs. Strain; (d) Effective SiC Modulus vs. Strain

3.4.2 Unidirectional Composite Response

The response of a UD C/SiC CMC was also simulated using the fracture mechanics-informed matrix cracking damage model. Simulation results are presented for a T300

carbon fiber and the damage model is applied to the SiC matrix material. The properties for the T300 fiber used in the model are presented in Table 3.3. Figure 3.10 shows the simulated stress-strain response of the UD C/SiC and compares the isotropic damage case with the anisotropic damage case. As in the monolithic SiC simulations shown above, the anisotropic damage case shows a slightly stiffer response with slower damage growth compared to the isotropic damage case. The effective stiffnesses obtained from the simulations using isotropic and anisotropic damage variables are shown in Figure 3.11.

Table 3.3. Material Properties for T300 Fibers (Daniel & Ishai, 2006)

Axial Modulus	230 GPA
Transverse Modulus	15 GPa
Axial Shear Modulus	27 GPa
Transverse Shear Modulus	7 GPa
Poisson's Ratio, $\boldsymbol{\nu_{12}}$	.23

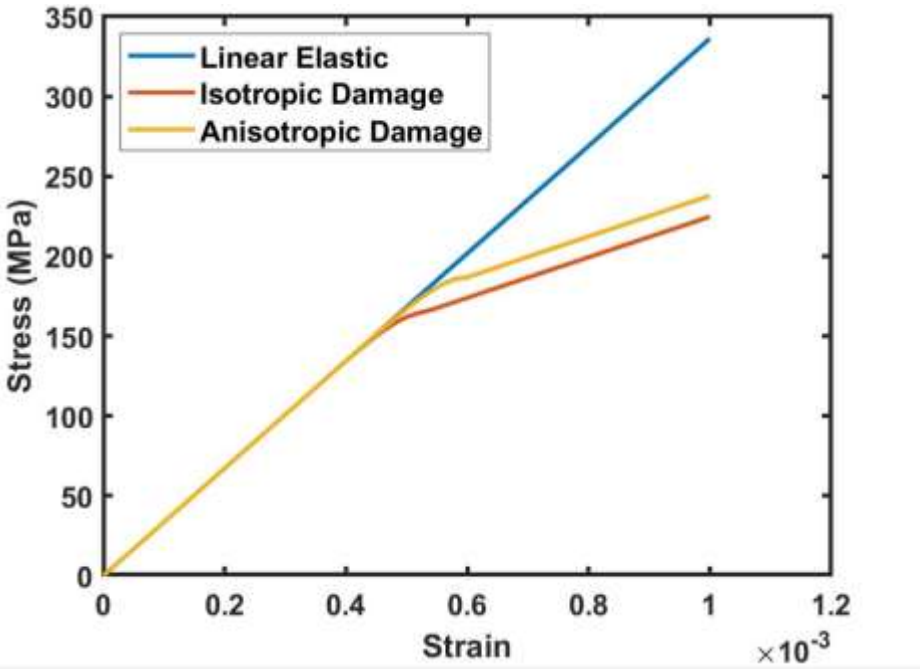

Figure 3.10. Simulated Stress–strain Response of UD C/SiC with Isotropic and Anisotropic Matrix Cracking ISVs

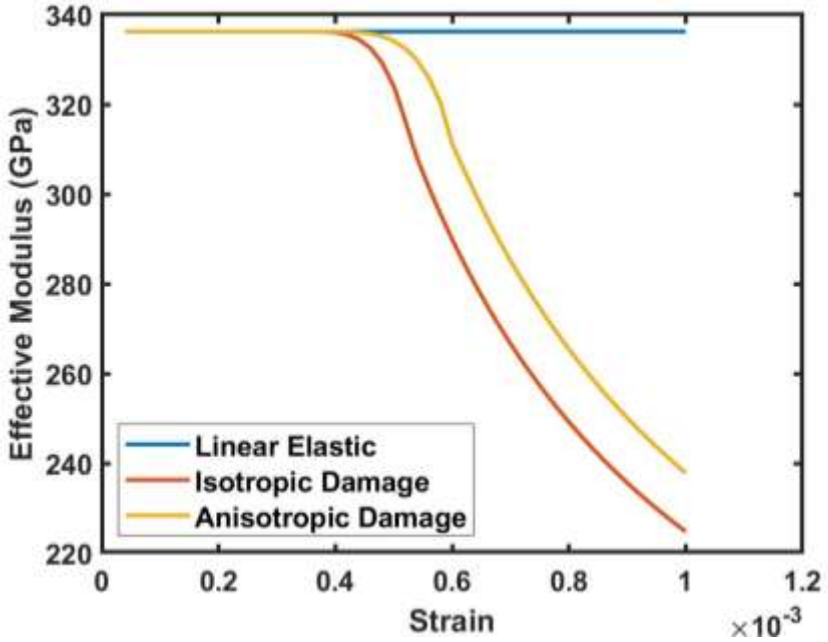

Figure 3.11. Simulated Effective Modulus Response of UD C/SiC with Isotropic and Anisotropic Matrix Cracking ISVs

Figure 3.12 compares the simulated stress-strain response of a UD C/SiC composite obtained using only anisotropic matrix cracking to those obtained using both microcracking and porosity. Matrix microcracking initiates in the matrix-rich intertow regions as cracks activate near areas with high void concentrations which cause increased stress intensity factors. Similarly, significant porosity nucleation and growth occurs in this region, causing material nonlinearity at low strains. As strain increases, matrix cracks extend and further degrade the composite properties before reaching saturation at approximately 0.2% strain when only considering matrix microcracking. In addition to causing early material nonlinearity, the porosity effects accelerate damage growth in the composite, and damage saturation occurs at lower strain than the matrix microcracking only case, occurring at approximately .15% strain when porosity effects are included (see Figure 3.13).

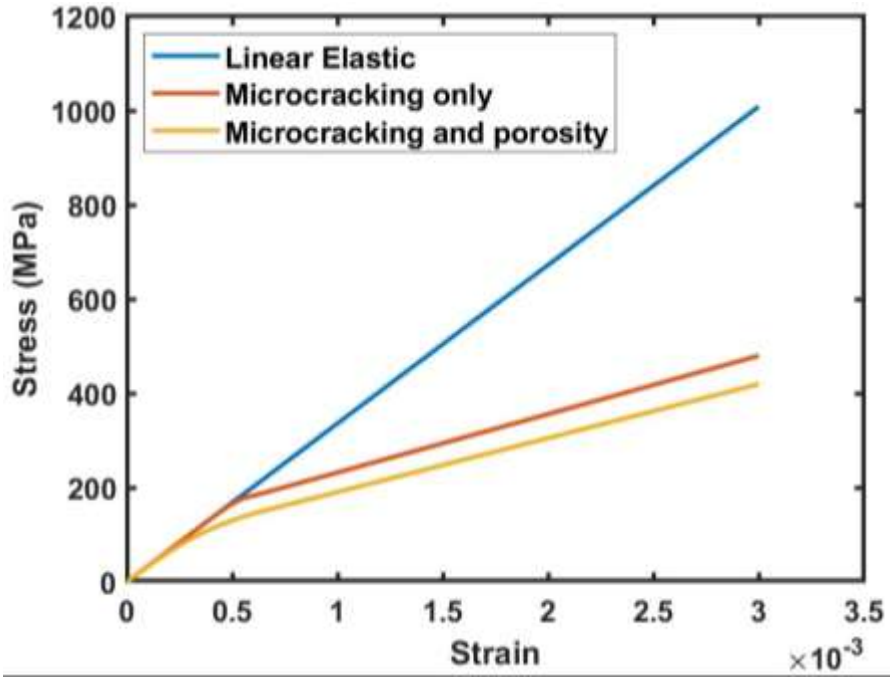

Figure 3.12. Simulated Response of UD C/SiC with Microcracking and Porosity

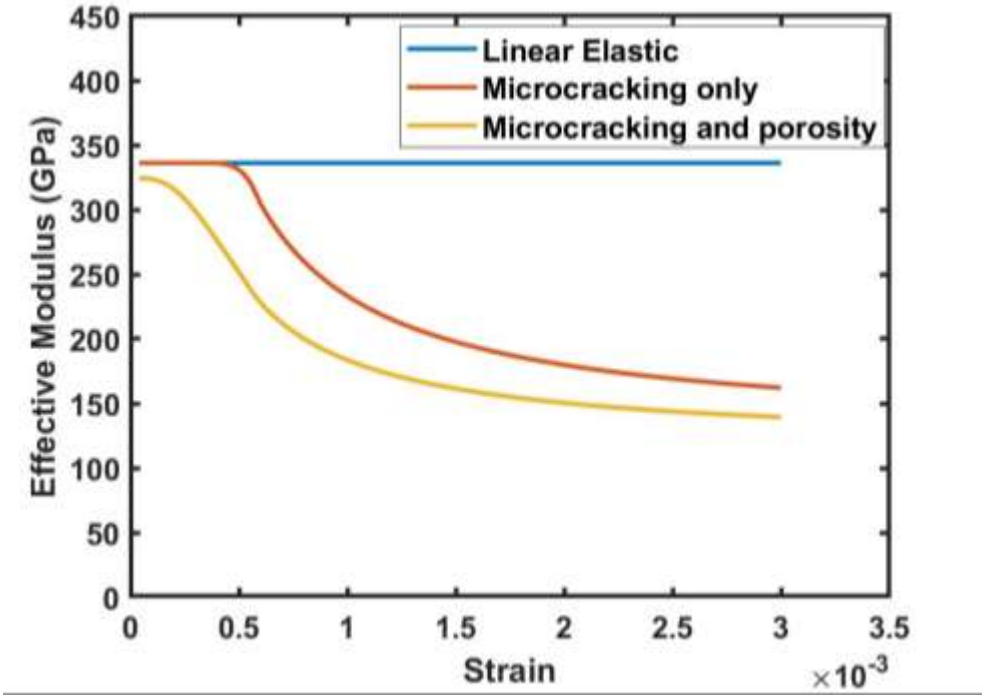

Figure 3.13. Effective Modulus of UD C/SiC with Microcracking and Porosity Effects

3.4.3 Woven Composite Response

The stress-strain simulation results for a 5HS woven C/SiC CMC simulated using isotropic and anisotropic matrix cracking ISVs are shown in Figure 3.14, and effects of damage using isotropic and anisotropic damage are compared. The simulation results show trends that match those seen in literature. The fracture mechanics-informed matrix microcracking damage model effectively captures first matrix cracking, which results in deviation from linear elastic material behavior. The anisotropic damage case predicts first matrix cracking at slightly higher stress than the isotropic damage case and remains slightly stiffer after first matrix cracking due to the stiffer behavior of the damaged matrix when cracks are modeled as transversely isotropic. The effective woven composite modulus obtained using isotropic and anisotropic damage ISVs is presented in Figure 3.15 and key

matrix damage mechanisms are indicated, illustrating the model's ability to capture the multiscale physics of matrix damage in woven CMCs. The woven composite has undulating tows, which cause local stress concentrations that accelerate crack activation and significantly decrease effective modulus. Damage initiates in the undulating tows, and the local tow-level damage contributes to the overall composite degradation. As strain increases, cracks initiate and propagate in the matrix rich interweave regions between tows and the overall composite modulus is further degraded.

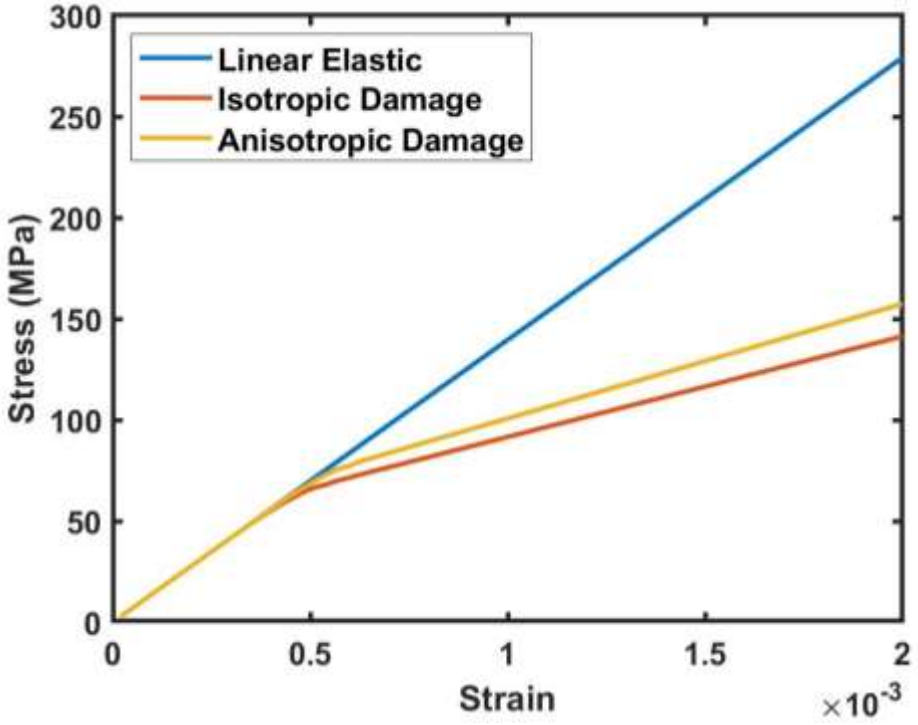

Figure 3.14. Simulated Response of 2D Woven C/SiC CMC with Isotropic and Anisotropic Damage

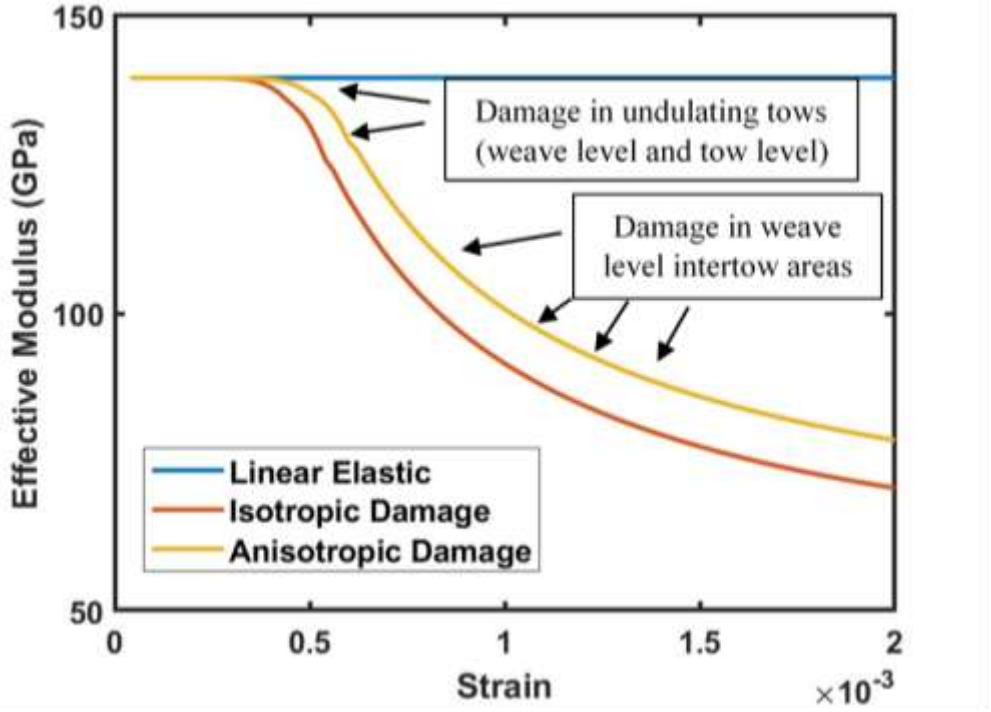

Figure 3.15. Simulated Effective Modulus Response of 2D Woven C/SiC CMC with Isotropic and Anisotropic Damage

Figure 3.16 shows the stress-strain simulation results for a 2D woven C/SiC CMC obtained using matrix cracking only (anisotropic) as well as matrix cracking and porosity, and effects of microcracking and porosity are compared to the linear elastic case. An example of a simulated 5HS weave RUC is shown in Figure 3.17(a), with the matrix material represented in red, the warp and weft overlapping tow stacks represented with light blue, and the undulating tows represented with dark blue (sandwiched between red matrix cells). These undulating tows cause local stress concentrations that accelerate microcrack activation and pore nucleation and lead to a significantly lower predicted effective modulus than that of the UD composite. Figure 3.17 (b) shows the damaged weave RUC at .25% strain and illustrates the model's ability to capture the multiscale

physics of matrix damage in woven CMCs. Damage initiates in the undulating tows and local tow-level damage contributes to the overall composite degradation. As strain increases, tow level damage growth is arrested as cracks initiate and propagate in the matrix rich interweave regions between tows and the overall composite modulus is further degraded.

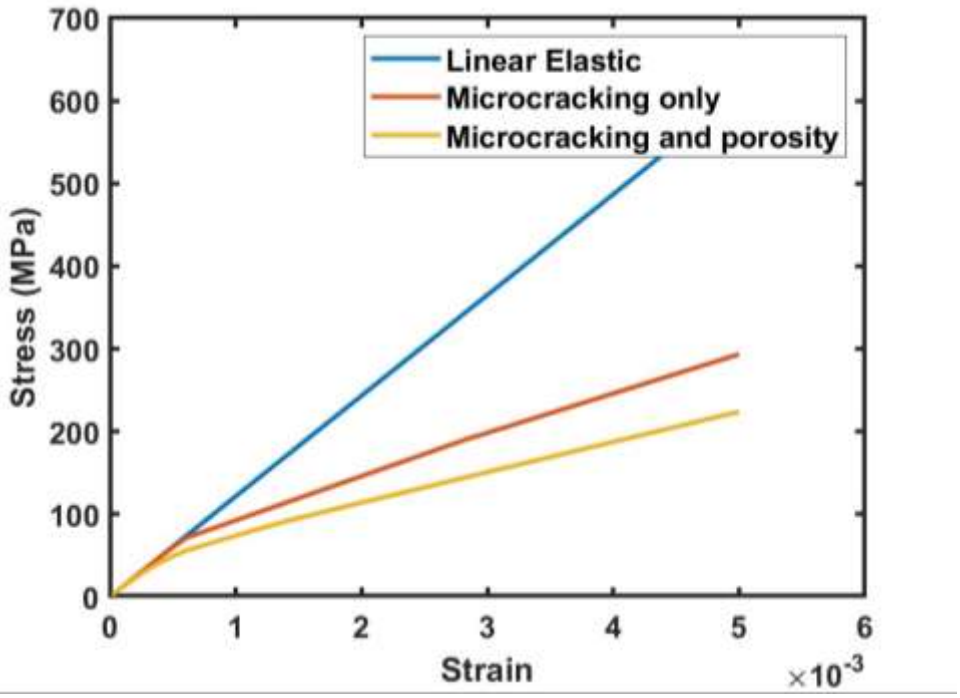

Figure 3.16. Simulated Response of 2D Woven C/SiC CMC with Matrix Cracking and Porosity

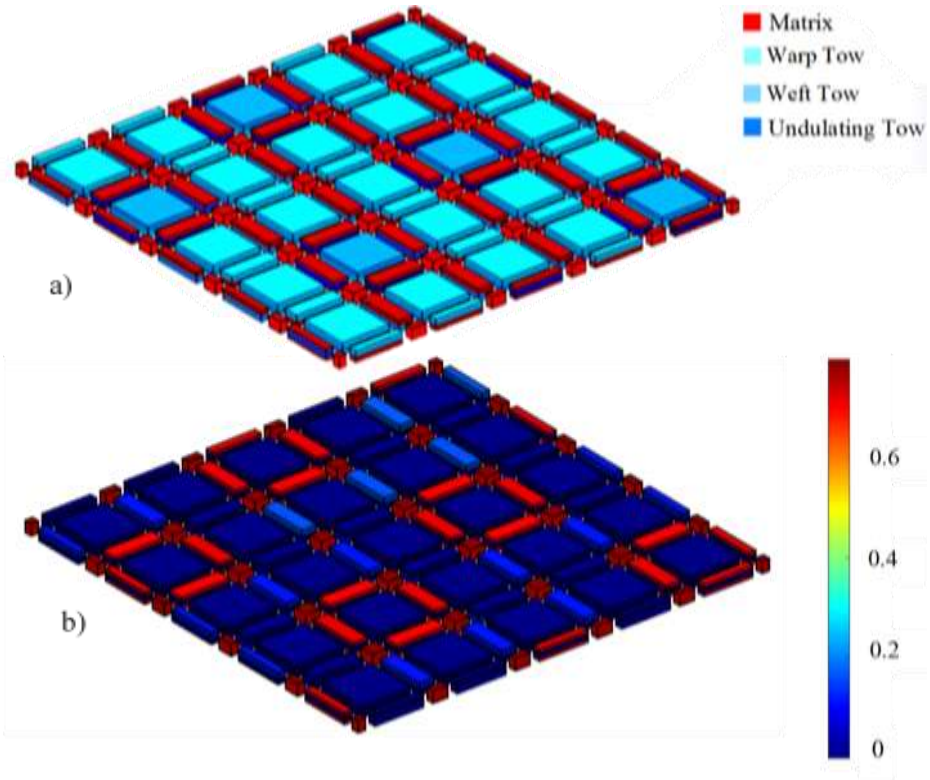

Figure 3.17. Damage in the 5HS RUC. (a) Simulated Weave Architecture; (b) Microcracking Damage (D_c) in Weave RUC at 0.25% Strain

The fracture mechanics-informed matrix microcracking damage model effectively captures first matrix cracking, which results in deviation from linear elastic material behavior, but initial material nonlinearity is not captured using only the microcracking damage model. When porosity effects are introduced, both nonlinear elastic material behavior and first matrix cracking are captured. The effective woven composite modulus is presented in Figure 3.18 and key matrix damage mechanisms are indicated.

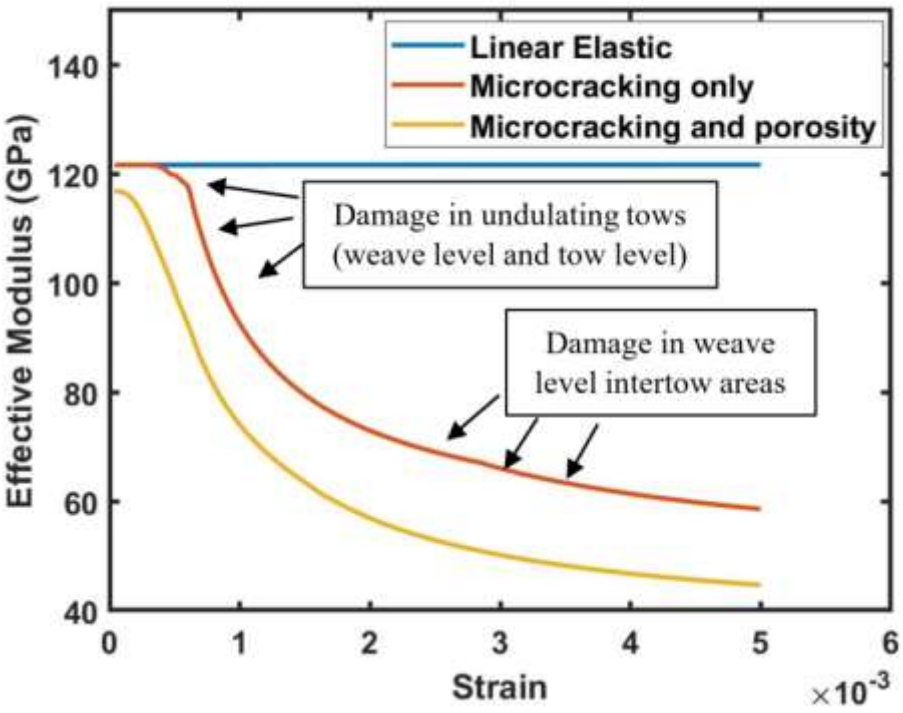

Figure 3.18. Effective Modulus of 2D Woven C/SiC CMC with Matrix Cracking and Porosity

3.4.4 Comparison with Literature

Yang et al. (Yang, Zhang, Wang, Huang, & Jiao, 2017) performed experiments across a range of temperatures using dogbone 2D woven C/SiC specimens machined from a CMC panel. The uniaxial tensile experiments were performed under displacement control at a quasistatic strain rate of $\sim 3x10^{-5}s^{-1}$. The simulations discussed in this chapter were displacement controlled at a comparable quasistatic strain rate of $1x10^{-5}s^{-1}$. The microcracking and porosity model predictions are in excellent agreement with room temperature experimental results as shown in Figure 3.19. By including the effects of both microcracking and porosity, this model accurately captures first matrix cracking and

material nonlinearity at low strains. At higher strains, the model deviates slightly from experimental results. This is most likely because the model fails to account for fiber damage, which becomes significant at higher strains. Additionally, the model does not account for inelasticity from mechanisms such as fiber pull out, crack face sliding, etc., which can cause appreciable nonlinearity at high strains.

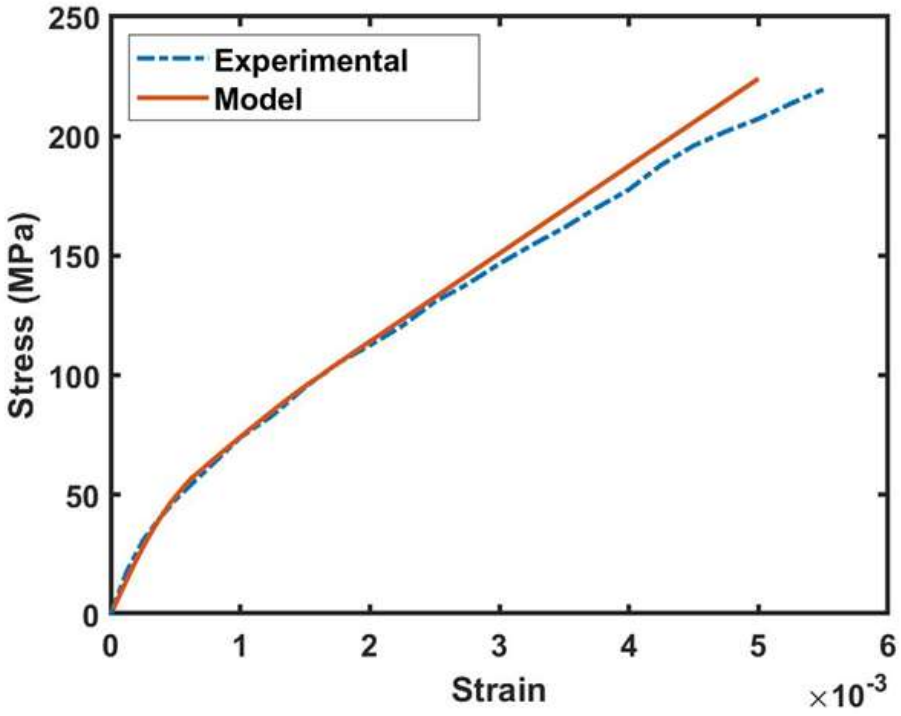

Figure 3.19. Comparison of Model (with Both Porosity and Matrix Microcracking) with Experimental Results from Literature

3.5 Temperature-dependent Reformulation

3.5.1 Reformulated Damage Model

Processing and operating temperatures have a significant impact on CMC deformation and damage behavior and should be accounted for to accurately capture the initial damage state of the material. Borkowski et al. (Borkowski & Chattopadhyay, 2015) used the MSGMC framework to capture the initial damage state of a UD C/SiC CMC due to cooldown from processing temperatures. That model effectively captured manufacturing induced damage in unidirectional CMCs due to large temperature differences between processing and operating temperatures and mismatch in coefficients of thermal expansion but did not consider damage caused by mechanical loading, and did not consider cooldown damage in a 2D woven CMC. Yang et al. (Yang, Zhang, Wang, Huang, & Jiao, 2017) modeled the tensile behavior of 2D C/SiC CMC at temperatures ranging from RT to 1200°C by idealizing the plain weave as a cross ply laminate and applying the shear lag approach and a stochastic crack evolution model. That model captures overall trends exhibited by experimental data but the predicted responses diverge from experimental results at elevated temperatures.

To account for these cooldown effects, the multiscale fracture mechanics-informed matrix damage model previously described in this section is reformulated and a unified damage ISV is introduced to capture effects of both matrix porosity and matrix cracking due to post-cooldown residual stresses and mechanical loading. Model calibration is performed using experimental data from Yang et al. (Yang, Zhang, Wang, Huang, & Jiao, 2017) for plain weave C/SiC at RT, 700°C, and 1200°C to determine how damage model

parameters change in this temperature range. The nonlinear predictive capabilities of the reformulated model are demonstrated for 1000°C and compared to the experimental results for this temperature. The predictions are in good agreement with experimental results

In the original formulation, two separate isotropic ISVs, D_p and D_c, were chosen to represent the damaged state of the material, with D_p representing the nucleation and growth of pores due to microstructural deformation with increasing volumetric strain (the pores act as crack precursors) and D_c representing matrix crack nucleation and propagation. In the temperature-dependent reformulation, however, both variables have been combined in single unified damage ISV to avoid potential issues from multiplying the effects of each damage variable as in the original formulation. By applying the principle of strain equivalence for a damaged medium and by taking partial derivatives, the following constitutive relationship can be obtained:

$$\sigma_{ij} = \rho \frac{\partial \psi}{\partial \varepsilon_{ij}} = C_{ijkl}\varepsilon_{kl}(1 - D), \tag{3.25}$$

where ψ, $\boldsymbol{C}$, ρ, $\boldsymbol{\sigma}$, and $\boldsymbol{\varepsilon}$ are as defined in the original formulation. The evolution of the unified damage ISV, D, can be determined using:

$$\dot{D} = \begin{cases} \dot{D}_p & K_I \leq K_{IC} \\ \dot{D}_c & K_I > K_{IC} \end{cases}. \tag{3.26}$$

The evolution equation for D_p remains unchanged from the original formulation, and the evolution equation for D_c becomes:

$$\dot{D}_c = \frac{\pi^2}{10}(1+\nu)(5-4\nu)\eta l^2 \dot{l}, \tag{3.27}$$

where η is a new, temperature-dependent parameter related to crack density and growth rate. An initial flaw size was assumed in the original formulation and calibrated to ensure crack activation at appropriate strains. In the reformulated model, no initial flaw size is assumed and instead the evolution of l is defined using a proportionality constant, b, to relate the flaw size before crack initiation to the porosity damage variable and after crack initiation to the stress intensity factors as follows:

$$\dot{l} = \begin{cases} b\dot{D}_p & K_I \leq K_{IC} \\ \dfrac{K_I - K_{IC}}{K_I - K_{IC}/2} & K_I > K_{IC} \end{cases}. \tag{3.28}$$

Defining the characteristic flaw size in this way allows the model to simulate both porosity and cracking deformation and damage mechanisms, and the porosity serves a crack precursor. Initially, the matrix degradation is dominated by the nucleation and growth of microstructural pores which grow until reaching a critical stress intensity factor. At this point, the stress intensity factor exceeds the fracture toughness of the material, matrix cracking is activated and becomes the dominant damage mechanism, and the continued effects of crack propagation are simulated.

In a real CMC material system, local failure can occur, causing load redistribution to surrounding regions of the material. However, due to the limitations of the first order displacement fields used in the formulation of MSGMC, failure of individual subcells (decreasing subcell stiffness to zero) has the effect of zeroing the stress in the entire row

and column of that subcell. This results in an unrealistic drop in the homogenized RUC stress at that length scale and unrealistically degrades the overall composite modulus. To avoid this issue, failure in individual subcells is not simulated and instead, a secant-tangent matrix damage model (Liu, Chattopadhyay, & Arnold, Impact of material and architecture model parameters on the failure of woven CMCs via the multiscale generalized method of cells, 2011) is employed to simulate the post-cracking matrix subcell behavior. This supplementary damage model is applied to failed subcells to prevent their stiffness from reaching zero, and the damaged normalized secant modulus, n, is calibrated to match the post-crack stiffness of the simulated CMC with the experimental results

3.5.2 Temperature-dependent Damage Model Parameters

Six parameters—a, b, η, $\sigma_{p_{max}}$, n, and D_0—from the damage model were identified as potential temperature dependent damage parameters. The $\sigma_{p_{max}}$ parameter is used in computing γ, the entropy dissipation rate, and represents the maximum stress at which porosity nucleation is possible. The use of this parameter allows the model to reflect the fact that pore growth significantly decreases at high stresses in a confined ceramic, such as the ceramic matrix in a CMC (Rubin, Vorobiev, & Glenn, 2000). The D_0 parameter allows the model to simulate effects of initial damage in the matrix material. The large temperature difference between processing and operating conditions for CMCs can produce significant damage and cracking due to high residual stresses that occur as a result of mismatch in constituents' coefficients of thermal expansion. The temperature dependent damage model parameters were calibrated using a nonlinear least squares regression optimization algorithm to minimize the difference between model results and experimental data from

Yang et al. (Yang, Zhang, Wang, Huang, & Jiao, 2017). This calibration was performed for plain weave C/SiC at RT, 700°C, and 1200°C to determine the value of each damage model parameter at these temperatures. The predicted values for each parameter at 1000°C were obtained by applying curve fitting to the resulting trends and were used to predict the CMC response at this temperature.

3.5.3 Results and Discussion

The responses of monolithic SiC (see Figure 3.20a) and UD C/SiC CMC (see Figure 3.20b) are simulated at room temperature using the reformulated damage model and are in good agreement with the original formulation. Figure 3.20a shows that the reformulated damage model retains the ability to capture the quasi brittle behavior of the SiC matrix material, while the results of the UD C/SiC simulation in Figure 3.20b confirms that the reformulated model captures first matrix cracking.

Figure 3.21 shows the simulated response of a 2D plain weave C/SiC CMC at room temperature. The parameters of the reformulated damage model were calibrated with the experimental results from Yang et al. (Yang, Zhang, Wang, Huang, & Jiao, 2017) using nonlinear least squares regression to obtain the optimum combination of parameters to allow the model to best approximate the experimental response. The calibrated parameters for the RT response are presented in Table 3.4. The reformulated model is in good agreement with the original formulation and correlates well with experimental results. It is important to note that failure is not included in either the original or reformulated damage model. Instead, simulation results are only included for strains within a range similar to the range of the experimental strain

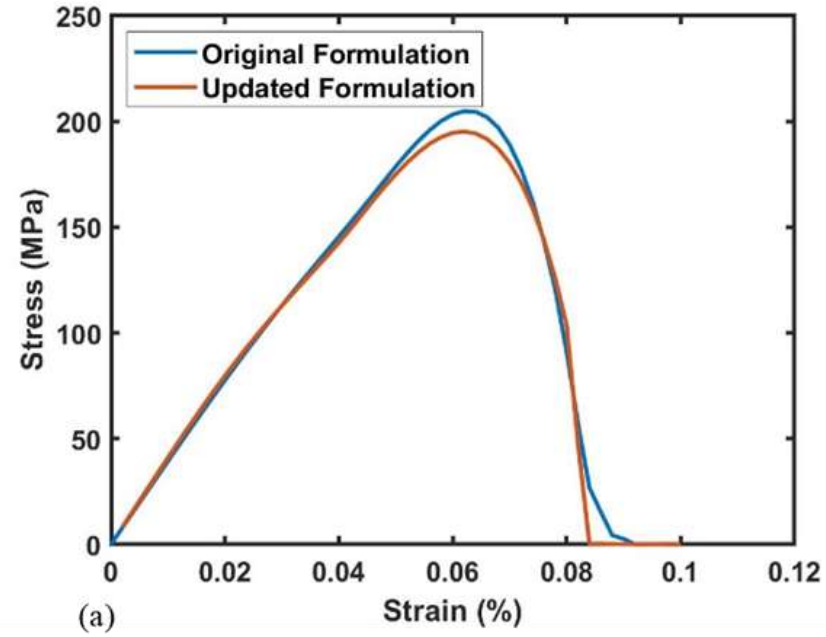

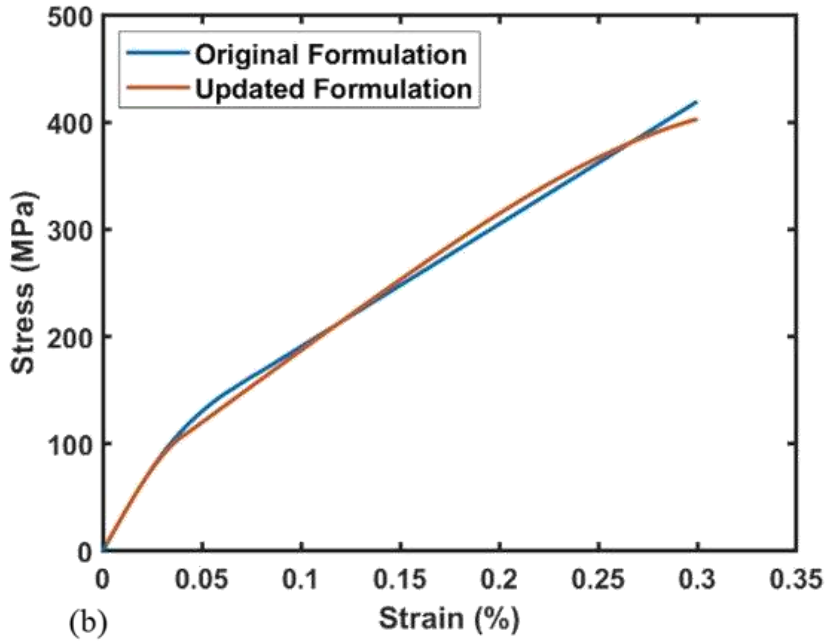

Figure 3.20. Comparing Original Formulation with Updated Formulation. (a) Monolithic SiC; (b) UD C/SiC (e.g. Minicomposite)

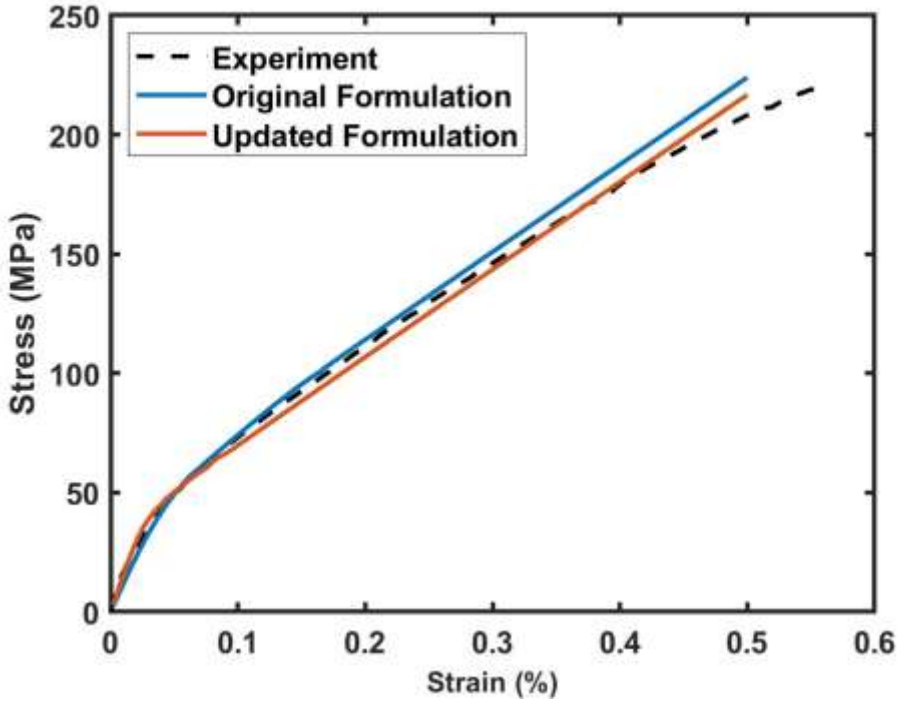

Figure 3.21. Comparison of RT Experiments to Simulation Results from Original and Updated Frameworks for Plain Weave C/SiC CMC

Table 3.4. Calibrated RT Model Parameters

a	b	η	$\sigma_{p_{max}}$ (MPA)	n	D_0
5800	$4.6x10^{-3}$	0.016	160	0.22	0.09

Additional model calibration was conducted to obtain the optimum temperature dependent model parameters to simulate the response of a 2D plain weave C/SiC CMC at 700°C and 1200°C. The experimental data for the 1000°C case was set aside to evaluate the predictive capabilities of the model and was not used to calibrate model parameters. Figure 3.22 shows that the reformulated dependent damage model can accurately represent

the temperature dependent response of the CMC across a wide temperature range. In this figure, the color of the curve corresponds to the temperature, solid curves represent the simulated response, and dashed curves represent experimental results. The calibrated model parameters and temperature trends for each parameter are shown in Figure 3.23. These trends can provide insight into the temperature dependent CMC deformation and damage behavior. For instance, the monotonically decreasing behavior of the porosity scaling parameter, a, indicates that the magnitude of the porosity damage variable growth rate decreases with increasing temperature. The increasing behavior of the proportionality constant, b, which relates the flaw size before crack initiation to the value of the porosity damage variable (effective size of pores/crack precursors), indicates that while the growth rate of the porosity variable may decrease, the effective size of the flaws increases with temperature. This agrees with expectations and results in earlier crack activation. A monotonically increasing trend is also displayed by the crack density/crack growth rate parameter, η, indicating that the severity of cracking and rate of crack extension will increase with temperature. In this case, however, the effects become more pronounced with temperature, indicating that for extremely high temperatures beyond the range studied in this work, crack growth and subsequent fracture would be even more severe and would occur more rapidly. Again, this supposition aligns with expectations. The decreasing trend of $\sigma_{p_{max}}$ implies that the maximum stress at which porosity nucleation is possible decreases with temperature. The post-cracking damage parameter, n, shows no clear temperature trend and will be discussed later. Finally, the initial damage parameter, D_0, decreases with temperature at a decreasing rate. This indicates that at a temperature beyond those investigated in this work, D_0 would be zero. This aligns with expectations since the

initial damage is a result of residual stresses due to cooldown from processing temperatures to operating temperatures. At higher operating temperatures, the residual stresses are lower, and the initial damage is not as severe. In the extreme case where the operating temperature and processing temperatures were identical, there would be no residual stresses, and zero initial damage due to cooldown.

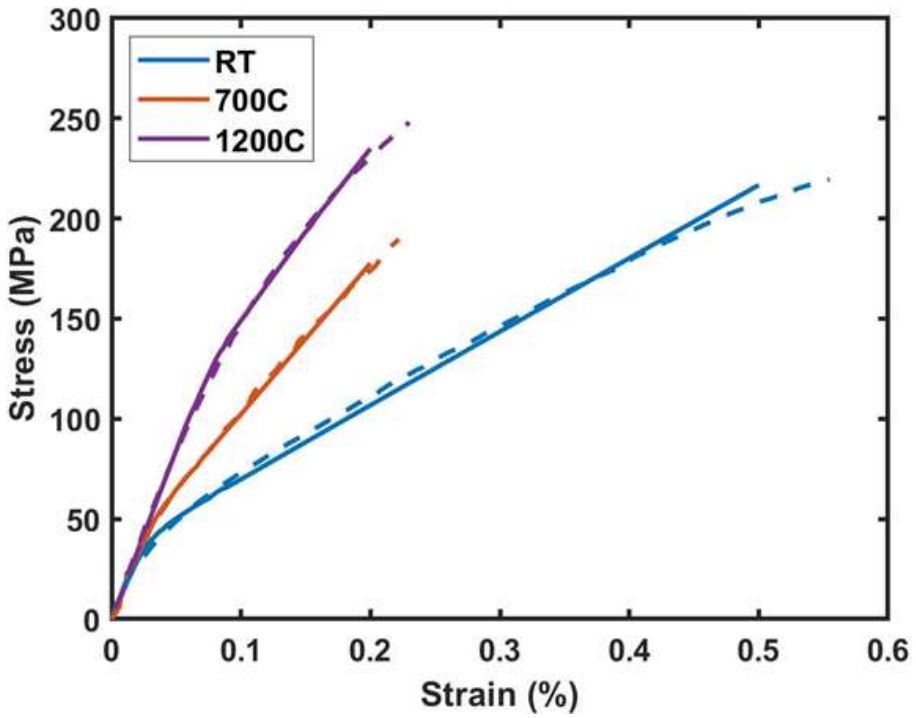

Figure 3.22. Temperature-dependent Model Results Compared with Experimental Data

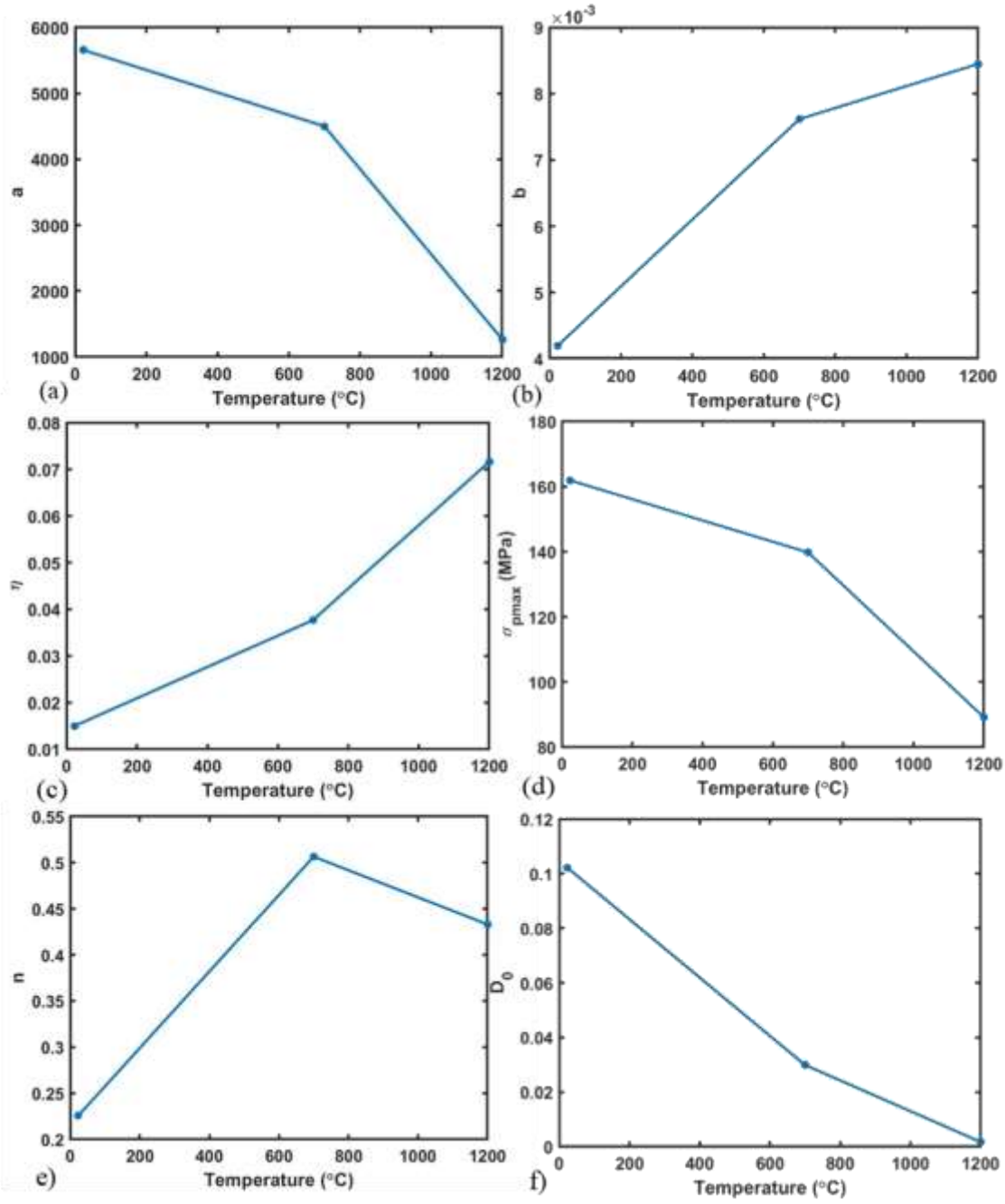

Figure 3.23. Damage Model Parameter Temperature Trends. (a) Porosity Scaling Parameter; (b) Effective Pore Size Proportionality Constant; (c) Crack Density/Growth Rate Parameter; (d) Maximum Porosity Nucleation Stress; (e) Post-cracking Secant-tangent Damage Parameter; (f) Initial Damage Parameter

The nonlinear, temperature dependent predictive capability of the model is demonstrated in Figure 3.24, which compares the predicted response at 1000°C to the experimental response at this temperature. The predicted damage model parameters at 1000°C were chosen to match the temperature trends of each parameter as shown in Figure 3.23. With more data points (experimental results from additional temperatures), more complex relationships could be investigated to better capture the effects of temperature on each parameter. In this case, however, the lack of experimental results precludes more accurate investigation, and only simple linear fits were applied to each parameter. A linear fit is deemed appropriate for the purposes of this study, since the overall temperature trends for each parameter within the range of RT to 1200°C are retained. However, more accurate relationships (sigmoidal or exponential trends) would be necessary to attempt to predict the CMC response outside the temperature range investigated in this work. It is also important to note that a linear fit is not appropriate for the post-cracking secant-tangent damage parameter since it does not display a monotonic temperature trend. In this case, the average value of the parameter for RT, 700°C, and 1200°C is used as the predicted value for 1000°C. This parameter will be investigated in future work to better understand its dependence on temperature and how to obtain appropriate predicted values within the relevant temperature range. Thermomechanical experiments will also be performed in the future to obtain additional experimental data so that more accurate temperature-dependent damage model parameter relationships can be obtained. The predicted parameter values at 1000°C, obtained from fitting the data for the RT, 700°C, and 1200°C cases, are compared to the values obtained through calibration with experimental data for 1000°C in Table 3.5. The predicted and calibrated values are in good agreement and validate the predictive

capabilities of the temperature dependent model within the temperature range considered in this work.

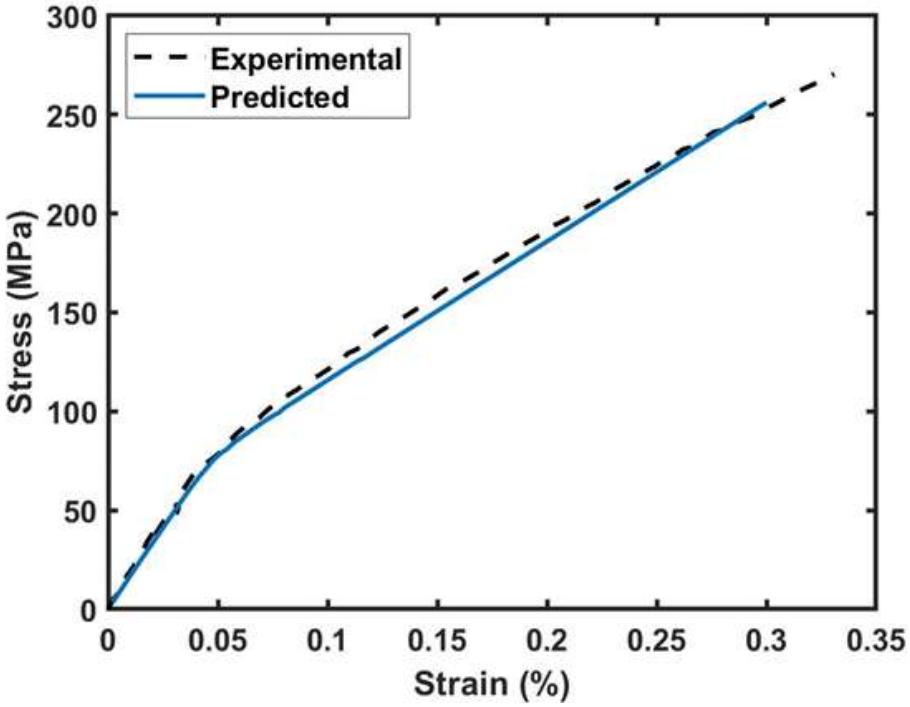

Figure 3.24. Predicted Response Compared to Experiment for 1000°C

Table 3.5. Predicted and Calibrated Parameters for 1000°C

	a	b	η	$\sigma_{p_{max}}$ (MPA)	n	D_0
Predicted	2480	$8.08x10^{-3}$	0.058	109	0.388	0.014
Calibrated	2400	$8.3x10^{-3}$	0.051	103	0.36	$6.1x10^{-3}$

3.6 Conclusions

A physics-based multiscale CMC matrix damage model was developed using ISV theory within a thermodynamic framework. The stress-strain constitutive behavior of damaged ceramic matrix material was derived using damage variables to describe the effects of matrix cracking and porosity nucleation and growth. The matrix cracking damage variable captures the effects of first matrix cracking and is determined using fracture mechanics and the self-consistent scheme. This ISV is activated when stress intensity factors exceed the fracture toughness of the material, and its evolution is governed by crack growth kinetics. The porosity ISV is a function of the volumetric strain, and its evolution depends on material entropy dissipation. The addition of this ISV allows the model to capture material nonlinearity at low strains. The nonlinear predictive capabilities of the material model were demonstrated for monolithic silicon carbide, UD C/SiC CMC, and a 2D woven C/SiC CMC and the simulation predictions are in excellent agreement with experimental results for 2D woven C/SiC CMCs from the literature. However, some limitations should be noted on the damage model described in this chapter, namely that this model does not account for the effects of fiber damage or debonding as a result of imperfect interfaces. This is suitable for predicting CMC behavior at small to intermediate strains, but at higher strains these effects contribute additional nonlinearity and inelasticity. Future work will include investigation into the effects of fiber damage and imperfect interfaces to improve simulation accuracy at higher strains.

The damage model provides valuable insight into the multiscale matrix damage behavior of CMCs that is difficult and expensive to obtain by experimentation. The model

predicts that matrix cracks initiate in the matrix surrounding undulating tows and links this localized tow level damage to the resulting overall composite degradation. The model also predicts arrested tow level damage progression as cracks propagate in the matrix rich interweave regions between tows. At intermediate to high strains, these matrix rich interweave regions have higher values for the damage ISV than the undulating tow matrix subcells where damage initiated. To obtain this information without a model would require extensive experimentation and serial sectioning on damaged CMCs at various levels of strain to determine matrix crack density in each part of the weave. Additionally, since the model is based on the physics of matrix cracking and accounts for fracture mechanics and crack growth kinetics across multiple length scales, the predictive capabilities of the damage model are not limited to a specific CMC architecture. Any arbitrary 2D or even 3D woven CMC architectures can be simulated using this framework simply by defining different weave level RUCs for each architecture and applying the same recursive localization/homogenization algorithms and the same constitutive damage relations at each scale.

The temperature-dependent reformulated CMC matrix damage model accounts for CMC matrix damage initiation and propagation behavior for temperatures ranging from room temperature to 1200°C. A unified damage model, which captures combined effects of both matrix porosity and matrix crack initiation and propagation, is implemented and temperature-dependent damage model parameters are calibrated with experimental data from literature for plain weave C/SiC CMC at RT, 700°C, and 1200°C. The predictive capabilities of the temperature-dependent reformulated model are demonstrated for 1000°C

using the temperature trends of each parameter to obtain expected damage model parameters at this temperature. The predicted response is in good agreement with experimental results, indicating that the model can be used to predict the temperature-dependent response of 2D woven CMCs within the temperature range considered in this work.

It is important to note that elastic properties were assumed to be approximately constant across the temperature range in this work. Temperature-dependent elastic properties will be included to better simulate the effects of temperature on CMC deformation behavior in future iterations of the model. In the current work, the effects of initial damage due to cooldown from processing to operating temperatures are captured using the initial damage parameter, D_0, which is calibrated to fit experimental data. This captures the average effects of cooldown damage on all matrix subcells and is dependent on calibration. In the future, cooldown will be explicitly modeled to obtain actual residual stresses in the CMC weave. Performing these cooldown simulations and applying the reformulated damage model will result in a more realistic initial damaged state and will improve predictive capability by reducing dependence on calibration. Additionally, future work will include thermomechanical experiments to provide sufficient experimental data to obtain improved temperature-dependent damage model parameter relationships and to experimentally validate the reformulated damage model.

4 TEMPERATURE-DEPENDENT CERAMIC MATRIX COMPOSITE DAMAGE MODEL WITH THERMAL RESIDUAL STRESSES AND MANUFACTURING-INDUCED DAMAGE

4.1 Introduction

In this chapter, the multiscale thermomechanical simulation framework discussed in the previous chapter is further developed and implemented using MSGMC to capture the temperature-dependent damage behavior of woven CMCs. The framework consists of cooldown simulations, which capture a realistic material initial state, and subsequent mechanical loading simulations to capture the temperature-dependent nonlinear stress-strain behavior. A fracture mechanics-informed thermomechanical progressive damage model previously developed is reformulated and extended to capture manufacturing-induced damage and to simulate the temperature-dependent mechanical response of 2D plain weave CVI C/SiC CMCs at temperatures ranging from RT to 1200°C. Additionally, a secant-tangent matrix damage model (Liu, Chattopadhyay, & Arnold, Impact of material and architecture model parameters on the failure of woven CMCs via the multiscale generalized method of cells, 2011) is employed to capture the homogenized effects of local subcell failure and simulate the post-cracking matrix subcell behavior. Model calibration was conducted using experimental data from the literature for RT, 700°C, and 1200°C. The experimental data for the 1000°C case was set aside for validation purposes and to evaluate the predictive capabilities of the model. Experimental data from the 1000°C case was not used to calibrate model parameters. The model agrees well with experiments and can effectively predict the CMC response within the temperature range studied in this chapter.

With minor modification, the model can simulate the temperature-dependent response of nearly any woven brittle-matrix composite. To demonstrate this capability, the model has been applied to simulate the temperature-dependent thermomechanical response of a 2D woven 5HS CVI/MI SiC/SiC CMC and shows excellent agreement with experiments. The Curtin progressive fiber filament failure model (Curtin, 1991), which has been adapted for use in GMC-based models (Bednarcyk & Arnold, 2001), is used in this work to capture the stochastic nature of progressive fiber failure in SiC/SiC CMCs.

This chapter is organized as follows: Section 4.2 describes the thermomechanical model framework, including the multiscale model, the cooldown simulations, and fiber and matrix damage models applied during cooldown and subsequent mechanical loading simulations. Section 4.3 presents and discusses the model results for monolithic SiC, plain weave C/SiC, and 5HS SiC/SiC CMCs. Section 4.5 discusses the experimental setup and initial results from RT testing of S200H C/SiNC CMCs. Finally, the last section concludes the chapter and provides a summary of findings

4.2 Model Description

4.2.1 Multiscale Modeling Framework

The temperature dependent matrix damage model is applied to the cooldown simulations and subsequent mechanical loading simulations using the MSGMC framework. This methodology enables prediction of a realistic residual stress profile with corresponding as-produced damage for various use temperatures and permits accurate temperature-dependent simulations to capture the matrix damage behavior of various

woven CMC material systems across a wide temperature range. The relevant length scales for a 2D woven CMC are the microscale (fiber/matrix level), mesoscale (tow level), and macroscale (weave level) as indicated in Figure 3.4 from the previous chapter, which shows an idealized 5HS triply periodic weave representative unit cell (RUC) that is discretized into subcells. The simulated global strain is applied at the macroscale level to the weave RUC, and the subcell strains are obtained using localization. Each subcell of the macroscale RUC is then modeled using a doubly periodic mesoscale RUC which is in turn discretized into subcells. Additional localization is again performed to obtain the mesoscale RUC subcell strains. The subcells of the mesoscale RUC are modeled using a microscale RUC consisting of SiC matrix, C or SiC fiber (monofilament), and PyC or BN fiber coating (interphase) subcells. A final localization is performed to determine the strain of each monolithic constituent subcell, and the stress-strain constitutive relationship corresponding to the material is applied to determine stress.

The stresses at each length scale are determined using homogenization techniques. For the microscale RUCs, which are the subcells of the mesoscale RUC, the homogenized stress is obtained by volume averaging the stresses of each monolithic constituent subcell. This method results in the microscale RUC effective stiffness, which includes damage effects and depends on the microscale geometry and constituent material properties. Similarly, in the mesoscale RUCs, which are subcells of the macroscale RUC, the homogenized stress is obtained by volume averaging the stresses of each microscale RUC. The mesoscale RUC effective stiffness is also computed. Finally, the global macroscale RUC stress and the global homogenized damaged composite stiffness matrix are obtained

by volume averaging of the mesoscale RUCs. These localization/homogenization algorithms allow for an accurate semi-analytical solution that links scale-specific deformation and damage behavior to the global weave response.

4.2.2 Cooldown Simulations

The CVI matrix densification process commonly used to manufacture CMCs requires extremely high temperatures. By accounting for spatially and architecturally varying thermal properties, the framework developed in this work can capture realistic post-cooldown thermal residual stress profiles and initial damage states for woven CMCs. In this chapter, 2D plain weave C/SiC and 5HS SiC/SiC CMC material systems are simulated. The C/SiC material system modeled in this work consists of T300 carbon fibers with a PyC interphase material and CVI SiC matrix. The SiC/SiC material system consists of Sylramic-iBN fibers with a BN interphase material and CVI SiC matrix at the tow level and MI SiC matrix at the weave level. The CTE for the T300 carbon fibers and CVI and MI SiC matrix materials are shown in Figure 4.1, and the temperature-dependent Young's modulus for the CVI and MI matrix are shown in Figure 4.2. The temperature-dependent material properties for the PyC and BN interphases as well as for the Sylramic-iBN fibers are included in Table 4.1. The T300 fibers are modeled as transversely isotropic, and the CVI and MI SiC matrix as well as the PyC and BN interphase materials and the Sylramic-iBN SiC fibers are modeled as thermally and elastically isotropic. The T300 fiber elastic properties, which are assumed to be approximately constant over the temperature domain, are included in Table 3.3.

The simulated woven composite architecture is assembled as described in the previous section, and cooldown simulations are conducted to determine the thermal residual stresses. The processing temperatures, which are used as the beginning temperatures for the cooldown simulations, for the plain weave C/SiC material and the 5HS SiC/SiC material are assumed to be ~1200°C (Heidenreich, 2015; DiCarlo, 2015) and ~1400°C (DiCarlo, 2015), respectively. The actual cooldown rates are unpublished by the manufacturers, but gradual cooldown is assumed and simulated in increments of 1-4°C. The low cooldown rate implies that no significant thermal gradients occur due to the slow passive cooling. The damage model, which will be discussed in the following section, is applied to determine the as-produced damage in the weave due to the high thermal residual stresses before subsequent mechanical loading simulations at various temperatures are applied. By capturing realistic thermal residual stress profiles and initial damage states, this methodology allows more accurate simulations of temperature-dependent damaged CMC stress-strain behavior.

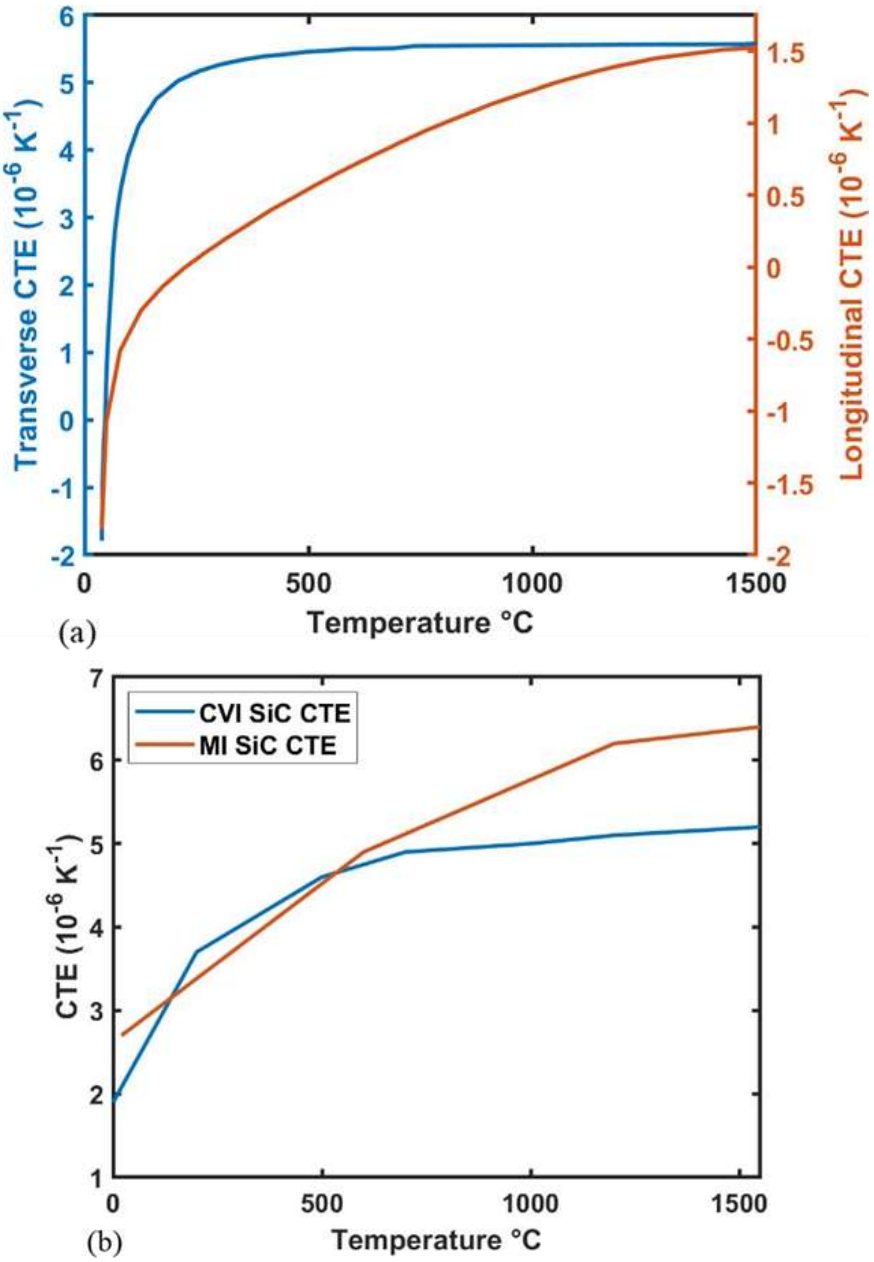

Figure 4.1. CTE vs. Temperature; (a) Longitudinal and Transverse CTE for T300 Carbon Fiber (Pradere & Sauder, 2008); (b) CTE for CVI (Rohm and Haas, 2008) and MI (Murthy, Mital, & DiCarlo, 1999) SiC Matrix

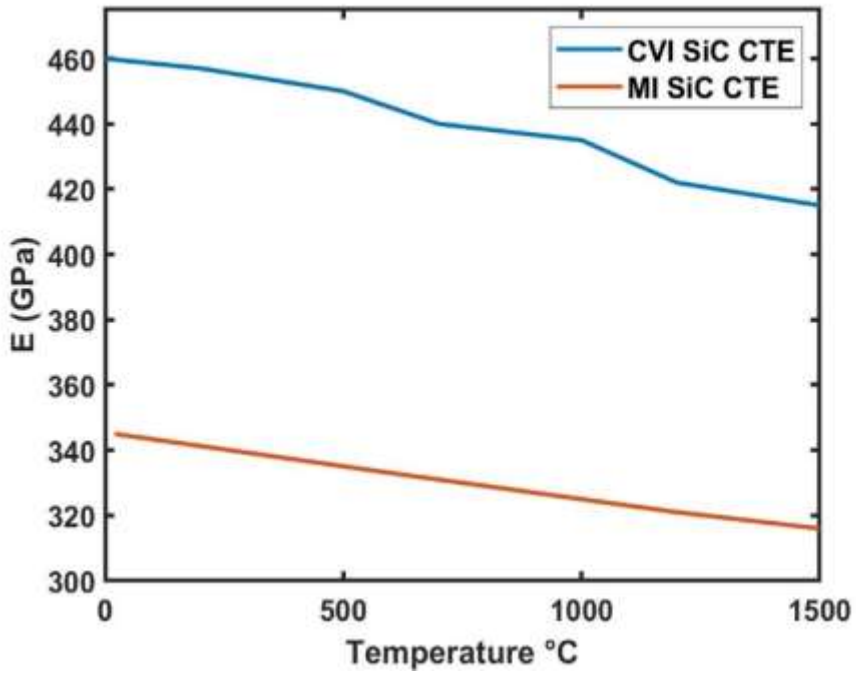

Figure 4.2. Young's Modulus vs. Temperature for CVI (Rohm and Haas, 2008) and MI (Murthy, Mital, & DiCarlo, 1999) SiC Matrix

Table 4.1. Temperature-dependent Material Properties for PyC and BN Interphase Materials and Sylramic Fibers

	CTE ($x10^{-6}$)		**E (GPa)**		$\boldsymbol{v}$	
	20°C	**1200°C**	**20°C**	**1200°C**	**20°C**	**1200°C**
PyC *	-1.12	1.7	20	20	0.23	0.23
BN **	6.3	3.7	20.3	14	0.22	0.22
Sylramic-iBN ***	5.4	5.4	400	365	0.17	0.17

* (Luo & Cheng, 2004)
** (Murthy, Mital, & DiCarlo, 1999; Gowayed, et al., 2010)
*** (Lipowitz, Rabe, Zangvil, & Zu, 1997; Ichikawa, 2016)

4.2.3 Damage Model

The matrix material stress-strain constitutive relationships are obtained as discussed in the previous chapter by taking the Helmholtz free energy as the scalar state potential of the material and assuming that it is completely described by the linear thermoelastic strain potential. The scalar state potential governs the evolution of state variables, which can be chosen to represent specific deformation and damage mechanisms. A unified isotropic damage internal state variable (ISV), D, is chosen to represent the damaged state of the material and includes effects of micropore nucleation and growth as well as matrix crack activation and propagation. The unified damage ISV is used in the damaged constitutive relationship obtained by applying the principle of strain equivalence for a damaged medium and by taking partial derivatives. The evolution of the unified damage ISV is defined as a piecewise function to represent the effects of two separate damage mechanisms in a single unified variable. Due to the brittle nature of the ceramic matrix material, the mode II and III SIFs play a negligible role in the rate of crack growth (Wachtman, Cannon, & Matthewson, 2009) and are not included in the model. The evolution equations for D_p, which captures effects of micropore (precrack) nucleation and growth, and D_c, which captures effects of matrix crack activation and propagation, are defined as follows:

$$\dot{D}_p = a\left(1 - D_p\right)\gamma\varepsilon^V \tag{4.1a}$$

$$\dot{D}_c = \frac{\pi^2}{10}(1+\nu)(5-4\nu)\eta l^2 \dot{l}, \tag{b}$$

where a is a temperature-dependent scaling parameter related to microporosity density, γ is the entropy dissipation rate defined by Rubin et al. (Rubin, Vorobiev, & Glenn, 2000), ε^V is the volumetric strain, ν is the Poisson's ratio, η is a parameter related to crack density

and growth rate, and l is the characteristic flaw size. Note that the parameter Γ_p, used in calculating γ as described in (Rubin, Vorobiev, & Glenn, 2000) has been modified to $\Gamma_p = \frac{3G}{\sigma_{eq}}$, where G is the shear modulus, and σ_{eq} is the equivalent stress. Additionally, note that the microporosity (precrack) density scaling parameter, a, is assigned two separate values in implementation to capture the precrack growth behavior during cooldown (a_0) as well as during mechanical loading (a_1). The evolution of l is defined as:

$$\dot{l} = \begin{cases} b\dot{D}_p & K_I \leq K_{IC} \\ \dfrac{K_I - K_{IC}}{K_I - K_{IC}/2} & K_I > K_{IC} \end{cases}, \tag{4.2}$$

where b is a proportionality constant relating the flaw size before crack initiation to the microporosity damage variable. As shown in Equation (4.2), after crack activation, the crack extension rate is computed using a modified form of the crack growth kinetic relationship given in Paliwal et al. (Paliwal & Ramesh, An interacting micro-crack damage model for failure of brittle materials under compression, 2008). Defining the characteristic flaw size in this way allows the model to simulate both microporosity and cracking damage mechanisms, and the transition from micropore (precrack) to matrix crack. Initially, the matrix degradation is dominated by the nucleation and growth of microstructural pores which grow as stress increases until the SIF due to the flaw exceeds a critical value. At this point, the SIF exceeds the fracture toughness of the material, matrix cracking is activated, and the continued effects of crack propagation are simulated as flaw growth is dominated by crack growth kinetics. This methodology aligns with the physical damage nucleation and propagation behavior of brittle materials. In these materials, micropores/precracks

form and then grow until reaching a critical size after which the flaw transitions to crack-like behavior and propagation (Evans, Rice, & Hirth, 1980).

As discussed in Chapter 3, matrix cracking in real CMCs is directionally dependent and causes local anisotropy. The anisotropic damage model developed in Equations (3.18) and (3.19) have been applied to capture this behavior in the model. The cracked matrix is assumed to be transversely isotropic in the plane of the crack, and matrix anisotropy occurs when the damaged stiffness tensor is rotated from the crack plane to the global axes. As a result of the rotation from principal axes, the resulting compliance tensor and the corresponding stiffness tensor are fully anisotropic in the global frame where loads are applied

In a real CMC material system, local failure can occur, causing load redistribution to surrounding regions of the material. This local failure and load redistribution behavior is difficult to capture explicitly using MSGMC. The first order displacement fields used in MSGMC endow the method with computational efficiency, but when combined with the imposed traction continuity requirements, failure of individual subcells (decreasing subcell stiffness to zero) results in entire subcell rows and columns being overly compliant. This in turn has the potential to cause the entire RUC to become overly compliant in some directions depending on the architecture. As a result, an unrealistic decrease in the homogenized RUC stiffness at that length scale can occur, and the overall composite modulus can be unrealistically degraded. To avoid this issue, failure in individual subcells is not explicitly simulated in this work. Instead, a secant-tangent matrix damage model (Liu, Chattopadhyay, & Arnold, Impact of material and architecture model parameters on

the failure of woven CMCs via the multiscale generalized method of cells, 2011) is employed to capture the homogenized effects of local subcell failure and simulate the post-cracking matrix subcell behavior. This supplementary damage model is applied to "failed" subcells to prevent their stiffness from reaching zero to avoid overly compliant material behavior. The damaged normalized secant modulus, n, is a calibrated parameter selected to match the post-crack stiffness of the simulated CMC with experimental results.

4.2.4 Fiber Damage Model

The failure strain of T300 carbon fibers used to simulate the response of the plain weave C/SiC CMC is approximately three times that of the ultimate strain for typical C/SiC CMCs at RT (Torayca). Failure in these CMC material systems is typically dominated by matrix damage and failure behavior that leads to failure at the weave level, and fiber failure plays a minor role in the global composite response. As a result, fiber damage is not included in the C/SiC CMC damage model. However, a matrix damage model alone is insufficient to fully capture the SiC/SiC damage response. The Sylramic fibers in the 5HS weave SiC/SiC CMC simulated as part of this study are stochiometric SiC fibers, and as such, have damage and failure behavior similar to that of the SiC matrix material. The Curtin progressive fiber filament failure model (Curtin, 1991), which has been adapted for use in GMC-based models (Bednarcyk & Arnold, 2001), is used in this work to capture the stochastic nature of progressive fiber failure in SiC/SiC CMCs. This modified Curtin model is based on fiber strength statistics combined with shear lag analysis and defines the damaged fiber modulus, $E_f^\star$, as follows:

$$E_f^{\star} = \frac{1}{2}\left[1 + \exp\left(-\left(\frac{\sigma_L}{\sigma_C}\right)^{m+1}\right)\right] E_f, \tag{4.3}$$

where E_f is the undamaged fiber modulus, σ_L is the fiber longitudinal stress, m is the fiber Weibull modulus, and σ_C is defined as:

$$\sigma_C = \left(\frac{\sigma_0^m \tau L_0}{r}\right)^{\frac{1}{m+1}}. \tag{4.4}$$

In this equation, σ_0 is the characteristic fiber strength, L_0 is the fiber characteristic length, r is the fiber radius, and τ is the fiber-matrix interfacial sliding resistance. The ultimate strength and failure strains predicted by the model are given by:

$$\sigma_f^{ult} = \frac{1}{2}\sigma_C h^{\left(\frac{1}{1+m}\right)}[1 + \exp(-h)], \tag{4.5}$$

$$\varepsilon_f^{ult} = \frac{\sigma_C}{E_f} h^{\left(\frac{1}{m+1}\right)}, \tag{4.6}$$

where h is the lowest positive number that satisfies:

$$1 + \big(1 - h(m+1)\big)\exp(-h) = 0. \tag{4.7}$$

The parameter values, σ_0, L_0, r, and m, were obtained from (Morscher & Martinez-Fernandez, 1999) and are 2.1 GPa, 25.5 mm, 4.5μm, and 5, respectively. The fiber-matrix interfacial sliding resistance parameter, τ, was assumed to be 10 MPa. For the 1200°C case, τ and m were assumed to be 1 MPa and 2, respectively, based on the high-temperature fiber data in (Morscher G. , 1997; Cao, et al., 1990).

4.2.5 Model Calibration

The damage model parameters used to simulate the scale-dependent matrix damage behavior in this work are obtained by calibrating with experimental results from the literature. Yang et al. (Yang, Zhang, Wang, Huang, & Jiao, 2017) performed experiments across a range of temperatures using dogbone 2D plain woven C/SiC specimens machined from a CMC panel. The longitudinal tensile experiments were performed under displacement control at a quasistatic strain rate of $\sim 3x10^{-5}s^{-1}$. The simulations discussed in this chapter were displacement controlled at a comparable quasistatic strain rate of $1x10^{-5}s^{-1}$. Gowayed et al. (Gowayed, et al., 2010) performed longitudinal tensile tests using flat 2D 5HS weave SiC/SiC specimens per EPM testing standards, which are equivalent to ASTM C1359, at RT and 1204°C. The experimental results from both studies are included in Figure 4.3, which clearly shows the proportional elastic limit (PEL) for the high temperature C/SiC load cases and both SiC/SiC load cases. The PEL corresponds to the onset of first macroscale matrix cracking (Liu, Chattopadhyay, & Arnold, Impact of material and architecture model parameters on the failure of woven CMCs via the multiscale generalized method of cells, 2011) and marks the transition between local, tow-level damage to intratow weave level damage. The RT C/SiC CMC load case has no obvious PEL because the high manufacturing-induced damage causes significant matrix cracking that rapidly extends under load and degrades material properties almost immediately. The PEL increases with temperature for the C/SiC CMC, despite a reduction in constituent properties with increasing temperature. This is primarily because the residual stresses and manufacturing-induced damage become less significant with increasing

temperatures. The SiC/SiC CMC has less mismatch in constituent thermal properties, so the manufacturing-induced damage is less severe. The higher constituent properties at RT combined with relatively low manufacturing-induced damage results in a higher PEL at RT than at high temperatures for SiC/SiC.

A critical objective of this work is to capture a realistic initial damage state resulting from thermal residual stresses due to cooldown from extreme processing temperatures. Micrographs of as-produced C/SiC CMCs (see Figure 4.4) show significant manufacturing-induced damage in the form of matrix cracking and transverse tow cracks. These initial manufacturing-induced damage mechanisms occur in specific areas withing the CMC weaves and show preferential orientations. The location and orientation of these as-produced cracks are governed by the thermal residual stress profiles which are themselves governed by the weave architecture and constituent thermal properties. The cooldown simulation framework described in this work accounts for these factors and captures realistic thermal residual stress profiles. Corresponding damage hotspots occur in regions consistent with those shown in Figure 4.4. This will be discussed in greater detail in the following sections.

The CVI/MI manufacturing method used to fabricate the SiC/SiC specimens simulated in this work results in a more dense matrix (see Figure 4.5) with less porosity and fewer open voids in the weave. Additionally, the CTEs of the individual constituents in the SiC/SiC CMC have significantly less mismatch compared to those of the C/SiC CMC. As a result, the SiC/SiC CMC has lower thermal residual stresses, and the CVI/MI SiC matrix material is more resistant to matrix cracking and transverse tow cracking because of

thermal shrinkage. The micrograph in Figure 4.5 shows significantly less initial damage compared to the C/SiC material in Figure 4.4. The results from the cooldown simulation framework developed in this work agree with this experimental observation, as will be shown in later sections.

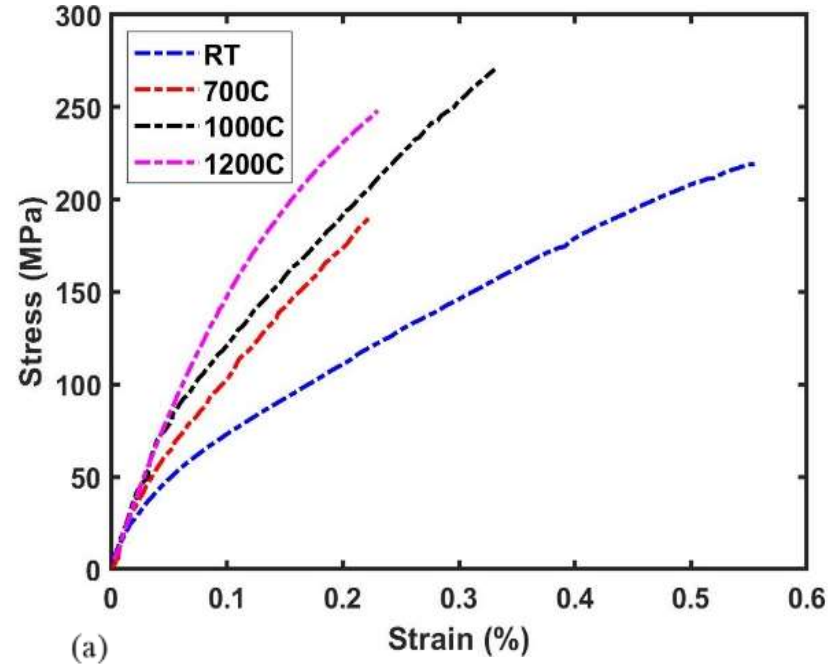

(a)

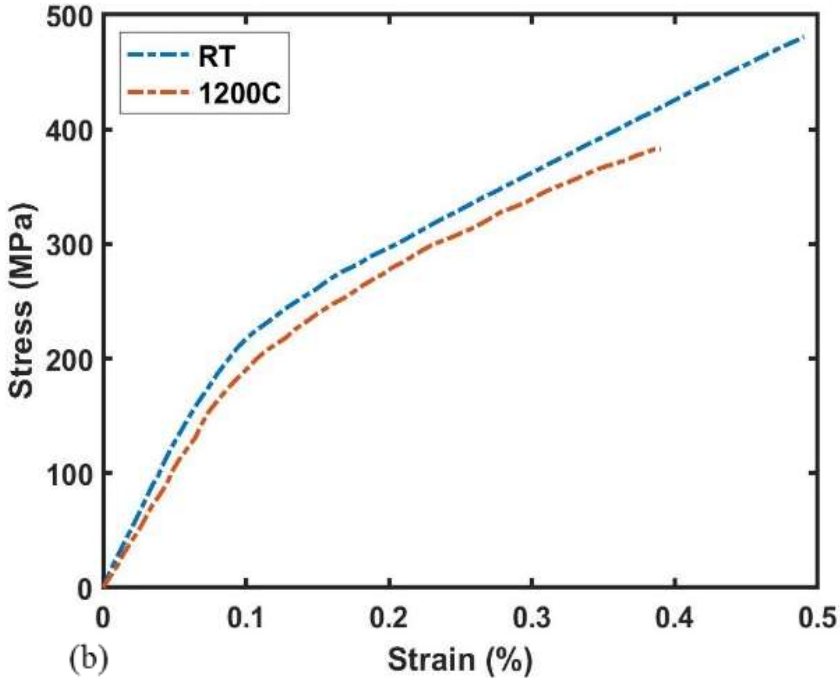

(b)

Figure 4.3. Experimental Longitudinal Stress-strain Response. (a) 2D Plain Weave C/SiC CMC (Yang, Zhang, Wang, Huang, & Jiao, 2017); (b) 2D 5HS Weave SiC/SiC CMC (Gowayed, et al., 2010)

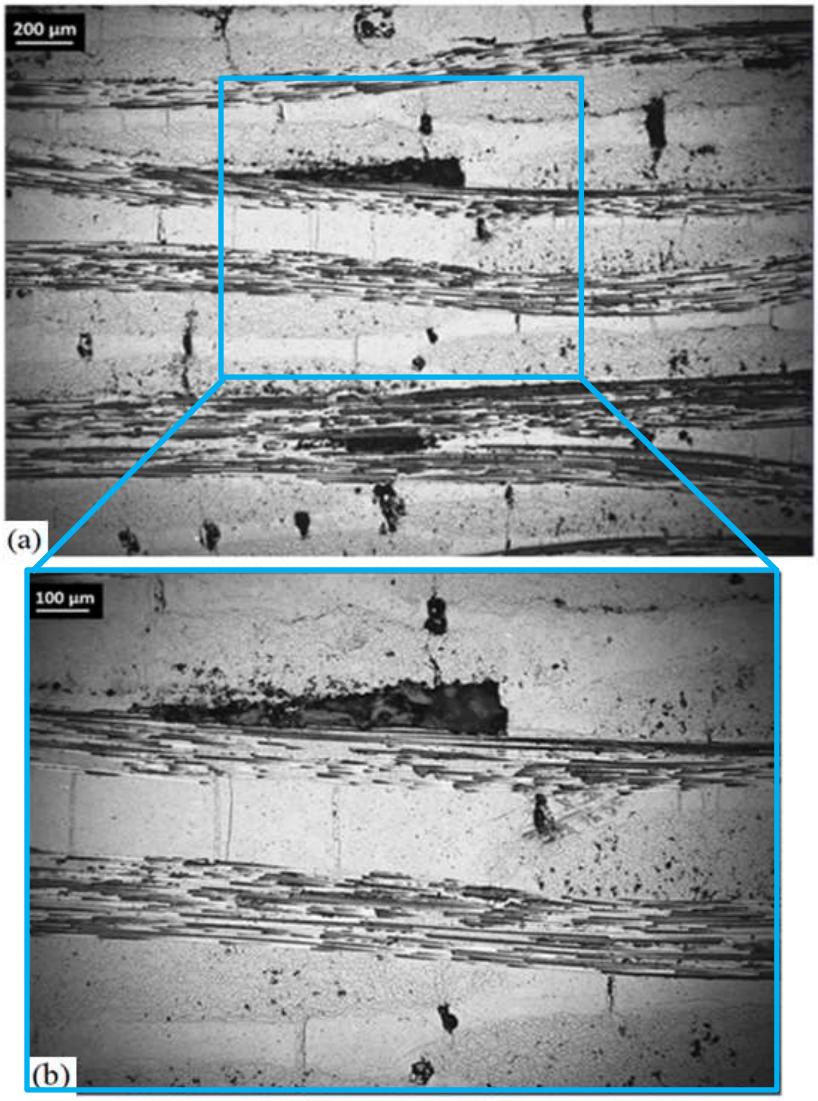

Figure 4.4. Micrographs Adapted from (Khafagy, Datta, & Chattopadhyay, 2021) Showing As-produced Damage with Preferential Orientation in C/SiC CMC. (a) Partial Specimen Cross Section; (b) Close-up View

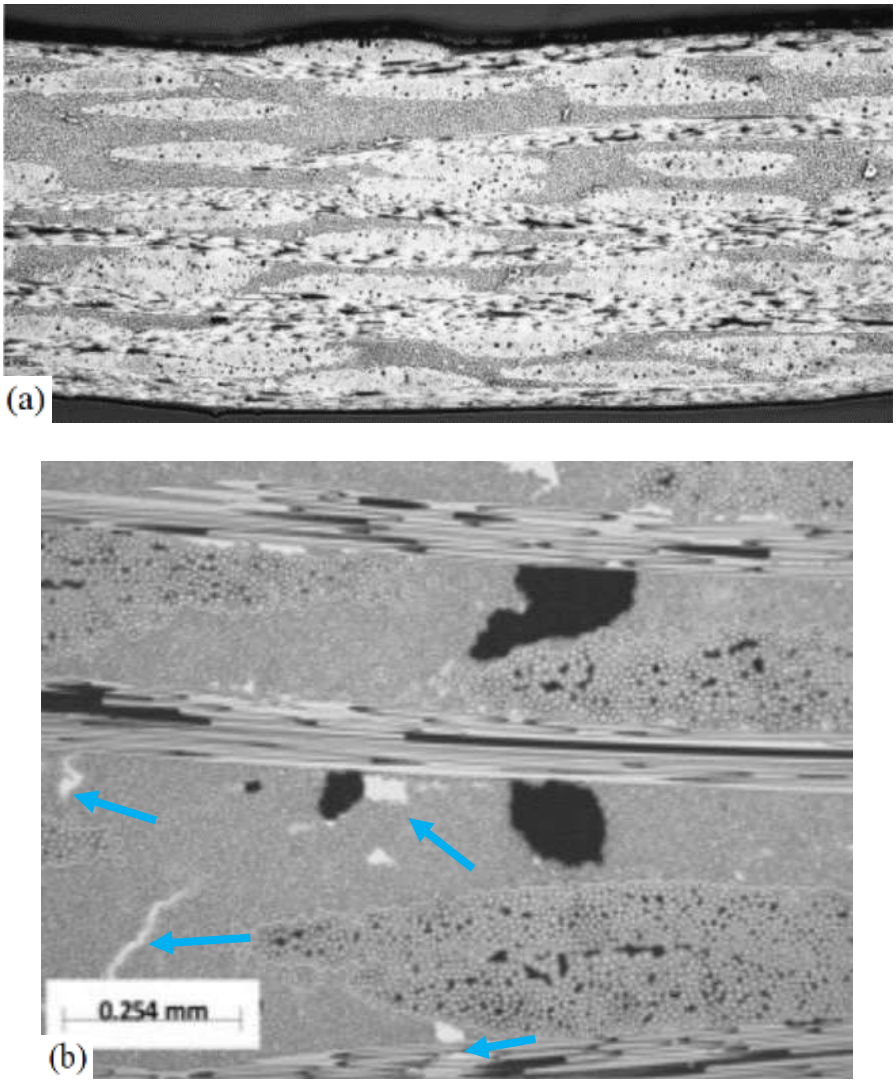

Figure 4.5. Micrographs Adapted from (Gowayed, et al., 2010) Showing As-produced damage in CVI/MI SiC/SiC CMC. (a) Specimen Cross Section; (b) Micrograph Showing Matrix Cracks and Voids Filled After MI Step

4.3 Results and Discussion

4.3.1 Monolithic SiC

The stress-strain response of bulk SiC matrix material is simulated and compared to the linear elastic case to demonstrate the capabilities of the damage model. In this case, the cooldown simulations have no effect because the monolithic SiC matrix material has no CTE mismatch, and therefore no thermal residual stresses. The quasi-brittle behavior of the SiC matrix material is captured and shown in Figure 4.6. The natural cracking behavior is displayed in Figure 4.7 (a), which shows the value of the total damage ISV. Initially, the damage behavior is dominated by micropore/precrack nucleation and propagation, which causes slight material nonlinearity at low strains. At approximately 0.04% strain, matrix cracks activate and damage propagation is dominated by matrix cracking and crack growth kinetics. The damage variable grows rapidly after crack activation and failure occurs shortly thereafter. To satisfy the governing thermodynamic requirements inherent in ISV theory, the temporal evolution of the damage ISVs must monotonically increase and satisfy normality conditions. These conditions are met by the dissipation-based definition of D_p below ~0.04% strain, and by the fracture mechanics-based definition of D_c after matrix crack activation. The piecewise definition of D and its growth rates are thermodynamically valid and agree with ISV theory. The effective modulus of the monolithic SiC material is shown in Figure 4.7 (b). Gradual material property degradation occurs because of the material dissipation associated with the formation and growth of micropores/precracks. After matrix crack activation, cracking propagates rapidly causing more significant material property degradation that continues until failure.

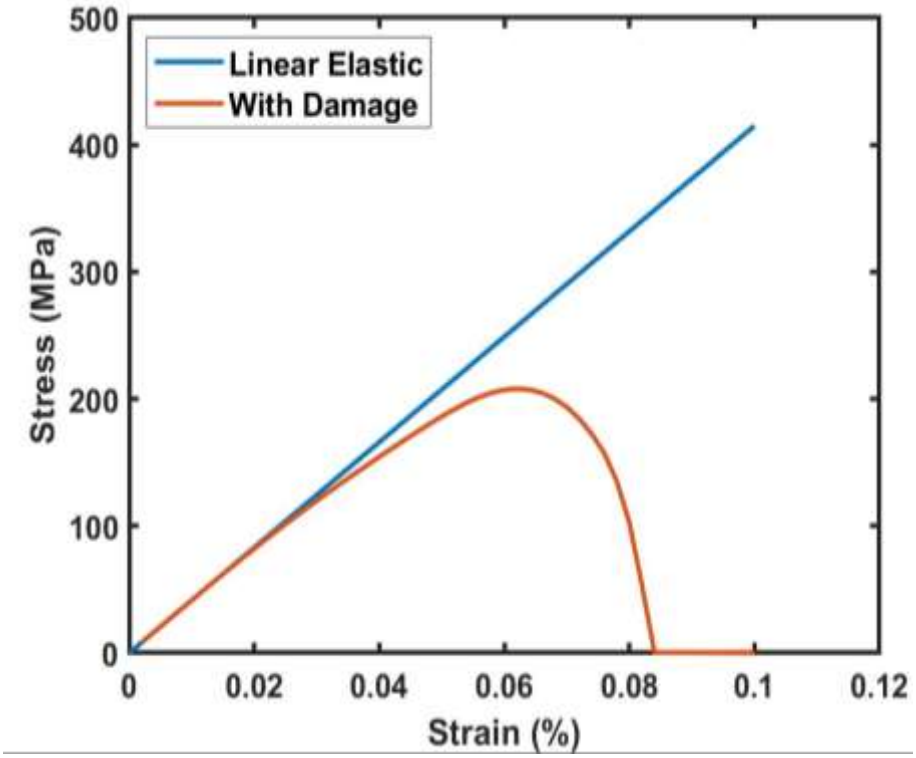

Figure 4.6. Simulated Stress-strain Response for RT Monolithic SiC

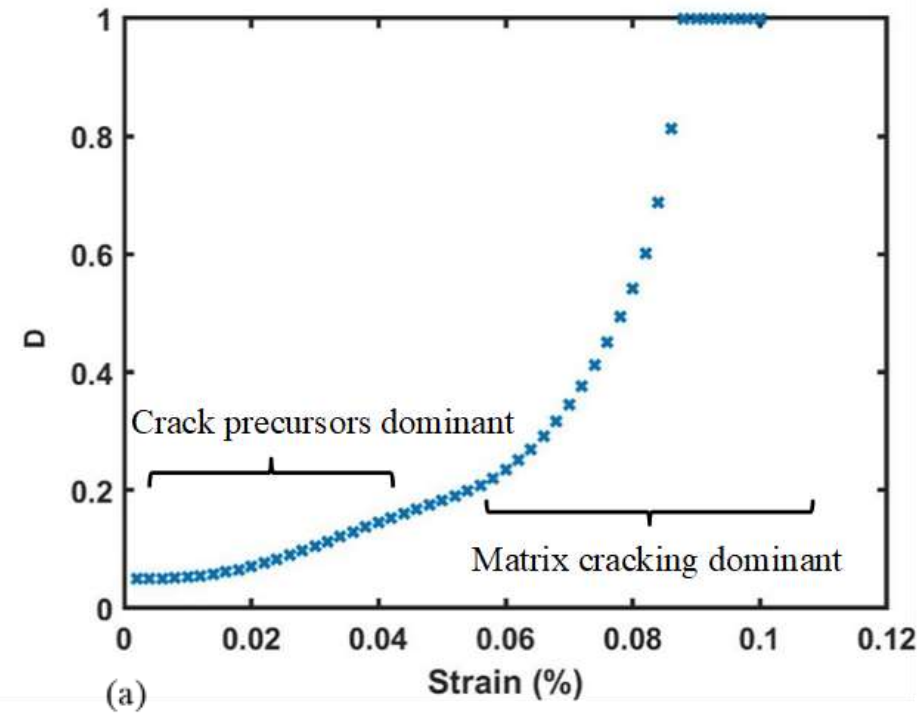

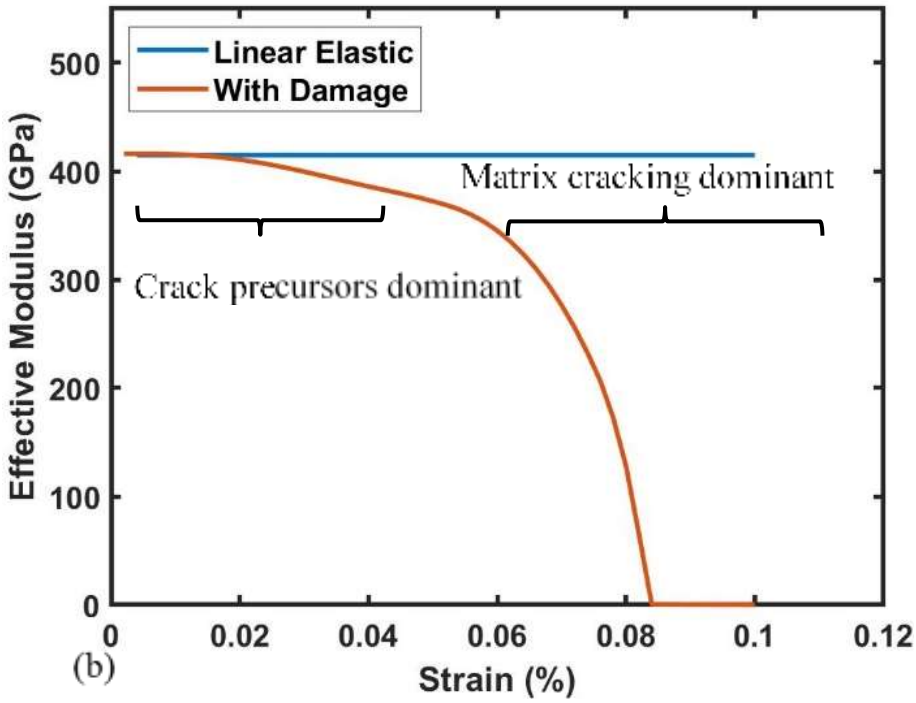

Figure 4.7. Simulation Results for RT Monolithic SiC. (a) Total Damage ISV vs. Strain; (b) Effective SiC Modulus vs. Strain

4.3.2 C/SiC

The initial thermal residual stresses resulting from cooldown from ~1200°C to RT in a 2D plain weave C/SiC CMC are shown in Figure 4.8. The same procedure was followed for all temperature cases (except with different final temperatures for the cooldown segment of the simulations), but only the RT case is included here for reference. The highest tensile stresses, which contribute the most to the cooldown-induced damage, occur in the transverse (weft direction) and longitudinal (warp direction) shown in Figure 4.8 (a) and (b), respectively. These high tensile stress areas correspond to regions in as-produced CMCs with matrix cracks and transverse tow cracks caused by material shrinkage as seen in Figure 4.4. The directionally dependent damage model is applied and results in degraded

properties in high stress areas according to the direction of the maximum principal stress in each matrix subcell. This results in a realistic anisotropic initial damage state for the simulated as-produced weave that includes damage hotspot areas. The temperature-dependent stress-strain responses are obtained by performing subsequent mechanical loading simulations.

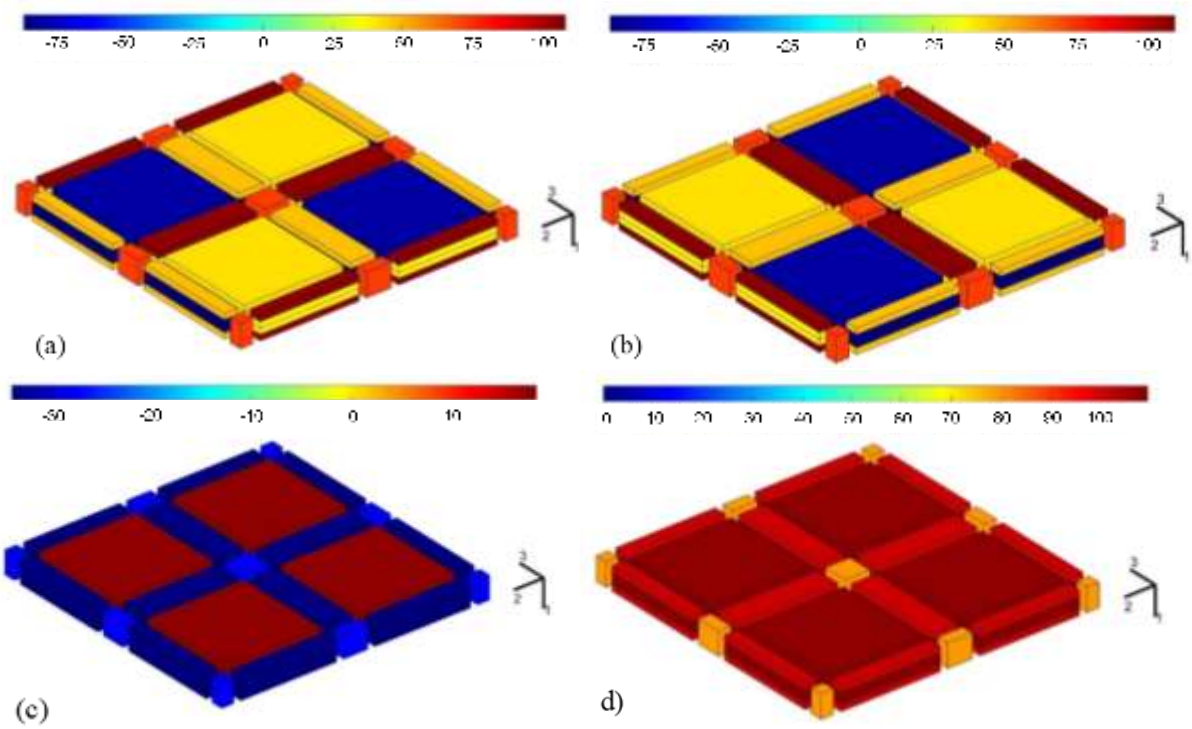

Figure 4.8. Simulated Thermal Residual Stresses for RT Plain Weave C/SiC CMC. (a) Residual Transverse Stress (Weft Direction); (b) Residual Longitudinal Stress (Warp Direction); (c) Residual Through-thickness Stress; (d) Residual Effective Stress

Model calibration was conducted using nonlinear least squares regression optimization techniques to obtain the optimum temperature dependent model parameters to simulate the response of a 2D plain weave C/SiC CMC at RT, 700°C, and 1200°C. The experimental

data for the 1000°C case was set aside to evaluate the predictive capabilities of the model and was not used to calibrate model parameters. The calibrated model parameters and temperature trends for each parameter are shown in Figure 4.9. The temperature trends of the model parameters can provide insight into the temperature-dependent CMC deformation and damage behavior. For instance, the monotonically decreasing behavior of the cooldown and mechanical loading microporosity scaling parameters, a_0 (Figure 4.9 (a)) and a_1 (Figure 4.9 (b)), indicates that the magnitude of the precrack damage variable growth rate decreases with increasing temperature. This aligns with expectations and experimental observations because the manufacturing-induced cooldown damage is less significant at higher operating temperatures. The decreasing behavior of the proportionality constant, b (Figure 4.9 (c)), which relates the flaw size before crack initiation to the value of the porosity damage variable (effective size of micropores/crack precursors), indicates that the relationship between the effective size of the flaws and the value of the precracking damage ISV decreases with temperature. A weak monotonically increasing trend is displayed by the crack density/crack growth rate parameter, η (Figure 4.9 (d)), indicating that the severity of cracking and rate of crack extension will moderately increase with temperature. In this case, the effects become more pronounced with temperature, indicating that for extremely high temperatures beyond the range studied in this work, crack growth and subsequent fracture would be even more severe and would occur more rapidly. This aligns with expectations and experimental observations. A weak monotonically increasing trend is displayed by n (Figure 4.9 (e)), the post-crack secant-tangent modulus that ensures subcell stiffness is not reduced completely to zero to prevent overly compliant simulated material behavior. Because n is a numerical feature of the model, no physically meaningful

interpretation of this parameter's temperature-dependent trends can be inferred. Unfortunately, the lack of published temperature-dependent CMC stress-strain response data limits confidence in the observed trends of each parameter. Published experimental data for equivalent material systems and loading conditions was available for four temperatures, leaving only three for model calibration and one for prediction and model validation. The authors are currently planning in-house tests to collect data at additional temperatures, which will allow more in-depth investigation into the temperature trends of each model parameter and will increase confidence in the temperature trends of the model parameters.

The multiscale cooldown and thermomechanical simulation framework and damage model can accurately represent the nonlinear stress-strain response of the CMC across a wide temperature range, as shown in Figure 4.10. In this figure, the color of the curve corresponds to the temperature, solid curves represent the simulated response, and dashed curves represent experimental results. The model accurately captures the dominant damage behavior of the brittle matrix CMCs. At low strains, the damage growth is dominated by tow-level crack initiation and propagation in the undulating tows. This corresponds to the initial nonlinearity in Figure 4.10. As strain increases, matrix cracking saturates in the undulating tows and cracks initiate in non-undulating tows just before the PEL (transition between tow-level damage and macroscale matrix cracking, as discussed in Section 4.2.5). This is reflected in the model, and matrix crack activation in the intratow matrix corresponds to the rapid drop in stiffness at the PEL. As strain increases, matrix cracks

continue to propagate in the intratow weave-level matrix subsells before reaching saturation.

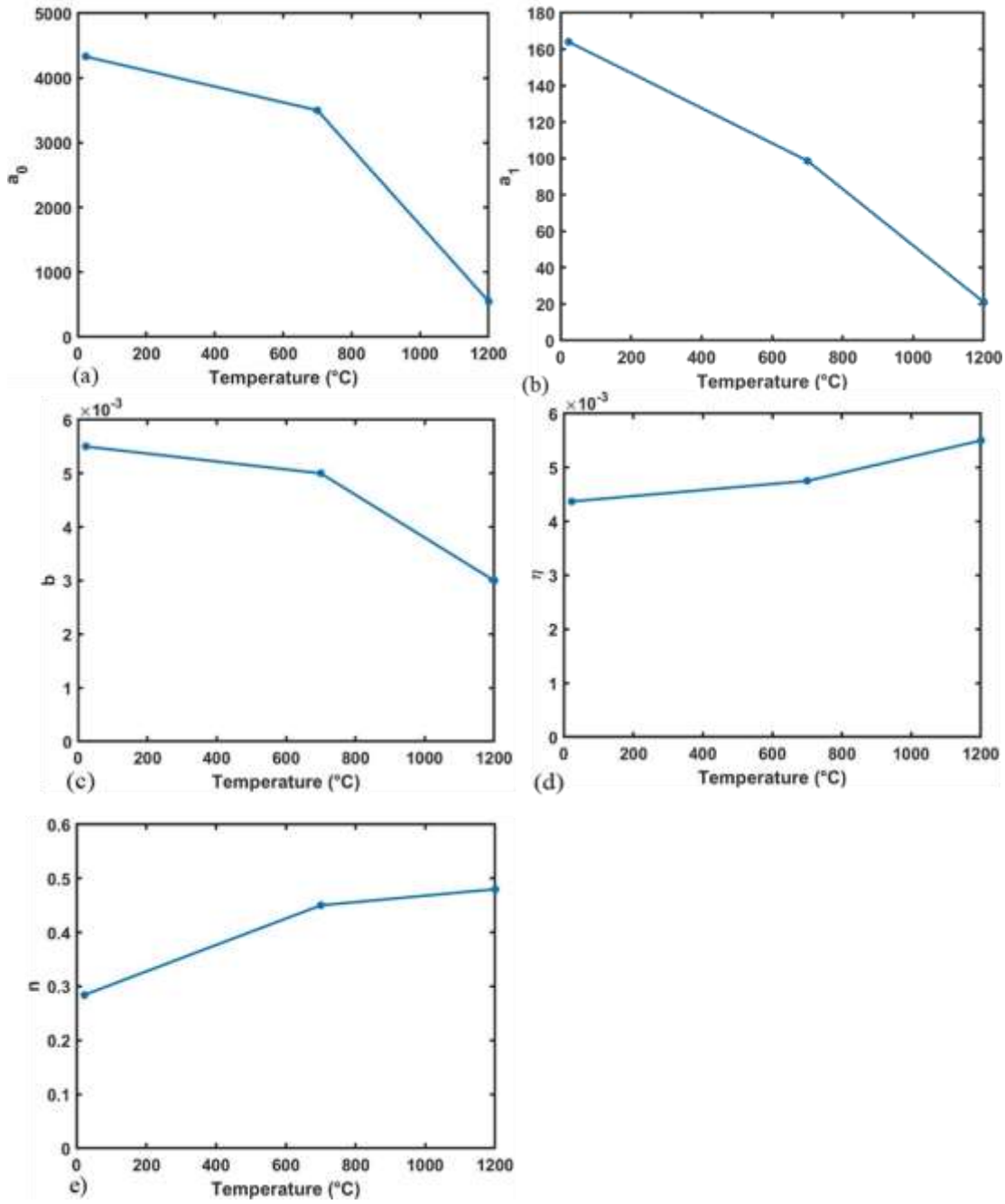

Figure 4.9. Damage Model Parameter Temperature Trends. (a) Porosity Scaling Parameter—Cooldown; (b) Porosity Scaling Parameter—Loading; (c) Effective Pore Size

Proportionality Constant; (d) Crack Density/Growth Rate Parameter; (e) Post-cracking Secant-tangent Damage Parameter

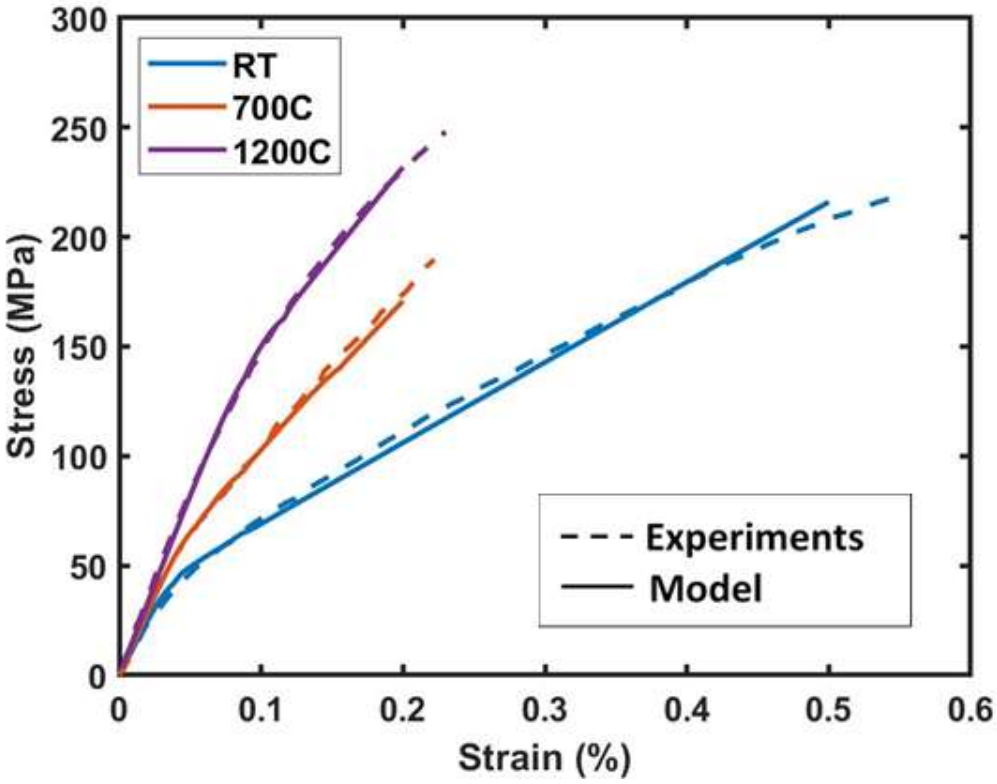

Figure 4.10. Temperature-dependent Model Results Compared with Experimental Data from Ref. (Yang, Zhang, Wang, Huang, & Jiao, 2017)

4.3.3 Predictive Capability

The nonlinear, temperature dependent predictive capability of the model is demonstrated in Figure 4.11, which compares the predicted response at 1000°C to the experimental response at the same temperature. The predicted damage model parameters for 1000°C were chosen to match the temperature trends of each parameter shown in Figure 4.9. With more data points (experimental results from additional temperatures), more

complex relationships could be investigated to better capture the effects of temperature on each parameter. In this case, however, the lack of experimental results precludes more accurate investigation, and only simple linear fits were applied to each parameter. A linear fit is deemed appropriate for the purposes of this study. The temperature trends for each parameter within the range of RT to 1200 °C are monotonic, so the rough overall temperature-dependent behavior of each parameter within this range is retained using linear fits. However, more accurate relationships (sigmoidal or exponential trends) would be necessary to attempt to predict the CMC response outside the temperature range investigated in this work. The predicted response and experimental results for 1000°C show good agreement, which serves to validate the predictive capabilities of the temperature dependent model within the temperature range considered in this work.

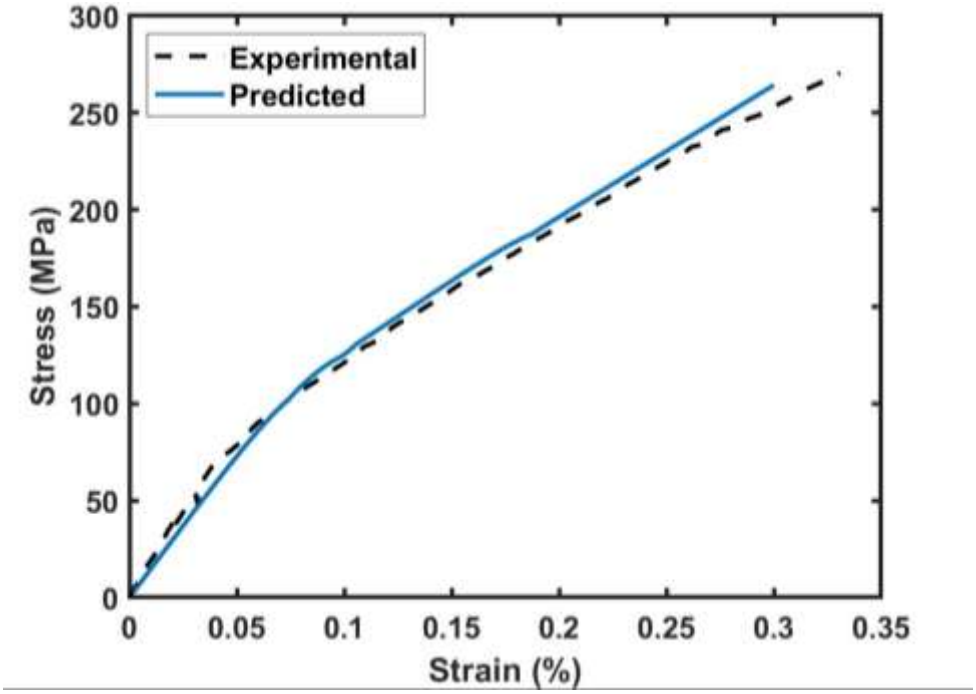

Figure 4.11. Predicted C/SiC Longitudinal Response Compared to Experiment (Yang, Zhang, Wang, Huang, & Jiao, 2017) for 1000°C

4.4 SiC/SiC

The model developed as part of this work effectively captures the quasi-brittle damage response of the SiC matrix used in C/SiC CMCs. By modifying the weave-level RUC and performing additional parameter calibration, this model can be applied to nearly any woven brittle-matrix composite. To demonstrate this capability, the model has been applied to simulate the temperature-dependent thermomechanical response of a 2D woven 5HS SiC/SiC CMC. The CVI and MI matrix densification steps used to manufacture the SiC/SiC CMC results in two SiC matrix phases that were modeled as separate materials with distinct thermomechanical properties. A small volume fraction of excess Si pockets often forms as a result from the MI step, but these were assumed to have a negligible effect on the overall weave thermomechanical damage response and were not accounted for in this work. The more complicated architecture of the 5HS weave is displayed in Figure 4.12, which shows the thermal residual stresses resulting from simulated cooldown from ~1400°C to RT. The CTE mismatch between the constituents of the SiC/SiC CMC is much less than that of the C/SiC CMC. Additionally, the CVI/MI SiC/SiC is more resistant to matrix cracking because of the higher density matrix that occurs as voids and cracks are filled during the MI step. As a result, the SiC/SiC CMCs have lower thermal residual stresses and less significant manufacturing-induced damage despite the higher processing temperatures required for MI.

After the cooldown simulations, mechanical loading simulations are performed to obtain temperature-dependent stress strain responses (see Figure 4.13), which correlate well with experiments. As before, solid curves correspond to simulation results, dashed curves represent experimental results, and the colors of the curves indicate the corresponding experimental/simulation temperature. The calibrated model parameters used to simulate the RT and 1200°C SiC/SiC nonlinear thermomechanical response are included in Table 4.2. The rough trends observed in the C/SiC model appear to hold true here as well, and the less significant manufacturing-induced damage observed in the SiC/SiC material system relative to the C/SiC CMC is reflected in the low values of the a_0 parameter in the SiC/SiC model compared to the C/SiC model.

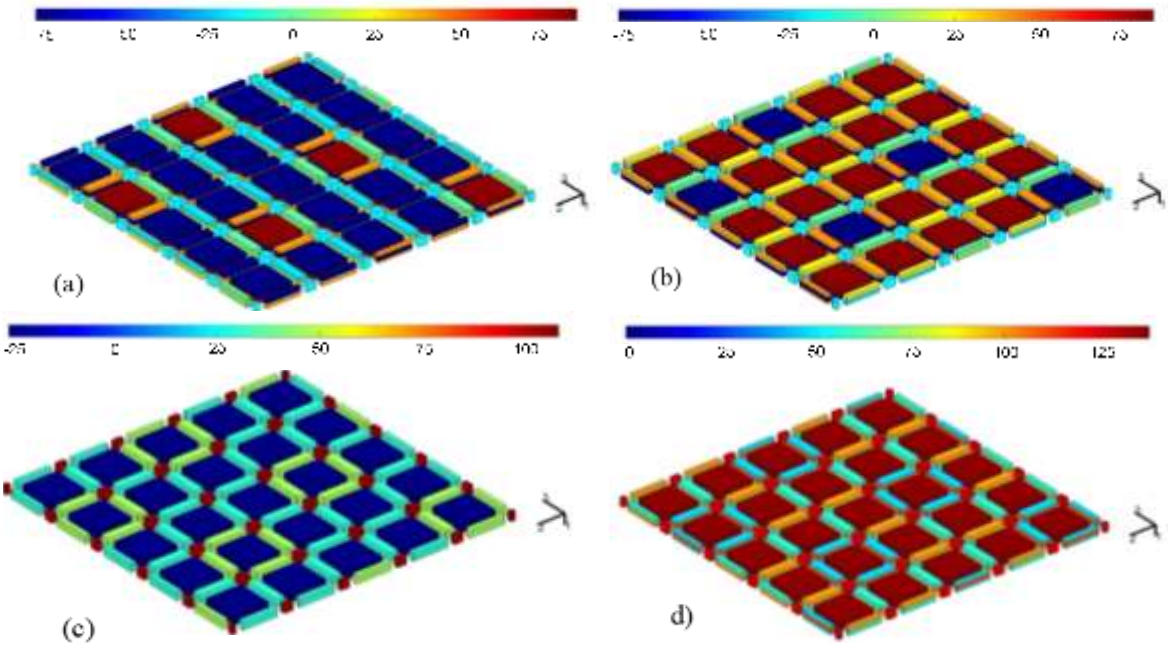

Figure 4.12. Simulated Thermal Residual Stresses for RT 5-HS weave SiC/SiC CMC. (a) Residual Transverse Stress (Weft Direction); (b) Residual Longitudinal Stress (warp Direction); (c) Residual Through-thickness Stress; (d) Residual Effective Stress

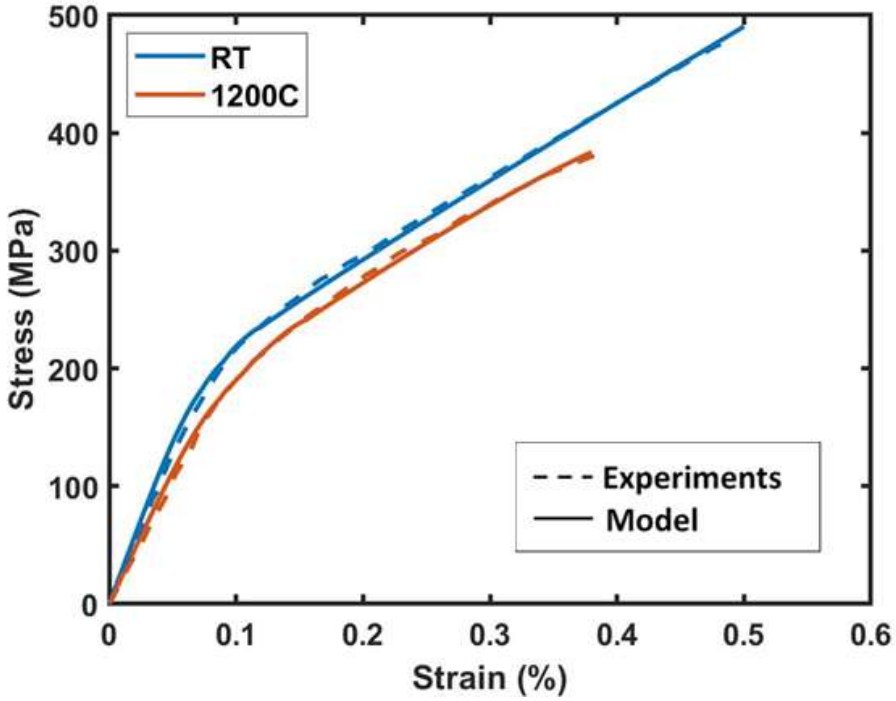

Figure 4.13. Temperature-dependent SiC/SiC Model Results Compared to Experiments from Ref. (Gowayed, et al., 2010)

Table 4.2. SiC/SiC Matrix Damage Model Parameters for RT and 1200°C

	a_0	a_1	b	η	n
RT	1100	400	$2.21x10^{-5}$	$1.22x10^{-4}$	0.14
1200°C	520	250	$1.07x10^{-5}$	$1.92x10^{-4}$	0.18

4.5 Experimental Testing for Model Validation

The temperature-dependent reformulated CMC damage model depends on calibration with experimental results. Experimental data from the literature has been used to calibrate the damage model parameters discussed in this work, but this data is only available for a few CMC material systems at specific temperatures. This shortage of experimental data limits the accuracy and predictive capability of the model. Thermomechanical test data from a range of temperatures and loading conditions is required to improve and experimentally validate the damage model. A uniaxial MTS test frame has been equipped with an AMTECO furnace (see Figure 4.14) to conduct the experiments. A slot was prepared in the furnace insert to accommodate the specimen geometry, and the furnace was fired to bake out the ceramic inserts and remove excess binders. The furnace is shown in operation in Figure 4.15

Figure 4.14. Experimental Setup with MTS Load Frame and AMTECO Furnace

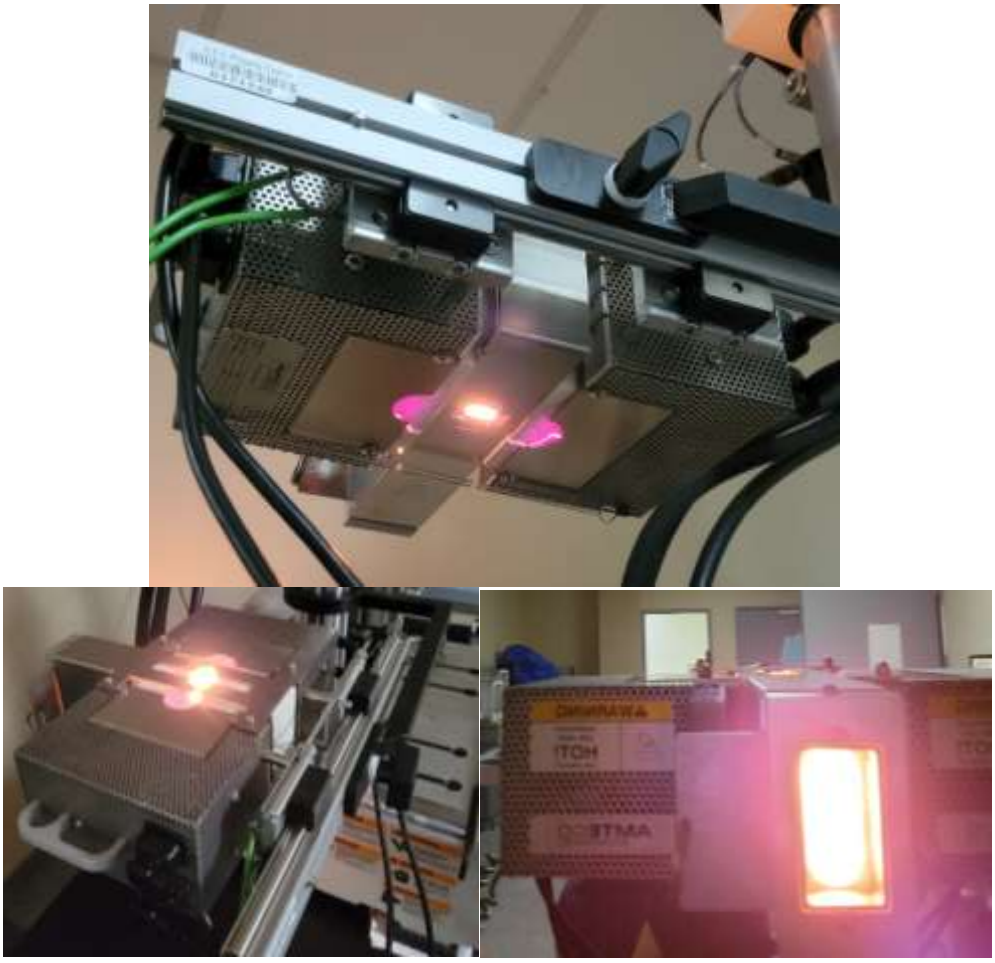

Figure 4.15. AMTECO Furnace in Operation

Room temperature tests were conducted using S200H C/SiNC CMC specimens. The specimen geometry and dimensions are shown in Figure 4.16 and Table 4.3. The tests were conducted at quasistatic strain rate of 1×10^{-5} and show good agreement with similar tests from the literature with the same material system (see Figure 4.17). Additional tests

will be performed across the temperature range between RT and ~1400°C to further inform and validate the temperature-dependent CMC damage model.

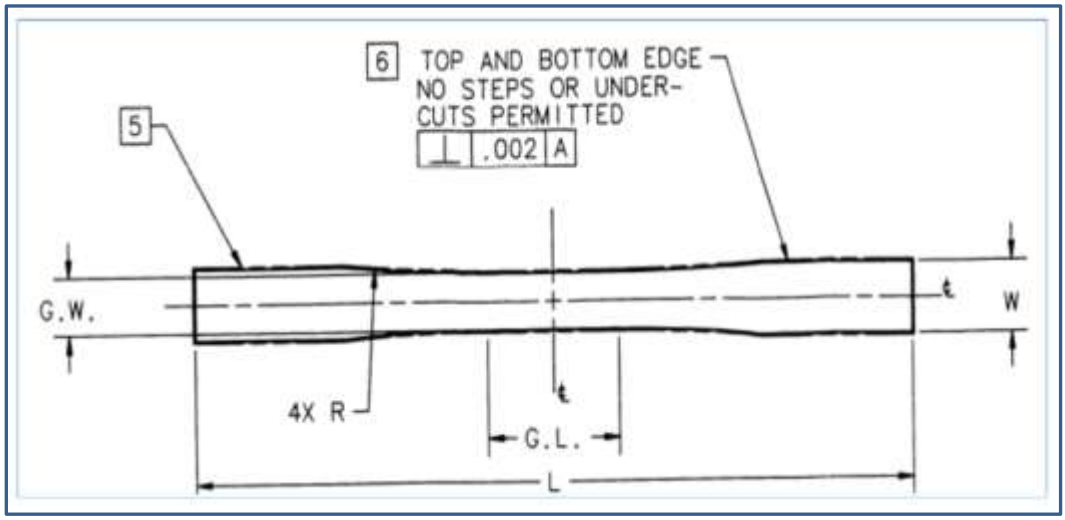

Figure 4.16. Specimen Geometry for S200 H C/SiNC CMC Specimens

Table 4.3. Dimensions (in mm) for S200H C/SiNC Specimen Geometry in Figure 4.16.

	Orientation	
Dimension (mm)	**0°/90**	**+/-45°**
L	152.4	152.4
W	12.7	21.59
GL	27.94	27.94
GW	10.16	19.05
R	368.3	368.3

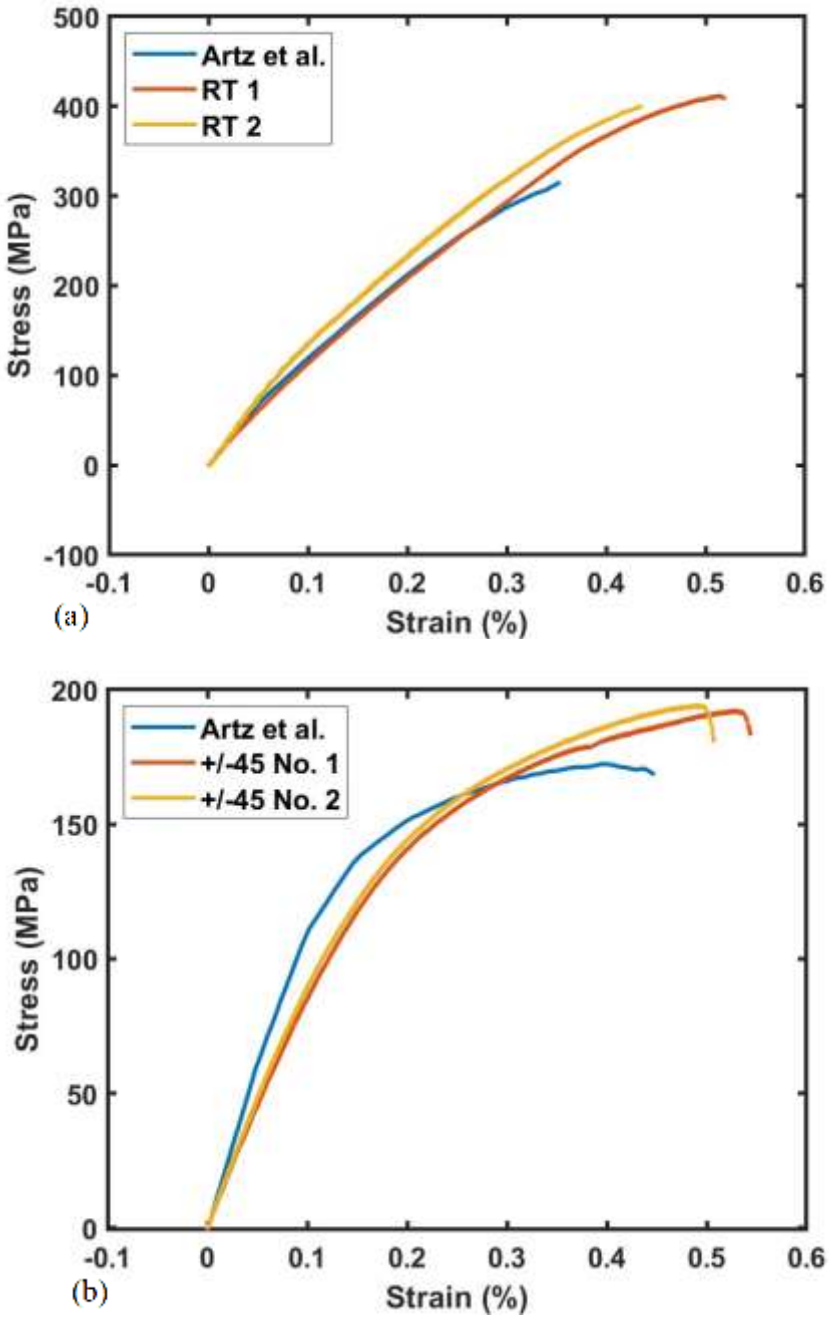

Figure 4.17. Room Temperature Experimental Results for S200H C/SiNC CMC Specimens Compared to Experiments from Literature (Artz, Yuan, Kumar, & Fish, 2020); (a) 0°/90° S200H C/SiNC CMC; (b) ±45° S200H C/SiNC CMC

Additional RT tests for the 0° and +/- 45° S200H were conducted and non-contact full field DIC (see Figure 4.18) was used to obtain the 3D strain map of the specimen surfaces. These images capture key deformation localization phenomena that are directly related to the localized damage behavior. Figure 4.19 shows the major strain for several frames from the DIC results for a 0° quasistatic RT load test using the S200H material. Figure 4.19(a) and (b) show the major strain field in the specimen at 0% longitudinal strain and 0.048% longitudinal strain. Even at the very low strain shown in Figure 4.19(b), regions of higher localized deformation are apparent near defects (strain hotspot) and in the undulating tow and intertow regions. The remaining images are from later in the load test, with Figure 4.19(c), (d), and (e) showing the surface major strain field for 0.4%, 0.45%, and 0.5% longitudinal strain, respectively. At higher longitudinal strains, the localization in and around undulating tows and intertow regions is more apparent. Figure 4.19(e), which was taken within one second of failure, shows significant localization as a result of damage. Final failure occurred at approximately 0.5% strain.

Figure 4.20 shows several frames from the DIC results showing the surface major strain field for +/-45° S200H specimen in RT quasistatic tension. As with the DIC results from the 0°/90° specimens, the strain localization patterns offer valuable insight into the damage initiation and propagation behavior of the material. Figure 4.20(d) shows significant localization along both the +45° direction as well as the -45° direction. The localization originates from the specimen edge and propagates toward the center at the same angle as the weave-level RUC. Figure 4.20(e) shows the major strain profile immediately preceding failure. In this image, the localizations along the +45° and -45° directions have increased

in severity, and failure occurs when the localizations intersect. Figure 4.20(f) shows that the specimen failed along the -45° direction.

The typical failure pattern for the 0°/90° and +/-45° S200H C/SiNC CMCs are shown in Figure 4.21. In each case, the dominant failure mechanisms align with the orientation of the weft tows in the weave-level RUC. The 0°/90° specimens failed perpendicular to the loading direction (along the 90° weft tows), and the +/-45° specimens typically failed at -45° relative to the loading direction (along the -45° weft tows). Failure tends to occur along the weft tows because the weft tows have slightly greater undulation than the warp tows. The higher undulation results in more fiber misalignment, which slightly decreases the stiffness and strength in those directions. Additionally, undulation sites typically have more flaws and higher void volume fractions, which serve as stress concentration and damage initiation sites.

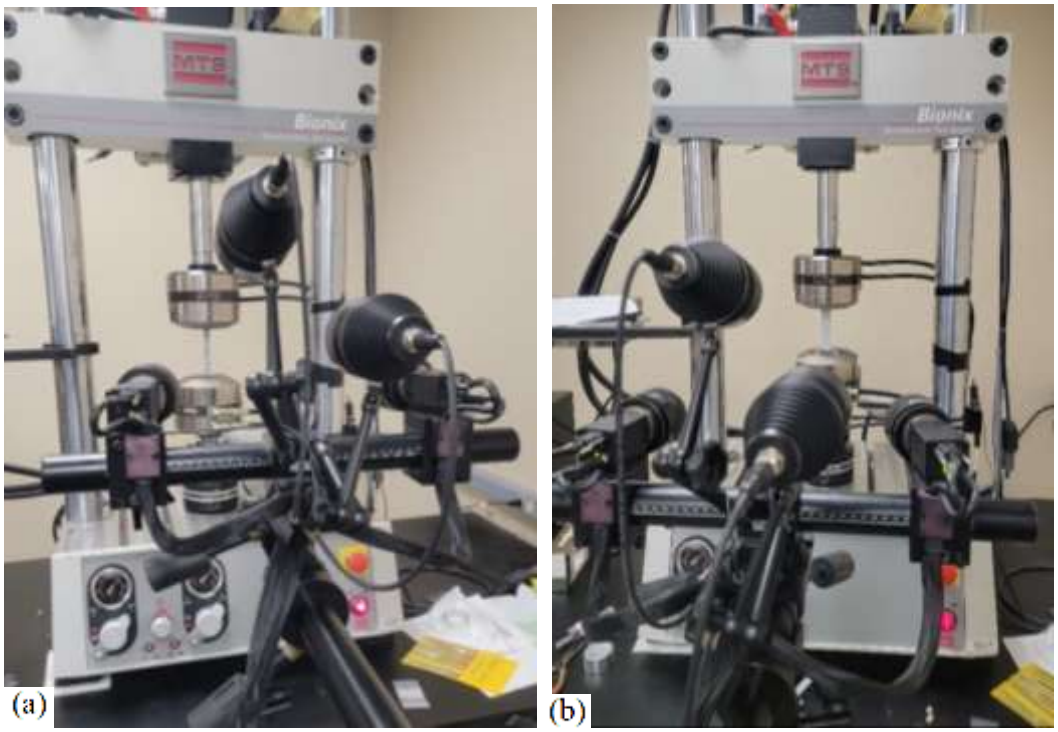

Figure 4.18. DIC ARAMIS Setup with MTS Bionix Load Frame; (a) 0° S200H Specimen; (b) +/-45° S200H Specimen

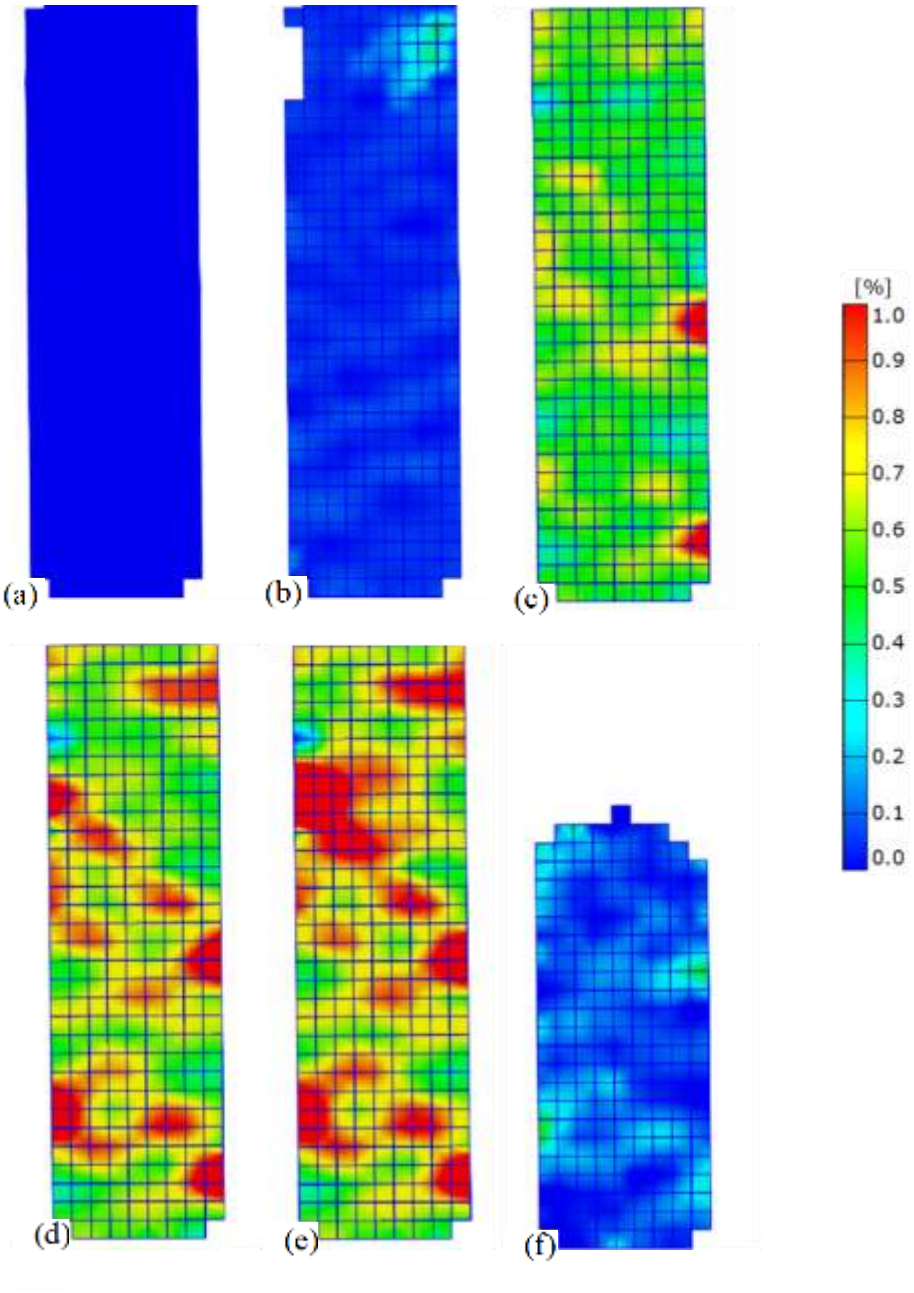

Figure 4.19. Select Major Strain DIC Results for RT Quasi Static Load Test for 0°/90° S200H CMC; (a) 0% Strain; (b) 0.048% Strain—Localized Strain Near Defect and in

Undulating Tows and Intertow Regions ; (c) 0.4% strain; (d) 0.45% Strain; (e) 0.5% Strain (Immediately Preceding Failure); (f) Post Failure

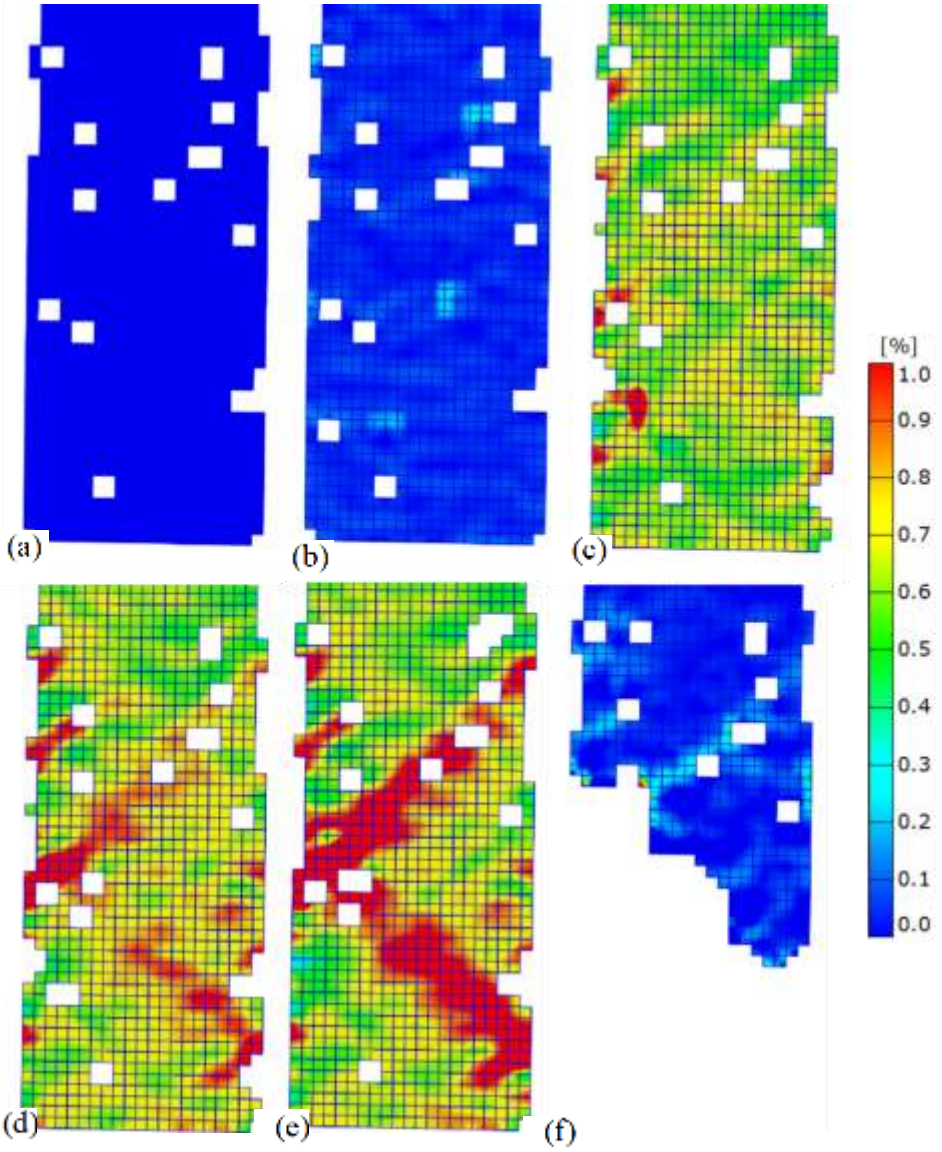

Figure 4.20. Select Major Strain DIC Results for RT Quasi Static Load Test for +/-45° S200H CMC; (a) 0% Strain; (b) 0.05% Strain—Localized Strain in Undulating Tows and

Intertow Regions ; (c) 0.45% strain; (d) 0.48% Strain; (e) 0.5% Strain (Immediately Preceding Failure); (f) Post Failure

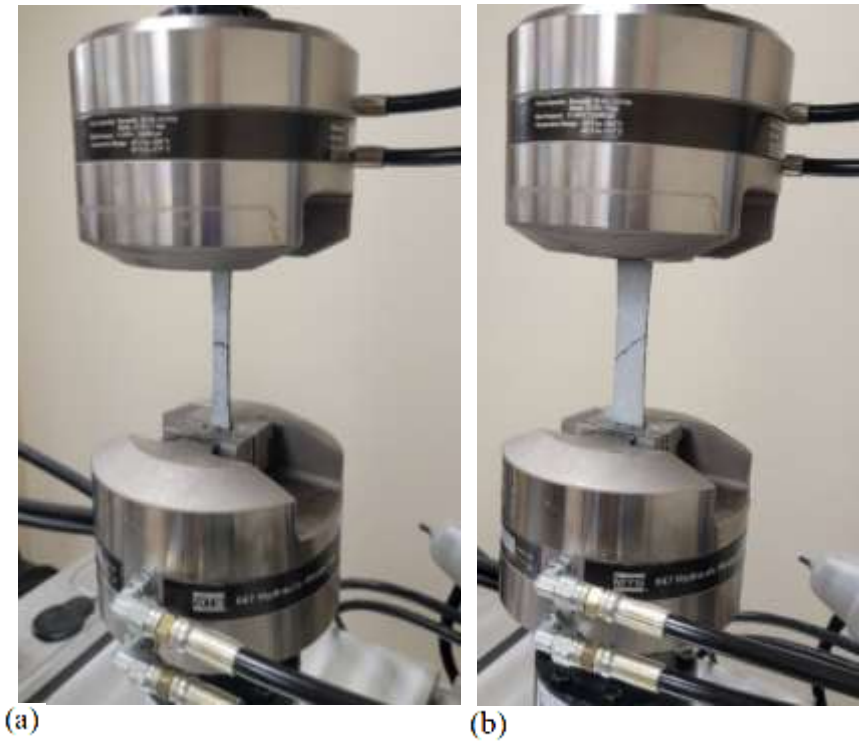

Figure 4.21. Failed S200H Specimens; (a) 0° Specimen; (b) +/- 45° Specimen

4.6 Conclusions

A multiscale thermomechanical CMC simulation framework was developed and implemented using MSGMC to capture the temperature-dependent damage behavior of woven CMCs. The modeling framework was applied to 2D woven CMCs including plain weave C/SiC CMCs manufactured using CVI and 5HS SiC/SiC CMCs manufactured using a two-step CVI/MI matrix densification process. The nonlinear predictive capabilities of the model are demonstrated and show excellent agreement with the literature. The framework consists of cooldown simulations to capture thermal residual stresses and

subsequent mechanical loading simulations to capture deformation and damage behavior. A fracture mechanics-informed thermomechanical progressive damage model is used to simulate the cooldown damage that occurs as a result of the high thermal residual stresses and to capture the temperature-dependent damage behavior of the CMCs at temperatures ranging from RT to 1200°C. A unified damage ISV is defined that combines the effects of microporosity/precrack nucleation and growth with crack activation and propagation. Crack growth kinetics and fracture mechanics are used to determine the transition from precrack to crack as well as to simulate the effects of crack propagation on the matrix mechanical properties. Additionally, an experimental process has been developed and experimental results have been verified with similar experiments with the same material system from the literature. The AMTECO furnace has been incorporated into the experimental setup and a slot has been cut into the ceramic insert to accommodate the specimen geometry. The furnace has been fired to achieve bake out, and the excess binder in the ceramic inserts has been burned away. The furnace and MTS load frame experimental setup will be used to perform high temperature testing at temperatures ranging from RT to ~1400°C and the high temperature experimental results will be used to further inform and to validate the modeling framework introduced in this chapter. The main outcomes of this work are as follows:

- Formulation of residual stresses due to manufacturing related cool down and investigation of flaws and damage in as-produced CMCs

- Incorporation of the cool down simulation with a reformulated fracture mechanics-informed damage model for more accurate prediction of temperature-dependent damage and failure in CMCs
- Implementation of the new damage model within a multi-physics thermomechanical multiscale methodology to capture CMC damage progression and deformation behavior under thermomechanical loading.
- Development of experimental setup to perform RT and high temperature tests using various CMC material systems. Experimental results can be used to inform and validate the simulation framework.

5 CONTRIBUTIONS AND FUTURE WORK

5.1 Contributions

The primary objective of the research presented in this dissertation was to utilize experimental and modeling techniques to develop comprehensive insight into the complex deformation and damage behavior of fiber reinforced composite materials. Both polymer matrix and ceramic matrix composite material systems were investigated, and the fracture behavior and key damage mechanisms of each material system were explored.

The damage accumulation and propagation behavior in CFRP composites under complex in-phase biaxial fatigue loading was investigated to capture early stage damage and obtain an improved understanding of damage propagation and associated degradation in material properties. Both cross ply and quasi isotropic laminate configurations were studied and the tests were conducted under constant amplitude in-plane, in-phase biaxial loading. An optimization technique was used to design the cruciform specimens for each stacking sequence. To understand the propagation of damage from the micro-to the macroscale, the fractured surfaces were analyzed, during various stages of fatigue, using electron microscope assisted fractography and a high-resolution camera. Material property degradation was determined by measuring the change in specimen stiffness to analyze the progression of fatigue damage and is correlated to the micro- and macroscale damage mechanisms and the biaxial fatigue loading parameters. The results provide insight into the initiation and propagation of damage mechanisms in CFRP composites which is essential to understanding the fatigue behavior of composite materials under complex multiaxial loadings.

The temperature-dependent damage response of brittle matrix CMC materials were also investigated, and a fracture mechanics-informed damage model was developed and incorporated within a multiscale simulation framework to simulate the thermomechanical damage response. The framework consists of cooldown simulations, which capture a realistic material initial state, and subsequent mechanical loading simulations to capture temperature-dependent nonlinear stress–strain behavior. The cooldown simulations result in a realistic material initial state with thermal residual stresses and damage hotspots that occur due to constituent property mismatch and post-manufacturing cooldown. The simulations were applied to 2D plain weave C/SiC and SiC/SiC CMCs at temperatures ranging from room temperature (RT) to 1200 °C. The model captures the brittle matrix cracking response of the CMCs and shows good agreement with experiments.

5.2 Future Work

The research presented in this dissertation serves to significantly improve understanding of several fiber reinforced composite deformation and damage behavior under a variety of loading and environmental conditions. However, further developments and advancements will maximize its applicability and considerably extend its effectiveness. Additional study and future work will be essential to further understand, predict, and delay damage initiation and progression in fiber reinforced polymer and ceramic matrix composites.

The biaxial fatigue study presented in Chapter 2 that discusses the initiation and propagation of key biaxial fatigue damage mechanisms in CFRP composite laminates can be extended to explore the effects of out-of-phase planar biaxial loading conditions.

Additionally, new material stacking sequences can be investigated to further understand the effects of stacking sequence and external loading conditions on the biaxial fatigue damage behavior of the CFRP laminates. Finally, the biaxial fatigue behavior of the nano-enhanced CFRP laminates with embedded buckypaper membranes can be investigated. In each of these cases, the nucleation and propagation of damage mechanisms can be investigated using SEM fractography techniques and correlated to external loading, stacking sequence, and the placement of the buckypaper membrane within the specimen gage region. Additionally, the self-sensing capabilities of the laminates with embedded buckypaper can be investigated, and resistance changes can be correlated to fatigue damage to predict remaining useful life. The additional insight provided by these future tasks will provide valuable understanding of the nucleation and growth of fatigue damage in CFRP laminates under complicated multiaxial fatigue loading conditions. This will enable more accurate fatigue life prediction methodologies and will allow designers and material selections engineers to make more informed decisions.

The fracture mechanics-informed CMC damage model in Chapter 3 and the temperature-dependent multiscale thermomechanical CMC modeling framework in Chapter 4 contribute increased understanding of the mechanisms of damage in brittle matrix composite systems, but further investigation into the temperature-dependent deformation and damage behavior of CMCs is warranted. The modeling framework can be applied to additional CMC systems fabricated using various methodologies including CVI, PIP, and MI, to investigate the effects of different constituent combinations and manufacturing processes on the temperature-dependent response of CMCs. The

experimental setup incorporating the tabletop MTS load frame and the AMTECO furnace can be used to perform experiments at a variety of temperatures and environmental conditions. Quasistatic load/unload testing in these conditions will provide valuable insight into the deformation and damage behavior of the CMCs and will help to partition the nonlinearities in the stress-strain response. This will help determine what nonlinearity is caused by damage and what is caused by inelastic effects such as plasticity (at high temperatures), crack opening, crack face sliding, fiber pullout, or interfacial debonding. Creep testing can also be performed under conditions that will help to understand the oxidative, temperature, and environmental degradation behavior of various CMC systems. The insight gained by these further investigations will contribute significant insight into the scale-dependent temperature- and environmentally-dependent deformation and damage behavior of these complex composite materials.

REFERENCES

Aboudi, J., Arnold, S., & Bednarcyk, B. (2012). *Micromechanics of composite materials: a generalized multiscale analysis approach.* Butterworth-Heinemann.

Arai, Y., Inoue, R., Goto, K., & Kogo, Y. (2019). Carbon fiber reinforced ultra-high temperature ceramic matrix composites: A review. *Ceramics International, 45*(12), 14481-14489.

Arhatari, B., Zonneveldt, M., Thornton, J., & Abbey, B. (2017). Local Structural Damage Evaluation of a C/C–SiC Ceramic Matrix Composite. *Microscopy and Microanalysis, 23*(3), 518-526.

Artz, T., Yuan, Z., Kumar, R., & Fish, J. (2020). Computational model for oxidation-assisted rupture of ceramic matrix composites. *International Journal of Solids and Structures*, 195-207.

Baptista, R., Claudio, R. A., Reis, L., Madeira, J. F., & Freitas, M. (2016). Numerical study of in-plane biaxial fatigue crack growth with different phase shift angle loadings on optimal specimen geometries. *Theoretical and Applied Fracture Mechanics, 85*, 16-25.

Bar-on, E., Rubin, M. B., & Yankelevsky, D. Z. (2003). Thermomechanical constitutive equations for the dynamic response of ceramics. *International Journal of Solids and Structures, 40*, 4519-4548.

Bathias, C. (1991). Fracture and fatigue of high performance composite materials: mechanisms and prediction. *Engineering Fracture Mechanics, 40*(4), 757-783.

Bathias, C. (2006). An engineering point of view about fatigue of polymer matrix composite materials. *International Journal of Fatigue, 28*(10), 1094-1099.

Bednarcyk, B. A., & Arnold, S. M. (2001). Micromechanics-based deformation and failure prediction for longitudinally reinforced titanium composites. *Composites Science and Technology, 61*(5), 705-729.

Binner, J., Porter, M., Baker, B., Zou, J., Venkatachalam, V., Diaz, V. R., . . . Murthy, T. (2020). Selection, processing, properties and applications of ultra-high temperature ceramic matrix composites, UHTCMCs–a review. *International Materials, 65*(7), 389-444.

Bonacuse, P. J., Mital, S., & Goldberg, R. (2011). Characterization of the as manufactured variability in a CVI SiC/SiC woven composite. *Proceedings of ASME turbo expo 2011*.

Borkowski, L., & Chattopadhyay, A. (2015). Multiscale model of woven ceramic matrix composites considering manufacturing induced damage. *Composite Structures, 126*, 62-71.

Budiansky, B., & O'Connell, R. J. (1976). Elastic moduli of a cracked solid. *International Journal of Solids and Structures, 12*(2), 81-97.

Camus, G. (2000). Modelling of the mechanical behavior and damage processes of fibrous ceramic matrix composites: application to a 2-D SiC/SiC. *International Journal of Solids and Structures, 37*(6), 919-942.

Cao, H. C., Bischoff, E., Sbaizero, O., Ruhle, M., Evans, A. G., Marshall, D. B., & Brennan, J. J. (1990). Effect of interfaces on the properties of fiber-reinforced ceramics. *Journal of the American Ceramic Society, 73*(6), 1691-1699.

Caputo, A. J., & Lackey, W. J. (1984). Fabrication of fiber-reinforced ceramic composites by chemical vapor infiltration.

Cherapanov, G. P. (1967). The propagation of cracks in a continuous medium. *Journal of Applied Mathematics and Mechanics, 31*(3), 503-512.

Curtin, W. A. (1991). Theory of mechanical properties of ceramic matrix composites. *Journal of the American Ceramic Society, 74*(11), 2837-2845.

Curtis, P. T. (1991). Tensile fatigue mechanisms in unidirectional polymer matrix composite materials. *International Journal of Fatigue, 13*(5), 377-382.

Daniel, I. M., Wooh, S. C., & Lee, J. W. (1987). Defect and Damage Characterization in Composite Materials. *Review of Progress in Quantitative Nondestructive Evaluation.* Evanston, IL.

Daniel, I., & Ishai, O. (2006). *Engineering Mechanics of Composite Materials 2nd Ed.* Oxford University Press.

Datta, S., Neerukatti, R., & Chattopadhyay, A. (2018). Buckypaper embedded self-sensing composite for real-time fatigue damage diagnosis and prognosis. *Carbon*, 353-360.

Degrieck, J., & Van Paepegem, W. (2001). Fatigue damage modeling of fibre-reinforced composite materials. *Applied mechanics reviews, 54*(4), 279-300.

Deshpande, V. S., & Evans, A. G. (2008). Inelastic deformation and energy dissipation in ceramics: a mechanism-based constitutive model. *Journal of the Mechanics and Physics of Solids, 56,* 3077-3100.

DiCarlo, J. A. (2015). Advances in SiC/SiC composites for aero-propulsion. In T. A. Society, N. P. Bansal, & J. Lamon (Eds.), *Ceramic Matrix Composites: Materials, Modeling, and Technology* (pp. 217-235). John Wiley & Sons, Inc.

Evans, A. G., Rice, J. R., & Hirth, J. P. (1980). Suppression of cavity formation in ceramics: Prospects for superplasticity. *Journal of the American Ceramic Society, 63*(7), 368-375.

Flory, P. J. (1961). Thermodynamic relations for high elastic materials. *Transactions of the Faraday Society, 57,* 829-838.

French, J., Rapking, D., Mollenhauer, D., & Czabaj, M. (2016). Development of a novel in-plane tension-tension biaxial cruciform specimen. *31st Annual Technical Conference of the American Society of Composites.* Williamsburg, VA.

Gowayed, Y., Ojard, G., Miller, R., Santhosh, U., Ahmad, J., & John, R. (2010). Correlation of elastic properties of melt infiltrated SiC/SiC composites to in situ properties of constituent phases. *Composites Science and Technology, 70,* 435-441.

Greenhalgh, E. (2009). Failure Analysis and Fractography of Polymer Composites. Woodhead Publishing Limited.

Hashin, Z. (1985). Cumulative damage theory for composite materials: Residual life and residual strength methods. *Composites Science and Technology, 23*(1), 1-19.

Heidenreich, B. (2015). C/SiC and C/C-SiC Composites. In *Ceramic Matrix Composites: Materials, Modeling and Technology* (pp. 147-216). Hoboken, NJ: John Wiley & Sons.

Hild, F., Burr, A., & Leckie, F. (1996). Matrix cracking and debonding of ceramic-matrix composites. *International Journal of Solids and Structures, 33*(8), 1209-1220.

Ichikawa, H. (2016, February 29). Polymer-derived ceramic fibers. *Annual Review of Materials Research*, pp. 335-356.

Kanoute, P., Boso, D. P., Chaboche, J. L., & Schrefler, B. A. (2009). Multiscale methods for composites. *Archives of Computational Methods in Engineering, 16*(1), 31-75.

Kawai, M. (2004). A phenomenoligical model for off-axis fatigue behavior of unidirectional polymer matrix composites under different stress ratios. *Composites Part A: Applied Science and Manufacturing, 35*(7), 955-963.

Kawai, M., Yajima, S., Hachinohe, A., & Takano, Y. (2001). Off-Axis Fatigue Bahavior of Unidirectional Carbon Fiber-Reinforced Composites at Room and High Temperatures. *Journal of Composite Materials, 35*(7), 545-576.

Khafagy, K. H., Datta, S., & Chattopadhyay, A. (2021). Multiscale characterization and representation of variability in ceramic matrix composites. *Journal of Composite Materials*. doi:10.1177/0021998320978445

Krenkel, W. (Ed.). (2008). Ceramic matrix composites: fiber reinforced ceramics and their applications. John Wiley & Sons.

Ladeveze, P., Gasser, A., & Allix, O. (1994). Damage Mechanisms Modeling for Ceramic Composites. *Journal of Engineering Materials and Technology, 116*(3), 331-336.

Lee, C. S., Hwang, W., Park, H. C., & Han, K. S. (1999). Failure of carbon/epoxy composite tubes under combined axial and torsional loading. Fracture morphology and failure mechanisms. *Composites Science and Technology, 59*(12), 1789-1804.

Lemaitre, J. A. (2012). *A course on damage mechanics.* Springer Science and Business Media.

Lemaitre, J., & Desmorat, R. (2005). *Engineering Damage Mechanics.* Springer.

Li, G., Datta, S., Chattopadhyay, A., Iyyer, N., & Phan, N. (2019). An online-offline prognosis model for fatigue life prediction under biaxial cyclic loading with overloads. *Fatigue and Fracture of Engineering Materials and Structures*.

Lipowitz, J., Rabe, J. A., Zangvil, A., & Zu, Y. (1997). Structure and properties of Sylramic™ silicon carbide fiber—A polycrystalline, stoichiometric β-SiC composition. *Proceedings of the 21st Annual Conference on Composites, Advanced Ceramics, Materials, and Structures—A: Ceramic Engineering and Science Proceedings.* Hoboken, NJ.

Liu, K. C., Chattopadhyay, A., & Arnold, S. M. (2011). Impact of material and architecture model parameters on the failure of woven CMCs via the multiscale generalized method of cells. In *Developments in Strategic Materials and Computational Design II: Ceramic Engineering and Science Proceedings* (pp. 175-192).

Liu, K. C., Chattopadhyay, A., Bednarcyk, B., & Arnold, S. M. (2011). Efficient Multiscale Modeling Framework for Triaxially Braided Composites using Generalized Method of Cells. *Journal of Aerospace Engineering, 24*(2), 162-169.

Longbiao, L. (2018). Damage and fracture of a ceramic matrix composite under isothermal and thermomechanical fatigue loading. *Theoretical and Applied Fracture Mechanics, 95*, 218-232.

Lua, J., Pham, D. C., Rahman, A., & Phan, N. D. (2018). A Progressive Damage Model for Fatigue Analysis of Woven Fabric Composites. *AHS International 74th Annual Forum and Technology Display.* Phoenix, AZ.

Luo, R. Y., & Cheng, Y. H. (2004). Effects of preform and pyrolytic carbon structur on thermophysical properties of 2D carbon/carbon composites. *Chinese Journal of Aeronautics, 17*(2), 112-118.

Maire, J. F., & Lesne, P. M. (1997). A damage model for ceramic matrix composites. *Aerospace Science and Technology, 1*(4), 256-266.

Makris, A., Vandenbergh, T., Ramault, C., Van Hemelrijck, D., Lamkanfi, E., & Van Paepegem, W. (2010). Shape optimisation of a biaxially loaded cruciform specimen. *Polymer Testing, 29*(2), 216-223.

Mayes, J. S., Welsh, J. S., & Key, C. T. (2002). Biaxial failure envelope for a glass fabric reinforced composite laminate. *Final report PO 00167*, 1-13.

Montesano, J., & Singh, C. V. (2015). Predicting evolution of ply cracks in composite laminates subjected to biaxial loading. *Composites Part B: Engineering, 75*, 264-273.

Montesano, J., McCleave, B., & Singh, C. V. (2018). Prediction of ply crack evolution and stiffness degradation in multidirectional symmetric laminates under multiaxial stress states. *Composites Part B: Engineering, 133*, 53-67.

Morscher, G. (1997). Tensile Stress Rupture of SiCf/SiCm Minicomposites with Carbon and Boron Nitride Interphases at Elevated Temperatures in Air. *Journal Of The American Ceramic Society, 80*(8), 2029-2042.

Morscher, G. N., & Martinez-Fernandez, J. (1999). Fiber effects on minicomposite mechanical properties for several silicon carbide fiber-chemically vapor-infiltrated silicon carbide matrix systems. *Journal of the American Ceramic Society, 82*(1), 145-155.

Murthy, P. L., Mital, S. K., & DiCarlo, J. A. (1999). Characterizing the properties of a woven SiC/SiC composite using W-CEMCAN computer code. *NASA NTRS Reports*.

Ohnabe, H., Masaki, S., Onozuka, M., Miyahara, K., & Sasa, T. (1999). Potential application of ceramic matrix composites to aero-engine components. *Composites Part A: Applied Science and Engineering, 30*(4), 489-496.

Paliwal, B., & Ramesh, K. T. (2008). An interacting micro-crack damage model for failure of brittle materials under compression. *Journal of the Mechanics and Physics of Solids, 56*, 896-923.

Paliwal, B., Ramesh, K. T., & MaCauley, J. W. (2006). Direct observation of the dynamic compressive failure of a trnasparent polycrystalline ceramic. *Journal of the American Ceramic Society, 89*, 2128-2133.

Peng, T., Liu, Y., Saxena, A., & Goebel, K. (2015). In-situ fatigue life prognosis for composite laminates based on stiffness degradation. *Composite Structures, 132*, 155-165.

Pradere, C., & Sauder, C. (2008). Transverse and longitudinal coefficient of thermal expansion of carbon fibers at high temperatures (300K-2500K). *Carbon, 46*(14), 1874-1884.

Quaresimin, M., & Carraro, P. A. (2013). On the investigation of the biaxial fatigue behaviour of unidirectional composites. *Composites Part B: Engineering, 54*, 200-208.

Quaresimin, M., Susmel, L., & Talreja, R. (2010). Fatigue behaviour and life assessment of composite laminates under multiaxial loadings. *International Journal of Fatigue, 32*(1), 2-16.

Rice, J. R. (1968). A Path Independent Integral and the Approximate Analysis of Strain Concentration by Notches and Cracks. *Journal of Applied Mechanics, 35*, 379-386.

Rohm and Haas. (2008). CVD Silicon Carbide Data Sheet.

Rubin, M. B., Vorobiev, O. Y., & Glenn, L. A. (2000). Mechanical and numerical modeling of a porous elastic-viscoplastic material with tensile failure. *Internaltional Journal of Solids and Structures, 37*, 1841-1871.

Rubio, V., Ramanujam, P., Cousinet, S., LePage, G., Ackerman, T., Hussain, A., . . . Binner, J. (2020). Thermal properties and performance of carbon fiber-based ultra-high temperature ceramic matrix composites (Cf-UHTCMCs). *Journal of the American Ceramic Society, 103*(6), 3788-3796.

Sadowski, T. (Ed.). (2007). Multiscale modelling of damage and fracture processes in composite materials. Springer Science and Business Media.

Sadowski, T., & Marsavina, L. (2011). Multiscale modelling of two-phase ceramic matrix composites. *Computational Materials Science, 50*(4), 1336-1346.

Schmidt, S., Beyer, S., Knabe, H., Immich, H., Meistring, R., & Gessler, A. (2004). Advanced ceramic matrix composite materials for current and future propulsion technology applications. *Acta Astronautica, 55*(3-9), 409-420.

Smits, A., Van Hemelrijck, D., Philippidis, T. P., & Cardon, A. (2006). Design of a cruciform specimen for biaxial testing of fibre reinforced composite laminates. *Composites Science and Technology, 66*, 964-975.

Sun, X. S., Haris, A., Tan, V. B., Tay, T. E., Narasimalu, S., & Della, C. N. (2012). A multi-axial fatigue model for fiber reinforced composite laminates based on Puck's criterion. *Journal of Composite Materials, 46*(4), 449-469.

Sun, Z., Daniel, I. M., & Luo, J. J. (2003). Modeling of fatigue damage in a polymer matrix composite. *Materials Science and Engineering: A, 361*(1), 302-311.

Talreja, R. (1981). Fatigue of composite materials: damage mechanisms and fatigue life diagrams. *Proceeding sof the Royal Society of London. A: Mathematical and Physical Sciences, 378*, 461-475.

Talreja, R. (1986). Stiffness properties of composite laminates with matrix cracking and interior delamination. *Engineering Fracture Mechanics, 25*(5-6), 751-762.

Torayca. (n.d.). *Technical Data Sheet No. CFA-001*. Retrieved 12 20, 2020, from https://www.rockwestcomposites.com/media/wysiwyg/T300DataSheet_1.pdf

Wachtman, J., Cannon, W. R., & Matthewson, M. J. (2009). Linear Elastic Fracture Mechanics. In *Mechanical Properties of Ceramics* (pp. 63-87). John Wiley & Sons.

Wang, H., & Ramesh, K. T. (2003). Dynamic strength and fragmentation of hot-pressed silicon carbide under uniaxial compression. *Acta Materialia, 52*, 355-367.

Wright, P., Fu, X., Sinclair, I., & Spearing, S. M. (2008). Ultra High Resolution Computed Tomography of Damage in Notched Carbon Fiber-Epoxy Composites. *Journal of Composite Materials, 42*(19), 1993-2002.

Yang, C. P., Zhang, L., Wang, B., Huang, T., & Jiao, G. Q. (2017). Tensile behavior of 2D C/SiC composites at elevated temperatures: Experiment and modeling. *Journal of the European Ceramic Society, 37*, 1281-1290.

Yang, Z., Yuan, H., & Markert, B. (2019). Representation of micro-structural evolution and thermo-mechanical damage in thermal shocked oxide/oxide ceramic matrix composites. *International Journal of Fatigue, 126*, 122-129.